Master Thesis - Hydraulic Engineering, TU Delft

Outer-Bank Shear Stress in River Bends

Numerical Modeling of Curved Flow

Anton W. van der Meer
a.w.vandermeer@student.tudelft.nl
Student Number: 4031431

Supervisors

Prof.dr.ir. W.S.J. Uijttewaal
TU Delft

Dr.ir. E. Mosselman
TU Delft & Deltares

Dr.ir. A. Crosato
TU Delft & Unesco IHE

Delft University of Technology
Faculty of Civil Engineering and Geosciences
Department of Fluid Mechanics

October 28, 2015

Abstract

In the dimensional averaged numerical models, that are used for practicle purposes, there need to be accounted for three-dimensional processes. Amongst others a bank shear stress parameterization need to be incorperated. This master thesis focusses on the outer-bank shear stress in order to obtain a parameterization for the outer-bank shear stress for naturally curved flows.

The outer-bank shear stress is obtained from three-dimensional numerical computations. The numerical modeling is based on the Large Eddy Simulator, available at the Fluid Mechanics Department of the Technical University of Delft. Despite the considerable progress achieved, the software is still under development and a thorough review of its code is therefore necessary. The aim of this master thesis is to assess the effect of the outer-bank roughness, the outer-bank angle and the transverse bed slope on the outer-bank shear stress and to test and improve the performance of the boundary method of the computational algorithm.

The magnitude of the outer-bank shear stress and the outer-bank cell increase for increasing roughness of the outer-bank, leading to a less uniform distribution of the outer-bank shear stress. The magnitude of the outer-bank shear stress decreases for increasing inclination of the outer-bank. For a more inclined outer-bank, the magnitude of the outer-bank shear stress is more dependent on the outer-bank roughness. No significant dependency of the distribution of the outer-bank shear stress on the outer-bank inclination can be found from the results. Inclusion of the point bar related transverse bed slope does not lead to a significant change of the magnitude and distribution of the outer-bank shear stress. Clearly, the helical motion outscores the effect of topographic steering.

The boundary method adds the frictional effects of solid boundaries to the computational algorithm. The implemented boundary method, the Immersed Boundary Method, allows for the implementation of complex boundaries on a structured grid. Although in some cases the boundary method has a good performance, it is not very robust and prone to errors. It is recognized that the near wall velocity profile using the Immersed Boundary Method does not often coincide with the actual momentum 'loss' at the wall. This problem, not recognized in earlier studies, can be attributed to inaccuracy in the description of the turbulent viscosity. The latter is understood and partly solved. The accuracy can be further improved by coarsening the grid or reconsidering the implemented turbulence closure model, the Smagorinsky Model. Different improved Smagorinsky Models are available.

List of Symbols

Symbol	Unit	Description
a	m/s^2	Acceleration
A		Scour Factor
A	m^2	Cross Sectional Area
b	m	Channel Width
c_f		Friction Coefficient
C_s		Smagorinsky Constant
F	N	Force
g	m/s^2	Gravitational Acceleration
h	m	Water Depth
I_b		Streamwise Bed Slope
I_e		Streamwise Energy Slope
k_s	m	Roughness Height
m	kg	Mass
p	Pa	Pressure
P	m	Perimeter
R	m	Radius of Curvature
R_h	m	Hydraulic Radius
s,n,z	m	Streamwise, Lateral and Vertical Direction
t	s	Time
u_*	m/s	Friction Velocity
v	m/s	Local Velocity
v'	m/s	Turbulent Intensity
V_s	m/s	Bulk Velocity
z^+		Wall Coordinate
ϵ	m^2/s^3	Dissipation of Turbulent Kinetic Energy
θ		Angle of Longitudinal Channel Slope
κ		Von Karman Constant
ν	m^2/s	Kinematic Viscosity
ρ	kg/m^3	Density of Water
τ	Pa	Shear Stress
τ_0	Pa	Cross Sectional Averaged Boundary Shear Stress
$\tau_{0,2D}$	Pa	Averaged Two-Dimensional Boundary Shear Stress
τ_b	Pa	Boundary Shear Stress
ϕ		Stream Function
ψ		Correction Factor
ω	s^{-1}	Vorticity

Contents

1 Introduction

1.1 Background and Problem Statement

Positive feedback between flow velocity and erosional processes result in the formation of rivers. Rivers transport water from a place of high (mountains) to a place of low altitude (sea). Because of instabilities and interactions with geology, rivers do not transport the water straight to the sea but through bends (Figure 1).

In a river bend the flow need to change direction. This implies a changing momentum vector and thus requires a force. This force is generated by a transverse water level gradient. Considering a cross-section in a river bend, the situation can be described by imposing an outward directed centrifugal force and an inward directed pressure gradient. Because in contrast to the pressure gradient the centrifugal force is not constant over depth, a secondary circulation cell develops. This secondary circulation cell is known as hellical motion or spiral flow. Result is that the flow in a river bend has a strong three-dimensional character.

To assess amongst others river migration, shipping routes and the spreading of polutants, numerical models are widely used. Beacause of the spatial scales of these models, three-dimensional models are practically not applicable and therefore the used models are often two-dimensional. In these dimensionally averaged models there need to be accounted for the three-dimensional processes. Amongst others a bank shear stress parameterization need to be incorperated. This master thesis focusses on the outer-bank shear stress in order to obtain a parameterization for the outer-bank shear stress for naturally curved flows.

In this thesis, knowledge about the outer-bank shear stress is collected using three-dimensional numerical models. The numerical modeling is based on the Large Eddy Simulator (Section 4.2), available at the Fluid Mechanics Department of the Technical University of Delft. This simulator is also used by `Ottevanger [2013]` (Chapter 2). Despite the considerable progress achieved, the software is still under development and a thorough review of its code is therefore necessary to correct imperfections.

1.2 Problem Analysis

From the literature review (Chapter 2) I concluded that there is insufficient confirmation to prove the applicability of the existing bank shear stress parameterizations in naturally curved flows. Further research is therefore necessary to extend the current bank shear stress parameterizations to naturally curved flows.

The Immersed Boundary Method is proposed by `Balaras [2004]` as the the boundary method for complex boundaries and implemented in the algorithm by `Van Balen [2010]`. Indeed in contrary to `Ottevanger [2013]`, who assessed rectangular cross-sections, a boundary method for complex boundaries needs to be included in the computational algorithm in order to calculate natural river bends. However, preliminary tests of the author show that the boundary shear stress obtained by the Immersed Boundary Method leads to an overestimation of the latter.

1.3 Research Scope

The goal of this research is to reduce this knowledge gap by improving knowledge about the distribution and magnitude of the outer-bank shear stress in naturally curved flows. In order

Figure 1: Creek in Sweden, not straight but consisting of a serie of bends.

to do so, the effect of outer-bank inclination, outer-bank roughness and a transverse bed slope on the outer-bank shear stress are assessed. The above mentioned is captured in the first three research questions.

1. How are the magnitude and distribution of the outer-bank shear stress affected by the **inclination** of the outer-bank?
2. How are the magnitude and distribution of the outer-bank shear stress affected by the **roughness** of the outer-bank?
3. How are the magnitude and distribution of the outer-bank shear stress affected by the, with the point bar related, **transverse bed slope**?

A visualization of the inclined outer-bank and point bar related transverse bed slope is included in Figure 2. The assessment of the performance of the algorithm in describing the boundary shear stress is captured in the fourth research question.

4. How accurate is the algorithm in describing the boundary shear stress, what is the reason for the inaccuracy and how can the accuracy be improved?

1.4 Approach

The aim of this Master Thesis is twofold: (1) to assess the effect of the outer-bank roughness, outer-bank angle and transverse bed slope on the bank shear stress and (2) to test and improve the performance of the computational algorithm. To answer the first point, insight is obtained by three-dimensional numerical calculations. A Large Eddy Simulator is used for the numerical computations, while the results are compared with identical physical experiments of `Duarte [2008]`. With regards to the second point, insight is obtained by numerical and hand calculations. Please go to Chapter 4 for a detailed description of the methodology.

1.5 Outline

This report is divided as follows: the state of the art in the current research about boundary shear stress parameterizations (Chapter 2); the theoretical background regarding turbulent flow (Chapter 3); the methodology (Chapter 4); the plain results (Chapter 5); the discussion of the research questions (Chapter 6) and; the conclusions and recommendations (Chapter 7).

The appendix contains derivations and elaborations on equations and mechanisms, a manual of the computational algorithm and three preliminary versions of spin-off analytical models.

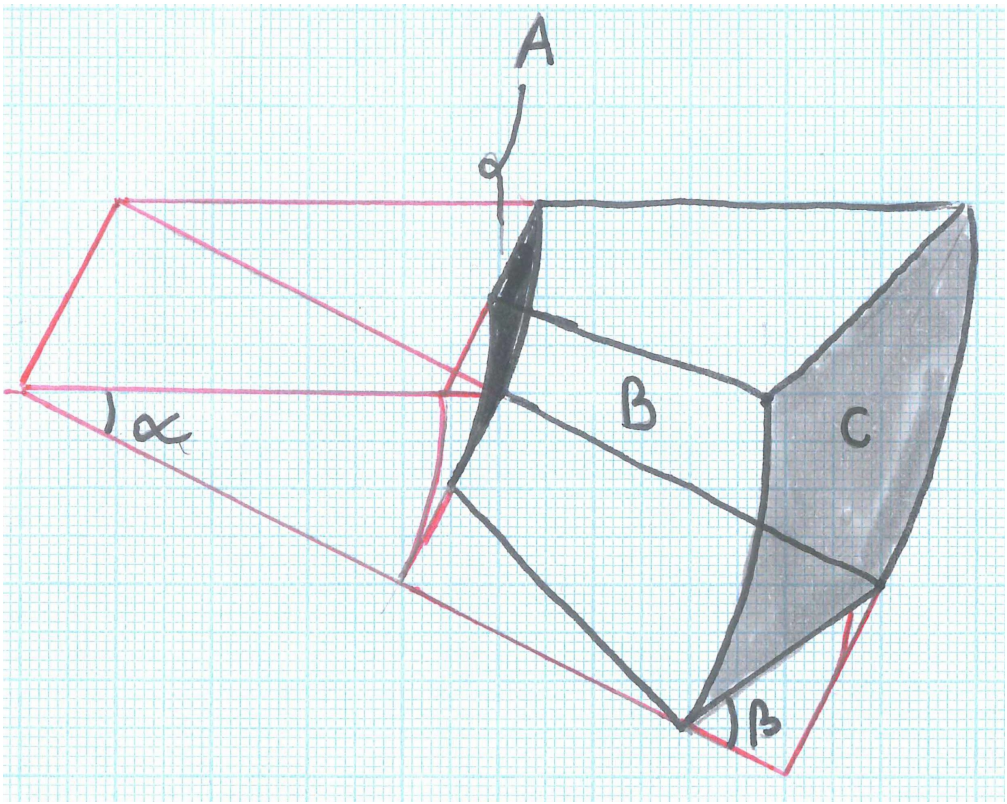

Figure 2: Sketch, showing (A) the inner-bank; (B) point bar related transverse bed slope; (C) inclined outer-bank; (β) angle of the inclined outer-bank; (α) the longitudinal angle of the bend.

2 State of the Art

Different relations have been derived for either the mean, maximum and/or distribution of the boundary shear stress in ducts and channels. All the existing relations known by the author are discussed in the following subsections.

2.1 Lane [1955], Chow [1959]

Lane [1955] describes the distribution of the bank and bed shear stress for a straight rectangular and trapezoidal channels with a uniform boundary roughness. This approach is widely used and often referred to Chow [1959], who describes the results is his book: Open channel hydraulics. It is assumed that "*the pattern of distribution varies with shape but is practically unaffected by the size of section*" (Chow [1959]). A relation is posed for the maximum ('mean in time and max in space' value) bank and bed shear stress (see Figures 3 and 4). The relations result from membrane-analogy, analytical and numerical studies in trapezoidal, v-notch and rectangular channels with fixed-beds. The data set, which can be found in Lane's [1955] Table 5, consists of sixteen measurements. The width-to-depth ratios used range from zero to eight. Note that the shear stress is scaled with the average two-dimensional boundary shear stress instead of the cross sectional averaged shear stress (Section 3.1).

2.2 Cruff [1965]

Based on data of Tracy and Lester [1961], Keulegan [1938] and Leutheusser [1963], the distributions of the bed and bank shear stress for rectangular channels, with different width-to-depth ratios and fixed-beds, is obtained. Also maximum and mean values of the bed and bank shear stress, and their dependence on the width-to-depth ratio, are presented. For width-to-depth ratios larger than 12.5 the maximum bed shear stress appeared to equal the two-dimensional boundary shear stress. Regarding the boundary shear stress, this implies that for such channels the central flow region can be treated as two-dimensional. Graphs and results can be found in Cruff [1965].

2.3 Knight [1994]

Relations for the mean- and maximum bed and -bank shear stress are obtained empirically (by curve-fitting) by Alhamid [1991]. Though always is referred to the untraceable article of Knight [1994]. The relations are based on flume experiments in a simple straight trapezoidal open channel with different base widths and constant side slopes of 1:1. A different roughness is applied to the side slopes. Local boundary shear stresses are measured using Preston Tubes. It is unclear which maximum shear stresses are meant, most likely these are the average in time and maximum in space values. Moreover, I recognized that important limitations have been omitted. Firstly, the equations contain a 'variable' that represents the bank slope although the data set only contains a 1:1 slope. Secondly, it is stated that the ratio between the bed and bank perimeter is sufficient to capture the geometry. Consequence of using this ratio is that the equations are limited to symmetrical channels. Given this limitations and since one has barely influence on the users of its equations, one should consider if it is wise to pose such equations. Duarte [2008] checked Knight's equations with his own data and concluded the equations to be reinforced by it. However, the average two-dimensional boundary shear stress instead of the cross sectional averaged boundary shear stress (Section 3.1) is used and the relative length of the bank is implemented incorrectly. I recognized and corrected those mistakes. The corrected results show that the equations are not at all supported by the data of Duarte [2008].

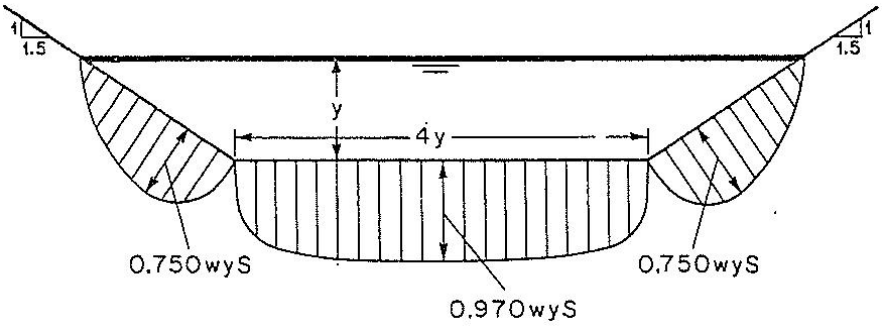

Figure 3: Sketch of the bank shear stress distribution including relations for the maximum bank and bed shear stresses (`Chow [1959]`)

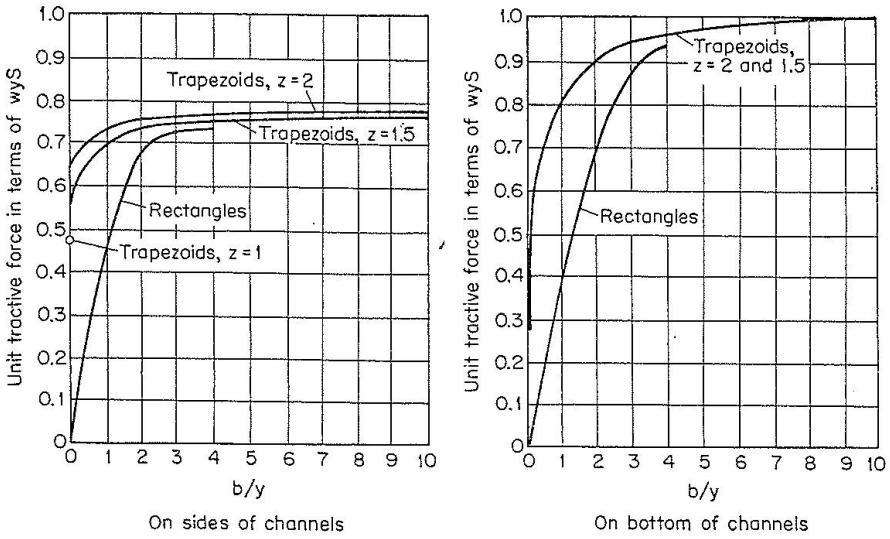

Figure 4: Maximum bank and bed shear stress (unit tractive force) for increasing width to depth ratio, `Chow [1959]`

2.4 Duarte [2008]

In a flume in Lausanne (Figure 5) `Duarte [2008]` tested the influence of bank inclination and roughness on the near-bank flow patterns. The measurements were carried out using the Acoustic Doppler Velocimetry Profiler (ADVP), which also provided information about the turbulent fluctuations. For straight channel sections it is found that (1) trapezoidal channels have fewer circulations cells and; (2) the bank shear stress increases with increasing outer-bank roughness. For curved channel flow the bank inclination and roughness have a strong effect on the (size of the) outer-bank cell, which constrains the center region cell. In curved flow with vertical banks the outer-bank cell increases with increasing outer-bank roughness. In curved flow with an inclined outer-bank this is not the case.

2.5 Ottevanger [2013]

Using Large Eddy Simulation (LES), `Ottevanger [2013]` assessed the dependency of the secondary flow processes on the curvature and parameterized the bank shear stress for the use in 1DH models. The strength of the center-region circulation cell (Section 3.2.1) was found to be linearly dependent on the curvature for mildly curved flows and reached a maximum for strongly curved flows (Figure 6). The strength of the outer-bank cell remained constant for mildly curved flows and increased in strength for intermediate and strongly curved flows (Figure 7). The mean outer-bank shear stress is described for curved open channels by Equation 1. The general equation for straight channel flow is adapted by using the depth-averaged velocity near the bank instead of the cross sectional averaged velocity and by adding a correction factor, accounting for the complex outer-bank hydrodynamics. The axisymmetric correction factor is obtained by curve-fitting using 60 axisymmetric LES-results. Axisymmetric cases with a horizontal bathymetry and different curvatures and flow depths are used. In the LES-models, the boundary shear stress is coupled to the flow field by means of a wall function. In the conclusion of this thesis, `Ottevanger [2013]` states that the research only considered rectangular cross-sections and "*further investigation is required in order to extend the bank shear stress parameterization to naturally meandering flows.*"

$$\begin{aligned} \tau_{bank,straight} &= \rho C_{f,bank} V_s^2 \\ \tau_{bank,curved\infty} &= \rho \psi_{bank,\infty} C_{f,bank} V_{s,bank}^2 \\ \psi_{bank,\infty} &\approx 2 - e^{-1.58\left(\frac{b}{R}\right)^{0.7791}} + \left(-0.6473 + 0.25 \log\left(\frac{b}{h}\right)\right) \frac{b}{R} \end{aligned} \tag{1}$$

where $C_{f,bank}$ is the friction coefficient at the bank and $\psi_{bank,\infty}$ the correction factor for axisymmetric flow. An equation is adopted to extend the correction factor for flow with developing curvature (Equation 2). This extension is tested against three different cases with developing curvature. However, dimensional analysis shows that the equation is incorrect. The equation is based on an analogy with other adaptation length equations. Further research is necessary to reassess this equation. Note that as a result of a typo, Equation 2 is different from the equation presented in the work of `Ottevanger [2013]`.

$$\psi_{bank} = \psi_{bank,\infty} + \frac{h}{2} \frac{\partial \psi_{bank}}{\partial s^2} \tag{2}$$

Figure 5: Flume in Lausanne, with an inclined rough outer-bank, as used for the experiments of `Duarte [2008]`.

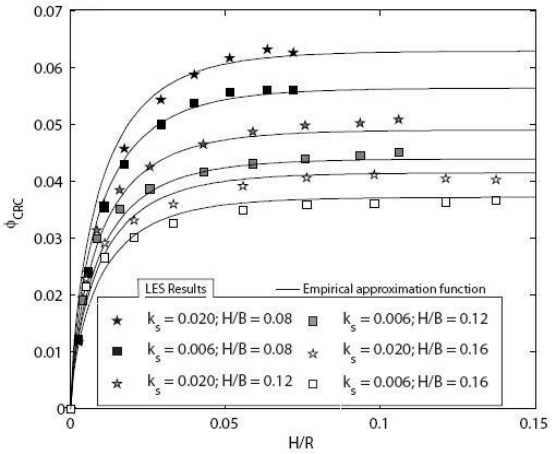

Figure 6: Strength of the center-region cell, depending on the curvature, calculated with a numerical LES model. The strength of the cell is characterized by the maximum of the stream function (`Ottevanger [2013]`).

2.6 Conclusion

`Ottevanger [2013]` states that in order to extend his bank shear stress parameterization to naturally curved flows further investigation is required. This statement is applicable for all the above described parameterizations. `Lane [1955]` is based on uniform roughened straight channels with rectangular and trapezoidal cross sections. `Cruff [1965]` is based on straight rectangular channels. `Knight [1994]` is based on straight channels with 1:1 side slopes. `Ottevanger [2013]` is based on curved axisymmetric flow cases with rectangular cross sections. Insufficient confirmation is present to prove a wider applicability of these four parameterizations. Challenge is to fill the gap between the existing paramterizations and the boundary shear stress in naturally curved flows.

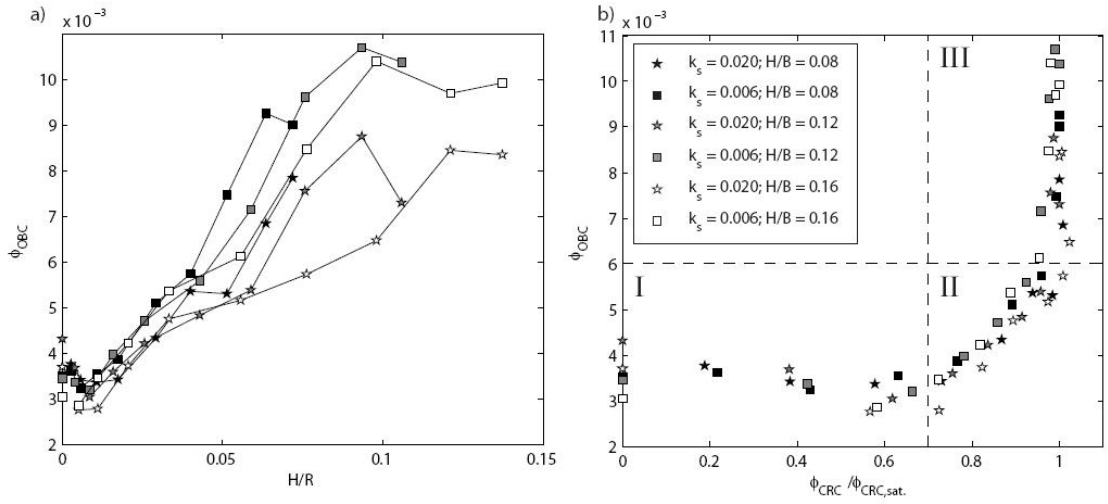

Figure 7: a) Strength of the outer-bank cell, depending on the curvature, calculated with numerical LES model. b) Comparison outer-bank, center-region cell strength (`Ottevanger [2013]`).

3 Theoretical Background - Turbulent Flow

Modeling turbulent flows and interpreting the results, theoretical knowledge about turbulent flows is inevitable. This chapter briefly describes the important quantities in and boundary conditions of these flows. This are also the quantities/boundary conditions that determine/affect the distribution and magnitude of the boundary shear stress.

The flow is characterized by an interaction between the boundary shear stress, velocity and turbulence. Boundary conditions influence these quantities. Within the considered time scale of the flow computations (minutes) erosion is negligible. Hence, the channel geometry, boundary roughness and up and downstream flow conditions can be regarded as boundary conditions (Figure 8). Below is elaborated on the flow quantities, boundary conditions and their dependencies.

3.1 Boundary Shear Stress

The boundary shear stress is the unit flow force exerted on the flow boundaries. According to Newton's third law, this implies that the boundary shear stress corresponds with the out of the flow domain transferred momentum. The cross sectional averaged boundary shear stress can thus be obtained using the momentum balance (Equation 3).

$$\tau_0 = -\frac{d}{ds}\left[\left(\rho\int_{\mathtt{A}} v_s^2 \mathtt{dA} + \int_{\mathtt{A}} p\,\mathtt{dA} + \rho g\int_{\mathtt{A}} z\,\mathtt{dA} + \int_{\mathtt{A}} \tau_{nz}\,\mathtt{dA} + \int_{\mathtt{A}} \tau_{zn}\,\mathtt{dA}\right)/P\right] \tag{3}$$

where τ_0 is the cross sectional averaged boundary shear stress and z is the vertical coordinate. For uniform flow, the equation simplifies to Equation 4.

$$\begin{aligned}\tau_0 &= -\frac{d}{ds}\left[\left(\rho g\int_{\mathtt{A}} z\,\mathtt{dA}\right)/P\right] \\ &= \rho g R_h I_e\end{aligned} \tag{4}$$

where R_h is the hydraulic radius and $I_e \equiv sin(\theta) - \frac{1}{\rho g}\frac{\partial p}{\partial s}$ is the streamwise energy slope. Generally, the notation τ_0 is also used for the average two-dimensional boundary shear stress (Equation 5). The average two-dimensional boundary shear stress applies for rough calculations in wide channels, but should not be confused with the cross sectional averaged boundary shear stress. By definition the average two-dimensional boundary shear stress is larger than the cross sectional averaged boundary shear stress.

$$\tau_{0,2D} = \rho g h I_e \tag{5}$$

where h is the water depth. The local boundary shear stress depends on the velocity gradient perpendicular to the boundary surface and the viscosity close to the boundary (Equation 6). Averaging the local boundary shear stresses in space lead to the cross sectional averaged boundary shear stress.

$$\begin{aligned}\tau_b &= -\rho\nu\frac{\partial v_s}{\partial z} \\ &= -\rho(\nu_m + \nu_t)\frac{\partial v_s}{\partial z}\end{aligned} \tag{6}$$

where τ_b is the local boundary shear stress, ν the kinematic viscosity (consisting of a molecular and a turbulent part) and $\frac{\partial v_s}{\partial z}$ the velocity gradient perpendicular to the boundary. Since the turbulent viscosity (as defined by `Boussinesq [1877]`) close to the boundary can be assumed

negligible compared with the molecular viscosity and the molecular viscosity can be assumed constant, (spatial) variations in the boundary shear stress are attributed to variations in the 'near boundary velocity gradient'. Where 'near boundary' is defined as within the viscous sublayer.

Integrating the velocity gradient, the velocity profile perpendicular to the boundary can be obtained. Knowing a velocity in the viscous sublayer, the local boundary shear stress can be simply obtained by Equation 7.

$$\frac{\bar{v_s}(z)}{u_*} = \frac{u_* z}{\nu} \tag{7}$$

where $\bar{v_s}(z)$ is the Reynolds averaged velocity at a distance z from the boundary and $u_* = \sqrt{\tau_b/\rho}$ is the local shear velocity. Further away from the boundary in the buffer-, inner- or outer layer turbulence is non-negligible. Here more assumptions have to be made and different relations between the velocity and boundary shear stress need to be applied. These relations are validated for cases with a smooth boundary. Considering a rough boundary again other relations need to be applied. Similarity between all these relations is that they contain the velocity at a certain distance from the boundary and a description of the viscosity profile. Derivations can be found in Appendix B. Note that they all have their limitations.

Since boundary shear stress can be defined as the out of the flow domain transferred flow momentum (Equation 3), variations in the boundary shear stress correspond with the distribution of flow momentum and thus (1) the geometry of the channel, (2) the (distribution of the) boundary roughness along the perimeter and (3) the streamwise velocity and turbulence distribution at the up- and downstream boundaries. All three affect the streamwise velocity- and turbulence distribution in the considered channel, which interact with the local boundary shear stress distribution (Figure 8).

3.2 Velocity Field

Interaction between the (or exchange of) water particles transfers the effect of a solid boundary into the flow and determines the (streamwise) flow velocity field. A distinction can be made between interactions on molecular level (the molecular scale) and interactions on a larger level (the flow scale). The interactions on the molecular scale can be regarded to be an intrinsic property of the fluid and independent of the flow properties. These interactions are in fluid dynamics always parameterized by the molecular viscosity. The interactions on the flow scale can be divided into turbulence and currents perpendicular to the main flow (secondary currents). The influence of the solid boundary on the flow field, implying a reactive force, depends on these interactions. Without any interaction the flow would accelerate infinitely. Only considering the interactions on the molecular scale will lead to an equilibrium flow field with unrealistically large flow velocities. Taking also the turbulence into account leads to flow velocities with a realistic order of magnitude. As well taking the secondary currents, also contributing to the interaction, into account will lead to even slightly lower flow velocities. Besides that the interactions determine the average flow velocity, the nature of the interactions also determine the distribution of the flow velocities.

3.2.1 Secondary Velocity

Secondary velocities (cross stream motion) are found in both straight and curved channels. Relative to the streamwise velocities, the secondary velocities are small which would hypoth-

esize a marginal influence on the bank shear stress. However, since the secondary currents redistribute the streamwise momentum its influence can be significant. A distinction can be made between circulatory and translatory parts of the cross stream motion (`Blanckaert and De Vriend [2004]`). The translatory part, also named meander currents or cross flow, is mainly pressure induced (`Blanckaert and De Vriend [2004]`). `Prandtl [1952]` classified the circulatory part in two categories. (1) Prandtl's first type is defined as secondary circulations induced by the local imbalance between the centrifugal and the pressure force in curved channels. This type of secondary circulations can be imagined intuitively and these circulations are found in both laminar and turbulent curved flows (`Nezu [1993]`). (2) Prandtl's second type is defined as secondary circulations induced by turbulence anisotropy and inhomogeneity. The mechanisms behind the secondary circulations can be assessed by means of the downstream vorticity equation as in `Blanckaert and De Vriend [2004]` (Equation 8).

$$
\begin{aligned}
\omega_s =& \frac{\partial v_z}{\partial n} - \frac{\partial v_n}{\partial z} \\
\frac{\partial \omega_s}{\partial t} =& \frac{\partial^2 v_z}{\partial n \partial t} - \frac{\partial^2 v_n}{\partial z \partial t} \\
=& \underbrace{-\left(\frac{1}{1+n/R} v_s \frac{\partial \omega_s}{\partial s} + v_n \frac{\partial \omega_s}{\partial n} + v_z \frac{\partial \omega_s}{\partial z}\right)}_{I} + \underbrace{\frac{1}{1+n/R} \omega_s \frac{\partial v_s}{\partial s}}_{II} \\
&+ \underbrace{\left(\omega_n \frac{\partial v_s}{\partial n} + \omega_z \frac{\partial v_s}{\partial z} + \frac{1}{1+n/R}\frac{v_n \omega_s}{R} - \frac{1}{1+n/R}\frac{v_s \omega_n}{R}\right)}_{III} - \underbrace{\frac{1}{1+n/R}\frac{\partial}{\partial z}\left(\overline{v_s'^2}\right)}_{IV} \\
&+ \underbrace{\frac{\partial^2}{\partial z \partial n}\left(\overline{v_n'^2} - \overline{v_z'^2}\right) + \frac{1}{1+n/R}\frac{1}{R}\frac{\partial \overline{v_n'^2}}{\partial z}}_{V} \\
&+ \underbrace{\left(\frac{1}{1+n/R}\frac{\partial^2}{\partial z^2} - \frac{\partial}{\partial n}\left(\frac{1}{1+n/R}\frac{\partial}{\partial n}\right)\right)\left((1+n/R)\,\overline{v_n' v_z'}\right)}_{V} \\
&+ \underbrace{\frac{\partial}{\partial z}\left(\frac{1}{1+n/R}\frac{\partial \overline{v_s' v_n'}}{\partial s}\right) + \frac{\partial}{\partial n}\left(\frac{1}{1+n/R}\frac{\partial \overline{v_s' v_z'}}{\partial s}\right)}_{VI} \\
&+ \underbrace{\nu_m\left(\nabla^2 \omega_s + \frac{2}{(1+n/R)^2}\frac{1}{R}\frac{\partial \omega_n}{\partial s} - \frac{1}{(1+n/R)^2}\frac{1}{R^2}\omega_s\right)}_{VII}
\end{aligned}
\tag{8}
$$

The equation represents the vorticity equation in a cylindrical coordinate system. Where (I) represent the advective terms, (II) the vortex stretching, (III) the circulations of Prandtl's first type, (IV) the turbulence related centrifugal term, (V) the circulations of Prandtl's second type, (VI) is due to the downstream non-uniformity of the flow and (VII) represents dissipation by molecular interactions. While, ω_n and ω_z are defined by Equation 9.

$$
\begin{aligned}
\omega_n &= \frac{\partial v_s}{\partial z} - \frac{1}{1+n/R}\frac{\partial v_z}{\partial s} \\
\omega_z &= \frac{1}{1+n/R}\frac{\partial v_n}{\partial s} - \frac{\partial v_s}{\partial n} - \frac{1}{1+n/R}\frac{v_s}{R}
\end{aligned}
\tag{9}
$$

Part (III) in Equation 8 shows us that the circulations of Prandtl's first type increase with increasing curvature and increasing cross stream gradients in the streamwise velocity. Considering a straight ($R = \infty$) axisymmetric ($\frac{\partial}{\partial s} = 0$) channel, eliminating circulations of Prandtl's first type, leads to equation 10. The equation shows us that the inhomogeneity of the turbulent shear stresses ($\overline{v_n' v_z'}$) and the turbulence anisotropy ($\overline{v_n'^2} - \overline{v_z'^2}$) account for the circulations of Prandtl's second type. Hence, turbulence generating secondary currents requires the transfer of energy from turbulence to the mean flow (`Blanckaert and De Vriend [2004]`).

$$\frac{\partial \omega_s}{\partial t} = \text{Advective terms} + \frac{\partial^2}{\partial z \partial n}\left(\overline{v_n'^2} - \overline{v_z'^2}\right) + \left(\frac{\partial^2}{\partial z^2} - \frac{\partial^2}{\partial n^2}\right)\left(\overline{v_n' v_z'}\right) + \text{Viscous terms} \qquad (10)$$

`Blanckaert and De Vriend [2003]` recognize two important secondary circulation cells in river bends. The center region and outer-bank cell (Figure 9).

Center Region Cell To lead the flow through a bend, continuously changing the direction of the flow, an inward directed force is required. This force is generated by a transverse water level gradient. Considering a cross section in a river bend, the situation can be described by imposing an outward directed centrifugal force and an inward directed pressure gradient. Because in contrast with the pressure gradient, the centrifugal force is not constant over depth, a transverse circulation cell develops (in this report referred to as center-region circulation cell but most commonly known as classical helical motion or spiral flow). The center-region cell, which is thus a secondary circulation cell of Prandtl's first type, redistributes streamwise momentum, affecting boundary shear stresses and sediment transport and therefore it shapes the bed topography and enhances mixing (`Blanckaert and De Vriend [2003]`). The strength of the cell depends on the radius of curvature and the vertical profile of the centrifugal force and thus the vertical profile of the downstream velocity. Increasing the depth generally leads to an increase in velocity differences, thus in most models the secondary flow strength is prescribed to increase linearly with h/R. However, secondary flow not only depends on the vertical streamwise velocity profile but it also affects it. As a result of the advective momentum transport by secondary flow, the downstream velocity profile flattens. "*This reduces the non-uniformity of the centrifugal acceleration and limits the strength of the secondary flow.* (`Blanckaert and De Vriend [2011]`)" This nonlinear interaction is referred to as saturation of secondary flow.

Outer-Bank Cell The outer-bank cell is a near bank circulation cell creating a buffer layer between the stronger center-region cell and the river bank (Figure 9). The outer-bank cell is induced by turbulence anisotropy and by the local imbalance between the centrifugal and the pressure force. The centrifugal force favors the outer-bank cell due to a non-monotonic vertical velocity profile. The outer-bank cell is enhanced by turbulence anisotropy, which is induced by the proximity of the flow boundary (`Blanckaert and De vriend [2004]`). Although the existence of the outer-bank cell has already been observed decades ago, knowledge about the conditions of occurrence is state of the art. `Blanckaert and De Vriend [2011]` investigated the relative importance of the outer-bank cell and its dependence on curvature, bank inclination and bank roughness. They revealed that outer-bank cells occur in over 30 degrees inclined banks (angle β in Figure 2); that they are observed from the bend entrance and retain a quasi-constant width from about 60 degrees in the bend (angle α in Figure 2); and that the relative importance of the cell increases with increasing curvature (thus decreasing radius of curvature), bank roughness and bank steepness. The dependence of the outer-bank cell strength on the curvature is shown in Figure 7a. Subsequently it displays a region where the outer-bank cell remains constant or even decreases for an increasing curvature, a region where the outer-bank cell increases. For

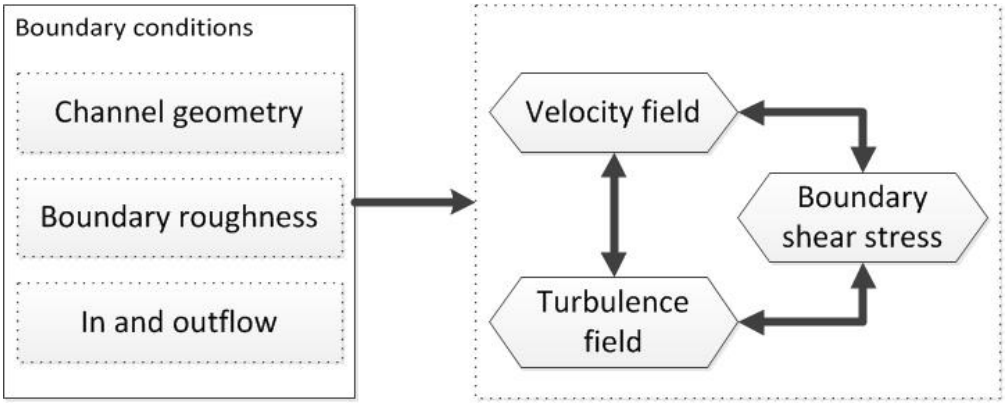

Figure 8: Recognized flow quantities and boundary conditions in turbulent flow.

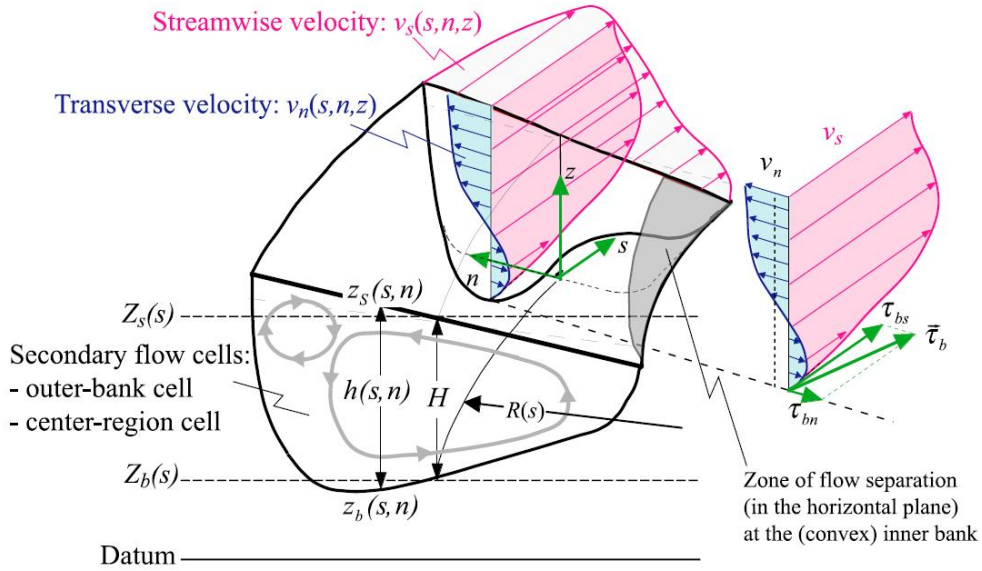

Figure 9: Sketch of a river bend, showing the rotation cells (`Blanckaert and De Vriend [2003]`)

very sharp river bends ($h/R > 0.1$) the outer-bank cell is roughly constant (Ottevanger [2013]).

Figure 7b shows the comparison between the outer-bank cell and the center-region cell strength. Three regions can be distinguished: The first region, indicating the mild curvature case, only shows an increase of the center-region cell strength; the third region, indicating strong curvature cases, only shows an increase in outer-bank shear strength; the second cell, indicating intermediate curvature cases, shows a correlation between the center-region cell strength and the outer-bank cell strength. "*The explanation of the strength of the outer-bank cell in the three zones is as follows: In the first zone (I) the outer-bank cell is driven by turbulence anisotropy; in the second zone (II) the outer-bank cell is also influenced by momentum transfer from the center-region cell; in the third zone (III) it grows in size and receives more momentum from the center-region cell.* (Ottevanger [2013])"

One concluding remark should be placed concerning the effect of the outer-bank cell on the forces acting on the outer-bank. It is suggested that the outer-bank cell creates a buffer layer between the center-region cell and the river bank, thus inhibiting the forces on the bank. However, the outer-bank cell leads to a locally enhanced production of turbulent shear stresses in the cross sectional plane (Van Balen [2010]), which might enhance the force on the bank. Ottevanger [2013] observed that the outer-bank cell causes an increase of the bank shear stress in the lower half of the water column caused by the transfer of high streamwise momentum to the toe of the bank. "*The overall effect of the outer-bank cell on the bank stability can however not be determined (with the concerning LES model) as this would require a flow simulation lacking the outer-bank cell.* (Ottevanger [2013])"

Remark To get insight in the effect of the secondary circulations on the streamwise flow field and boundary shear stress, the author started to assess the problem analytically on the basis of simplified advection-diffusion equations. For details, a provisional description of the model including some results can be found in Appendix F.

3.2.2 Internal Shear Forces

Internal shear forces, due to molecular interaction and turbulence, influence the velocity distribution. Both can be considered as a viscosity. This is further assessed in Section 3.3.

3.3 Turbulence Field

Turbulence is an important phenomenon distributing and dissipating flow momentum and energy. Regarding the local boundary shear stress, it can be stated that high turbulent kinetic energy close to a boundary enhances high velocities near that boundary which increases the local boundary shear stress. Referring to Equation 6, high turbulent kinetic energy implies a high value for the turbulent viscosity which represents an effective transfer of momentum from the core to the boundary. In the previous subsection this mechanism is referred to as 'internal shear force'. Secondly, in the previous subsection turbulence anisotropy and inhomogeneity as a mechanism generating secondary currents is discussed. These turbulent properties are mainly driven by channel geometry.

3.3.1 Sharp Open Channel Bends

Blanckaert and De Vriend [2005] assessed the turbulence structure in sharp open channel bends. Their study based on flume experiments suggested turbulence damping by streamline

curvature. The decrease of turbulence activity favors width-coherent fluctuations. "*When treated as turbulence, it* [width-coherent fluctuations] *contributes significantly to the turbulent normal stresses, but little to the turbulent shear stresses.* (`Blanckaert and De Vriend [2005]`)" Since this phenomenon leads to fewer shear generation, it is important in affecting the forces exerted on the flow boundaries.

3.3.2 Turbulent Viscosity

In analogy with molecular viscosity, turbulence can be represented by a viscosity. Hence, in numerical modeling, the viscosity consists of three components: (1) the molecular viscosity, (2) the sub-grid turbulent viscosity and (3) the resolved turbulent viscosity. To get the internal shear stress decreasing linearly from maximum at the wall to zero at the flow surface the viscosity should meet Equation 11.

$$\rho u_*^2 \left(1 - z/h\right) = \rho \left(\nu_m + \nu_{sgs} + \nu_{t,res}\right) \frac{\partial \overline{v}(z)}{\partial z} \tag{11}$$

where ν_m is the molecular viscosity, ν_{sgs} the sub-grid turbulent viscosity and $\nu_{t,res}$ the resolved turbulent viscosity. (1) The molecular viscosity is an intrinsic property of the fluid and independent of the flow properties and thus constant in space. (2) The sub-grid turbulent viscosity represents the turbulence that is not captured by the grid and should be included in the Navier-Stokes Equations with a closure model. As turbulent closure model, in Large Eddy Simulation (Chapter 4) the Smagorinsky Model is used. The grid size in the numerical model is chosen such that the sub-grid turbulence can be assumed homogeneous and isotropic. This allows us to define the sub-grid viscosity using the size of the grid cells and the sub-grid shear stresses (Equation 12). A damping function could be used to make the turbulent viscosity zero at solid boundaries, which is necessary when the ghost cell is located in the viscous sublayer or buffer layer. Changes in the sub-grid model, such as using the Dynamic Smagorinsky Model, only lead to minor differences (`Van Balen [2010]`).

$$\begin{aligned} \nu_{sgs} &= \left(\underbrace{C_s \Delta}_{lengthscale}\right)^2 \underbrace{\left|\tilde{S_{ij}}\right|}_{rateofstrain} \\ \tilde{S_{ij}} &= \frac{1}{2}\left(\frac{\partial \bar{v_i}}{\partial x_j} + \frac{\partial \bar{v_j}}{\partial x_i}\right) \end{aligned} \tag{12}$$

(3) The resolved turbulent viscosity represents the turbulence that is captured by the grid and can be expressed by Equation 13.

$$\begin{aligned} \rho \overline{v'w'} &= -\rho \nu_{t,res} \frac{\partial \overline{v}}{\partial z} \\ \nu_{t,res} &= \frac{\overline{v'w'}}{\frac{\partial \overline{v}}{\partial z}} \end{aligned} \tag{13}$$

3.4 Channel Geometry

On the considered time scale, the location of the flow boundaries is a main constrain of the flow. The channel geometry has, however, a broad variety. The geometry of natural channel bends is non-uniform, in streamwise and cross stream direction, with deep pools in the outer bends and bars in the inner bends. Dunes and mid-channel bars might be present, while in fast

flowing rivers anti-dunes can arise. Moreover, the bank geometry and width-to-depth ratio can vary. In the scope of the present study, this broad variety needs some generalization. Since, only axisymmetric channels are considered, all the streamwise non-uniformities can be left out. The three important remaining variables are the bank geometry, the transverse bed slope and a streamwise bed slope.

3.4.1 Bank Geometry

As mentioned in Section 1.1, a river bank can be described consisting of a vertical cohesive upper bank and an inclined lower bank. When referred to the bank, sometimes only the steep upper bank is meant. Similar to `Duarte [2008]` the inclined lower bank is also meant when referred to bank. From previous research the following can be said about the effect of the outer-bank on the flow and boundary shear stress. With a decreasing outer-bank angle (1) "*the bed shear stress evolution presents less peaks although wider and* (2) *the maximum bank shear stress gets closer from the bank toe.* (`Duarte [2008]`)" The secondary current structure (which directly influences the boundary shear stress distribution) for a trapezoidal channel is different from a rectangular channel, (`Tominaga [1989]`).

3.4.2 Transverse Bed Slope

Because of the interplay between secondary currents (or transverse flow forces) and the gravitational force, in an alluvial river bend a transverse bed slope develops, with deep pools near the outer-bank and shallow shoals near the inner-bank. Roughly spoken, as a result of internal shear forces (Section 3.2.2) the highest flow velocities occur where the channel is deepest, referred to as topographic steering. In an alluvial river bend this implies high flow velocities near the outer-bank. Topographic steering is a very important phenomena distributing the flow. Not including the transverse bed slope in a model, but assuming a flat bed can lead to a completely different flow velocity field. In this case, it might occur that because the longitudinal water level gradients are largest in the inner bend, the largest velocities are found in the inner bend. This mechanism is called potential vortex distribution. Analytically, the transverse bed slope can be derived from the balance between transverse flow forces and the gravitational force (Appendix C). Here a sinusoidal profile is adopted.

$$h = h_m \left(1 + \frac{b}{\pi}\frac{A}{R}\sin\left(\frac{\pi}{b}n\right)\right) \tag{14}$$

where: h is the water depth, h_m the mean water depth, b the channel width, R the radius of the bend, A a dimensionless scour factor and n the transverse location.

Remark To get insight in the effect of the geometry on the flow field and boundary shear stress, the author started to assess the problem analytically using Green's and Mapping Functions. This research is still ongoing. A provisional description of the model can be found in Appendix F.

3.4.3 Streamwise Bed Slope

The flow in natural rivers is forced by a longitudinal bed slope. Per unit of channel length this force is shown by Equation 15. The forcing term can also be rewritten as a momentum source.

$$F = \rho g A I_b \tag{15}$$

In equilibrium conditions dividing by the perimeter gives the cross-sectionally averaged boundary shear stress, τ_0. In curved reaches the longitudinal bed slope is steeper in the inner bend than

in the outer bend. This phenomena is known as potential vortex distribution. The longitudinal bed slope is inverse proportional with the length of the longitudinal domain and this length is proportional with the radius of curvature.

3.5 Boundary Roughness

The boundary roughness (distribution) describes the nature of the interface between the flow and the boundary. Apart from that the boundary roughness enhancing the outward transfer of momentum at the wall, leading to lower velocities close to the wall, it might also enhance turbulence and coherent structures. `Tominaga [1989]` concluded that the basic structure of the secondary currents near the bank did not considerably change for different (differential) boundary roughness. While `Duarte [2008]` concluded that with increasing outer-bank roughness relative to the bed roughness: "(1) *the number of circulation cells increase;* (2) *the circulation cells intensity increase;* (3) *the maximum downstream velocity increase, at about channel center;* (4) *the bed mean and maximum shear stresses decrease whereas bank mean and maximum shear stresses increase;* (5) *the maximum bank shear stress shifts closer to the bank toe;* (6) *the turbulent kinetic energy (tke) over the bank increases and shifts the tke maximum value from the channel center outwards.* (`Duarte [2008]`)"

Remark To get insight in the effect of the boundary roughness on the flow field and boundary shear stress, the author started to assess the problem analytically on the basis of an hypothetical case. The model gives interesting results. Given the amount of assumptions, the physical basis of the model is, however, weak. Among others, assumptions made regarding the mixing length could be improved. A provisional description of the model including some results can be found in Appendix F.

3.6 In and Outflow

The amount of water entering the considered channel section, its velocity and turbulence field and backwaters effects from downstream are of major importance in determining the flow properties within the channel section. For spatially developing flows one should pose the up- and downstream boundary conditions with great care. For axisymmetric channels the boundary conditions can be replaced by periodic boundary conditions.

4 Methodology

This chapter gives an overview of the numerical calculations, the physical experiments to compare the results with, the computational algorithm, how to test the performance of the computational algorithm (research question four) and the hardware used to make the computations.

4.1 Calculations and Experiments

Scientifically, knowledge can be obtained by (1) field measurements, (2) physical models, (3) numerical models or (4) analytical models. As all the four methods have different disadvantages, scientific work is often based on at least two of the them. The aimed knowledge is obtained by numerical calculations and compared with physical experiments.

Seven calculations are considered to be sufficient to answers the first three research questions (Tables 1 and 2). Less than seven calculations would also be enough. Though, since experimental data is available to support the carried out calculations, there is chosen to make seven calculations. Comparing Calculations N16_30_00, N16_30_02 and N16_30_30 answers research question one. Comparing Calculations N16_45_02 and N16_30_02 answers research question two. Comparing Calculations N16_30_02 and N16_30_02TBS answers research question three. To prevent the difficulties and variety of developing flow case, similar to `Ottevanger [2013]`, the calculated cases are axisymmetric. With Equation 14 the transverse bed slope of Calculation N16_30_02TBS is implemented.

`Duarte [2008]` carried out physical experiments in flume bends with an inclined and roughened outer-bank. The first six numerical calculations I made are based on these physical experiments and therefore the results can be compared. Apart from the straight inflow and outflow reaches, the geometries of the numerical calculations and physical experiments are identical. However, yet no experiment measuring the boundary shear stress in a bend with a transverse bed slope is available. Therefore, at the moment, research question three can not be compared with data from physical experiments.

The nomenclature is identical as in `Duarte [2008]`. In the naming of a case N refers to the data source from a numerical model; the first number refers to the water depth; the second number to the inclination of the outer-bank; the third number to the roughness height of the outer-bank; and TBS refers to the implementation of a transverse bed slope.

Remark To get to the cases hundreds of calculations made. Some of these simulations will be referred to in this thesis. All the simulations referred to are listed in Appendix E.

4.2 Computational Algorithm (Software)

The computational algorithm, where the results of this thesis are based on, carries on the work of `Ottevanger [2013]`, `Van Balen [2010]`, `Eggels [1994]` and `Pourquié [1994]`. The algorithm consists of tens of thousand rows of, mainly uncommented, code in FORTRAN. The algorithm is divided into different subroutines. The main file calls the different subroutines. By including/excluding specific subroutines, the modeler can accommodate the algorithm to suit its desired calculations. I worked through the code, made adaptations, removed unnecessary parts and wrote a manual in order to improve the performance of the algorithm, decrease the computational costs, make the code more understandable and improve the usability of it. This

section briefly addresses the algorithm. For a complete overview of the algorithm, please go to the manual (Appendix D).

4.2.1 Basics

The computations are three-dimensional Large Eddy Simulations (LES), since Direct Numerical Simulations (DNS) are computationally too expensive and Reynolds Averaged Navier-Stokes (RANS) computations do not allow energy transfer from turbulence to the main flow. The latter is essential to capture circulations of Prandlts second type. In Large Eddy Simulation the macro-scale anisotropic turbulence is captured with a sufficiently small grid. This allows energy transfer from the macro-scale turbulence to the main flow. For closure of the sub-grid motion the Smagorinsky Model is used. The sub-grid model only allows for dissipation of energy. The latter is justified since the small-scale turbulence is mainly important because it withdraws energy from the large scale motion (`lecture notes CIE5312`).

The pressure-correction method is used, because the water level is imposed as a rigid-lid and the flow is not assumed hydrostatic. This method consists of two steps. Firstly, the flow field is solved using the momentum equations but violating the non-divergence criterion (predictor step). Secondly, correction of the velocity field is computed through the pressure field (corrector step). Solving the pressure equation is thus required here. Which is achieved by including a Pressure Poisson Solver.

The numerical scheme used is the second order explicit Adams-Bashfort. Semi-implicit schemes did not result in a significant gain in time step and fully explicit methods, as Adams-Bashfort, greatly simplify the imposition of the boundary and the parallelization of the model (`Balaras [2004]`).

4.2.2 Boundary Conditions

For the free surface, the free-slip condition and the rigid lid approximation are applied. The latter means that at the free surface (the rigid lid) instead of $w \neq 0$ and $p = 0$, $w = 0$ and $p \neq 0$ are applied. This approximation leads to a deviation between the solution of the numerical algorithm and reality. This deviation is small when the super elevation of the free surface is small with respect to the channel depth (`Demuren and Rodi [1986]`).

Since the calculations are axisymmetric, at the up and downstream boundary, periodic boundary conditions can be used. This means that the velocity, viscosity and pressure in the most upstream grid points are equal to them in the most downstream grid points. Note that this requires a sufficiently long longitudinal length of the domain. Based on the results of `Van Balen [2010]` and `Ottevanger [2013]` the longitudinal length is chosen to be equal to the width of the bend. Where the width of the bend is defined as the difference between the radius of curvature of the outer and inner bank at the water level.

At the solid boundaries also the free-slip condition is applied. The effect of friction is added on the basis of a wall function. For grid aligned boundaries this method is quite straightforward and referred to as the Normal Wall Function Approach. Knowing the location of the ghost cell (the grid point bordering the boundary) and its velocity, using Newtons Law, the amount of

momentum can be easily subtracted according to Equation 16.

$$\begin{aligned} v_{new} &= v_{old} - \Delta v \\ &= v_{old} - \frac{u_*^2 \Delta t}{\Delta z} \end{aligned} \tag{16}$$

where v_{old} is the velocity in the ghost cell before subtracting the 'momentum loss' and Δz is the grid size of the boundary grid cell in the direction perpendicular to the wall. Note that u_* is calculated using v_{old}. The absolute value of v_{new} is thus too small with respect to the boundary shear stress. In the following time step this will lead to too much momentum transport from the bordering fluid cell(s) towards the boundary fluid cell and finally the velocities in the whole flow domain are slightly underestimated. This problem could be solved by calculating u_* using v_{new}. This requires an extra iteration step and thus additional computational costs. Moreover, when $\Delta v << v_{old} \approx v_{new}$, which is generally the case, the made error is negligible. Two test calculations, one with and one without the additional iteration step, are compared and the relative difference between the two was in the order of 10^{-3} (Calculations HoT1 and HxT1, see Appendix E).

Non-grid-aligned/complex boundaries require a more sophisticated boundary method. `Balaras [2004]` proposed a method for complex boundaries through a Cartesian grid. This Immersed Boundary Method is by `Mittal et al. [2005]` specified as the Ghost Cell Finite Difference Approach. In the method the embedded solid boundary is represented by a body force in the fluid velocity grid points bordering the boundary, referred to as ghost cell (Equation 17). This body force is calculated hypothesizing a velocity, $\hat{v}_i^{n+1}$, for the ghost cell (Equation 18).

$$\frac{v_i^{n+1} - v_i^n}{\Delta t} = RHS_i + f_i \tag{17}$$

$$f_i = -RHS_i + \frac{\hat{v}_i^{n+1} - v_i^n}{\Delta t} \tag{18}$$

where RHS is the right hand side of the momentum equation, including the advection, diffusion and pressure term. Combining Equation 17 and 18 leads to $v_i^{n+1} = \hat{v}_i^{n+1}$. The forced velocity in the ghost cell is obtained by means of fitting a wall function through the ghost cell and an interpolated point lying on the line perpendicular to the boundary and through the ghost cell. This interpolated point (point I in Figure 10) represents the surrounding velocity grid points. Obtaining the flow parameters in point I requires, besides interpolation, a local rotation of the grid. An extensive description of the procedure can be found in Appendix D. One of the main adaptations of the author is in the representation of this body force (in the algorithm Subroutine `fluidcell`). Combining Equation 17 and 18 shows that the body force can easily be included according to Equation 19.

$$\begin{aligned} RHS_i + f_i &= \frac{v_i^{n+1} - v_i^n + \Delta t \left(RHS_i - \frac{\hat{v}_i^{n+1} - v_i^n}{\Delta t} \right)}{\Delta t} \\ &= \frac{v_i^{n+1} - \hat{v}_i^{n+1} + \overbrace{\Delta t \left(RHS_i \right)}^{\text{Missing}}}{\Delta t} \end{aligned} \tag{19}$$

The denoted part was missing in previous versions of the algorithm. I recognized and corrected this. This correction also required some adjustments in other subroutines (Appendix D). Note that by including the incorrect Subroutine `fluidcell` twice in the algorithm, for equilibrium

flow, this mistake does not lead to a major deviation in the flow field. However, since it was not properly documented, in previous research the concerned subroutine was not always included twice.

Remark 1 Known is that with the Normal Wall Function Approach the momentum that is subtracted from the flow equals a value that is based on the flow velocity in the ghost cell (Equation 16). With the Immersed Boundary Method the subtracted momentum equals the momentum fluxes from the surrounding fluid cells towards the ghost cell, while the flow velocity in the ghost cell depends on the surrounding fluid cells. In equilibrium conditions when the wall functions are applicable on the ghost cell and surrounding fluid points, the considered momentum fluxes equal the subtracted momentum from the Normal Wall Function Approach. This, however, requires that the near wall turbulent viscosity equals the value as described by Boundary Layer Theory, κz^+ (Appendix B).

Remark 2 The boundary shear force depends among others on the the length of the boundary. Contrary, in the Immersed Boundary Method no attention is payed to the length of the boundary. The amount of momentum 'lost' at the boundary does depend on the amount and size of the ghost cells. This approximates but not (necessarily) equals the length of the boundary.

Apart from the velocity, also the turbulent sub-grid viscosity requires a boundary condition. Using the Normal Wall Function Approach the sub-grid turbulent viscosity in the ghost cell is simply calculated according to the Smagorinsky Model. The viscosity, which is defined in the cell center, is calculated using the shear stresses on the cell corners. Since four of the cell corners are located on the boundary and the 'virtual' velocities outside the boundary are defined to be equal to the velocities in the ghost cells, there is incorrectly presumed that there is no stress in that corners and consequently the sub-grid viscosity might be underestimated. This might lead to an overestimation of the discharge. Using the Immersed Boundary Method, the sub-grid turbulent viscosity in the ghost cell is defined by the function κy^+ (Appendix B). Since the resolved turbulent viscosity (Section 3.3.2) is assumed negligible in the ghost cell, this seems an appropriate boundary condition. Implementing the sub-grid turbulent viscosity this way is one of the adaptations I made. In previous versions of the algorithm, the sub-grid turbulent viscosity was made dependent on the distance from the boundary cubed and calibrated by the sub-grid viscosity in the interpolated point I (Figure 10). When point I is located in the turbulent inner layer or outer layer (Appendix B), the latter leads to an immense underestimation of the sub-grid viscosity in the ghost cell.

4.2.3 Forcing

The flow is forced by a streamwise momentum source. Written in units of velocity, this can be added to the streamwise flow velocities. Given Newton's second law of motion this leads to Equation 20.

$$\begin{aligned} F &= m \cdot a \\ \tau_b \Delta x \Delta y &= \rho \Delta x \Delta y \Delta z \frac{\Delta u}{\Delta t} \\ \rho c_f u^2 \Delta x \Delta y &= \rho \Delta x \Delta y \Delta z \frac{\Delta u}{\Delta t} \\ \Delta u &= \frac{c_f u^2 \Delta t}{\Delta z} \end{aligned} \tag{20}$$

	Flow Properties
Water Depth	0.159 m
Width At Water Line	1.3 m
Radius Of Curvature	1.7 m
Bed Roughness (k_s)	0.002 m
Inner Bank Roughness	Smooth
Inner Bank Inclination	90°
Outer-Bank Roughness	Variable (Table 2)
Outer-Bank Inclination	Variable (Table 2)
Bulk Velocity	Variable

Table 1: General properties of the proposed calculations. Note that the outer-bank inclination and roughness as well as the bulk velocity are different for the different calculations.

Name	Outer-Bank Inclination	Outer-Bank Roughness
N16_30_00	30°	Smooth
N16_30_02	30°	k_s =0.002 m
N16_30_30	30°	k_s =0.030 m
N16_45_00	45°	Smooth
N16_45_02	45°	k_s =0.002 m
N16_45_30	45°	k_s =0.030 m
N16_30_02TBS	30°	k_s =0.002 m

Table 2: Outer-bank inclination and roughness for the proposed calculations. Figure 2 shows the definition of the bank angle.

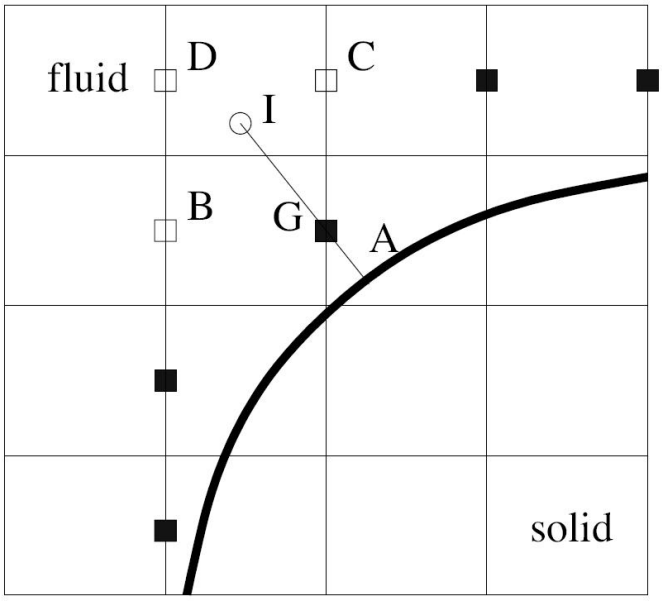

Figure 10: Showing the essence of the Immersed Boundary Method. Where the black line is the embedded boundary, the black squares the ghost cells, the white squares the other fluid points and the white round an interpolated fluid point (`Van Balen [2008]`).

Giving the desired mean velocity and guessing a friction coefficient, the forcing term can be assessed. Instead, τ_b can also be linked to a longitudinal bed slope. The potential vortex distribution (Section 3.4.3) is implemented by scaling the forcing term with the inverse of the normalized curvature. Which is the radius of curvature at a specific spot divided by the radius of curvature at the channel axis. In previous version of the algorithm, the latter was done in a dimensional incorrect way. Implementation in a dimensional correct way is one of the adaptations of the author.

4.2.4 Grid and Temporal Spacing

For all the calculations an identical structured grid has been used. The dimensions of the grid are 1.3 meter in lateral direction and 0.159 m in vertical direction. In longitudinal direction the grid is curved and the boundary conditions are periodic. Based on experience of `Van Balen [2010]` and `Ottevanger [2013]`, the length of the longitudinal domain along the channel axis is chosen to be equal to the width of the bend. Defining an equal amount of grid cells in longitudinal and lateral direction assures an aspect ratio of the grid spacing of one at the channel axis. Information about the amount and spacing between the grid points can be found in Table 3. A solid boundary is drawn through the grid. Result is that part of the grid points are in the solid domain instead of in the fluid domain.

Regarding the temporal spacing, the modeler chooses the amount of time steps (#t). Knowing the spatial grid and the instant velocities, based on the CFL-condition, each time step the algorithm determines the time spacing (dt). Given periodic boundaries and expecting some spin-up time, to get an accurate result, the flow should pass several times through the model domain. This means that the simulated time should be sufficiently long. Table 4 shows the simulated time, number of time steps, time spacing and number of times a fluid particle passes through the model domain. Without proper argumentation, based on comparison with the work of `Ottevanger [2013]`, the above described requirement is assumed to be met.

4.2.5 Summary

The model consists of a predictor step and a corrector step. In the predictor step the system of momentum equations is solved, assuming free slip conditions and taking the 'isotropic' sub-grid turbulence into account with the Smagorinsky Model, while the flow is forced by adding momentum to each grid cell and the boundary shear stress is included by means of wall functions. Subsequently, in the corrector step is solved for the non-divergence criterion. Big advantages of the algorithm are that: (1) it is build up from the ground, so the modeler controls everything; (2) the structured grid leads to straightforward easy to implement discritizations; (3) complex boundaries are easy to implement. The main challenge is on assuring the accuracy of the boundary method (Section 4.3 and Chapter 5).

4.3 Testing the Algorithm

The boundary shear stress is determined using wall functions. In Section 4.2.2 two methods that include and determine the boundary shear stress are described (the Immersed Boundary Method and the Normal Wall Function Approach). Although one method can be rewritten into the other, calculating identical cases both methods give a different answer. In order to test how accurate the algorithm is in describing the boundary shear stress, to find out what the reason is for the inaccuracy and how to improve the accuracy (research question four): (1) The over/underestimation of the boundary shear stress is tested by comparing the integrated

boundary shear stress with the integrated momentum source. In equilibrium flow conditions the integrated boundary shear stress should match the integrated momentum source; (2) The numerical procedure is exposed by making a hand calculation. The description of the turbulent viscosity appears to be extremely important regarding the performance of the boundary methods. Consequently, (3) the performance of the turbulent viscosity profile will be tested. The by the model obtained turbulent viscosities are compared with what is expected from Mixing Length Theory. This requires a calculation without strong secondary currents. Therefore, for this test, additionally to the curved calculations a calculation of a straight river reach is made. To assess the effect of the grid spacing, (4) a small convergence analysis is carried out.

4.4 Hardware

The calculations are made a calculation cluster with four *Dual Core AMD Opteron 265* processors. Computing on different processors requires parallelization of the software. Table 5 shows the time it took the nodes to make the calculations. A significant decrease in simulation time can be obtained by renewing the equipment.

4.5 Summary

The described cases (with different outer-bank roughness and inclination and with/without a transverse bed slope) are calculated on a multiple processor calculation cluster (hardware) using a Large Eddy Simulator (software). The software is developing and is tested to assess its performance.

Direction	# Grid Points	Grid Spacing
Transverse (n)	292	0.0045 m
Longitudinal (s)	292	0.0028-0.0062 m
Vertical (z)	36	0.0044 m

Table 3: Computational grid used for the numerical model. Note that because the grid is curved the longitudinal grid spacing varies laterally.

	Simulated Time [s]	# Time Steps	Time Spacing [s]	# Through Flow
N16_30_00	284	200000	0.0014	86
N16_30_02	283	200000	0.0014	82
N16_30_30	282	200000	0.0014	74
N16_45_00	289	200000	0.0014	79
N16_45_02	288	200000	0.0014	77
N16_45_30	287	200000	0.0014	70
N16_30_02TBS	340	200000	0.0017	115

Table 4: Showing the simulated time, number of time steps, time spacing and number of times a fluid particle passes through the model domain. Where the latter one is calculated by dividing the product of the bulk velocity and the simulated time by the longitudinal length of the domain.

	Simulation Time
N16_30_00	5d 14h 17m
N16_30_02	5d 16h 12m
N16_30_30	5d 07h 05m
N16_45_00	5d 10h 49m
N16_45_02	5d 11h 25m
N16_45_30	5d 12h 04m
N16_30_02TBS	6d 23h 56m

Table 5: Showing the time (in days, hours and minutes) it took the nodes with four *Dual Core AMD Opteron 265* processors to make the calculations.

5 Results

In this chapter the plain results are presented, whereas in the next chapter the research questions are discussed. In the Theoretical Background (Chapter 3) three important internal flow quantities are recognized, *velocity*, *turbulence* and *boundary shear stress*. What information about these quantities can be obtained from the numerical data and the hand calculation?

5.1 Flow Velocity

The first column of Table 6 shows the bulk velocity (mean streamwise velocity) for each numerical calculation. As a result of the implemented forcing term, the bulk velocity is different for each calculation.

Remark The bulk velocity depends on the balance between the term forcing the flow and the boundary shear stress. In the algorithm, the magnitude of the forcing term is based on a desired bulk velocity and a friction coefficient (Section 4.2.3). In all calculations the desired bulk velocity is chosen to be 0.43 m/s and the friction coefficient to be 0.0035. For the broad variety of calculation the latter leaded to different bulk velocities. Equal bulk velocities could be obtained by choosing the friction coefficient wiser. This is possible by integrating the forcing term and dividing it by the length of the boundary.

Figure 11 shows the velocity field for all three directions. The velocities are normalized by the bulk velocity. The figure shows that streamwise velocity is concentrated in the outer bend. Which suggest a strong dominance of the secondary circulation over the potential vortex distribution. Moreover, the streamwise velocity field shows that near the inner bend the maximum velocities are located low in the water column. This also suggest a strong effect of the secondary circulations. Figure 12 shows the same graphs as Figure 11, but for the experimental data of `Duarte [2008]`.

5.1.1 Secondary Circulation

Based on the transverse and vertical velocity field (Figure 11), a few statements about the secondary circulation pattern can be made. (1) Firstly, the positive lateral velocities in the upper water column, negative lateral velocities in the lower water column, positive vertical velocities in the inner bend and negative vertical velocities in the outer bend indicate the classical helical motion or center region cell (by the stream function defined as a positive circulation). The axis of rotation is located quite low in the water column. (2) Close to the banks (at lateral coordinates 0.15 and 1.00) the strong positive circulation is opposed by forces enhancing negative circulation and locally negative vertical velocities are found in the inner bend and locally positive vertical velocities in the outer bend. Especially in the inner bend, the isolines of the normalized lateral velocity show the presence of a opposing negative circulation cell. (3) On the other hand, between the bank and the negative circulation (at the lateral coordinates 0.05 and 1.10), again a positive circulation cell exists, which is along the bottom connected with the center region cell.

The strength of the secondary circulation cell is quantified by means of the normalized stream function, ϕ (Equation 21, Table 7 and Figure 13).

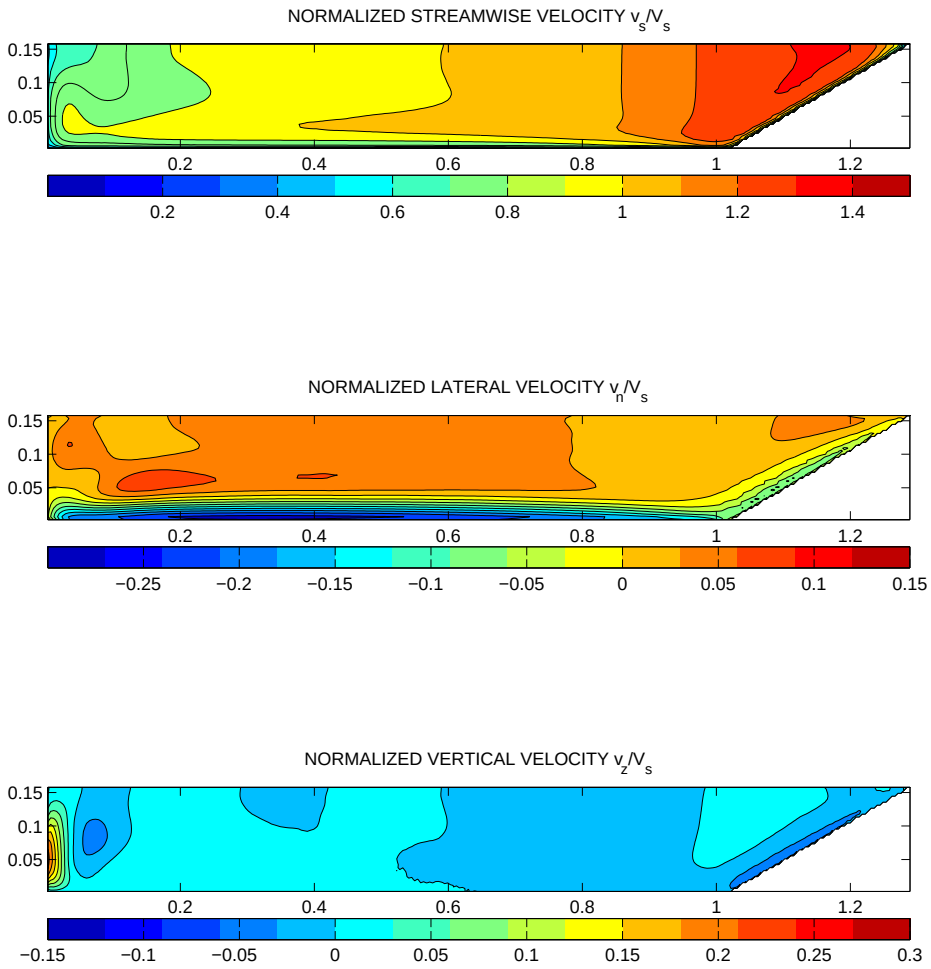

Figure 11: Cross section, showing the normalized streamwise, lateral and vertical velocity field for Calculation N16_30_02.

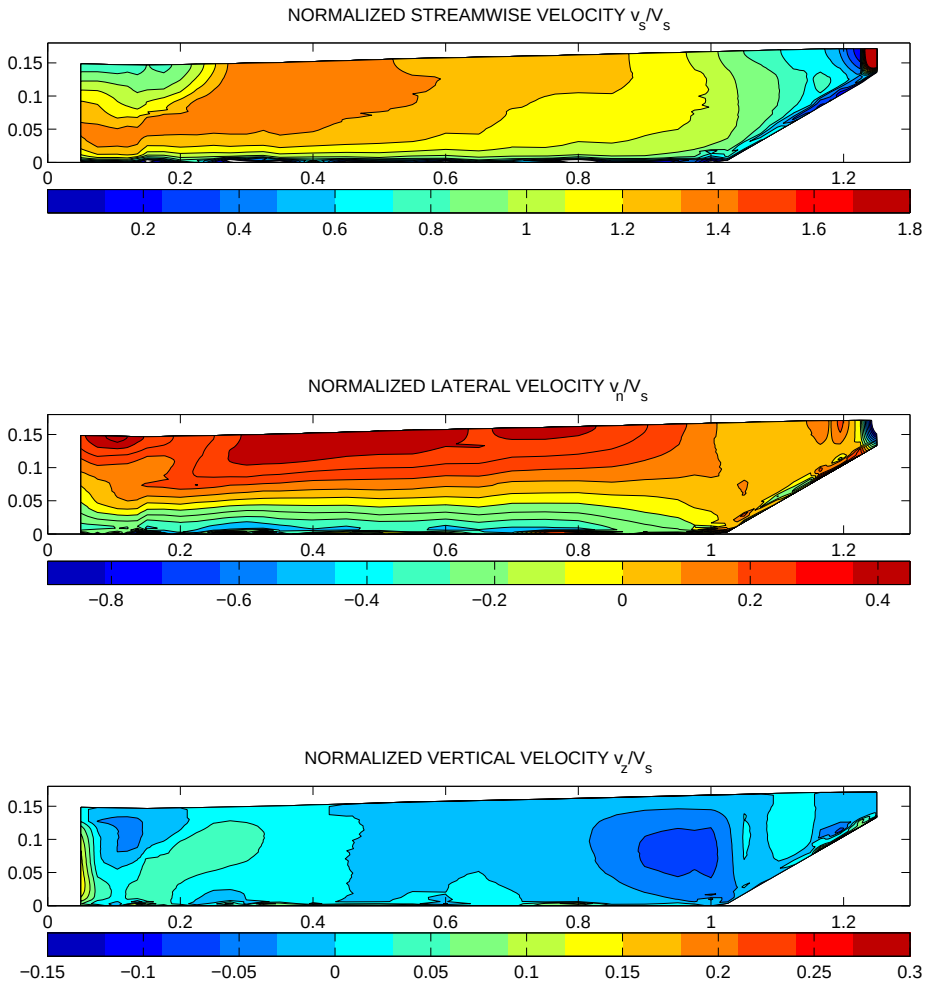

Figure 12: Cross section, showing the normalized streamwise, lateral and vertical velocity field for Physical Experiment F16_30_02 (`Duarte [2008]`). This data is still unpublished. Therefore, **before publishing one should consult K. Blanckaert**. Note that, in comparison with Figure 11, (1) the streamwise velocity is more concentrated near the inner bank and (2) the secondary velocities are significantly larger (Section 6.1.2).

$$\begin{aligned}\phi &= \frac{1}{hRV_s}\int (R+n)v_z \mathrm{dn} \\ &= \frac{(R+n)}{hRV_s}\int -v_n \mathrm{dz}\end{aligned} \tag{21}$$

where V_s is the longitudinal bulk velocity; h the mean water depth; R the radius of curvature; n the transverse location (here: defined zero at the channel axis); and the magnitude of the stream function can be obtained by integration. Figure 13 shows a strong positive circulation cell. The two depressions in the upper part of the water column at lateral coordinates 0.15 and 1 suggest opposing mechanisms enhancing a negative circulation. Figure 14 shows the same graphs as Figure 13, but for the experimental data of `Duarte [2008]`.

The meachnisms behind the secondary circulation can be assessed by the normalized vorticity equation/field. Equation 8 shows the streamwise vorticity balance. Neglecting the turbulence related centrifugal term, vorticity is added to the system by the terms representing the circulations of Prandtl's first and second type. Figure 15 shows the normalized vorticity and the normalized vorticity source terms of Prandtl's first and second type. The part that represents the circulation of Prandtl's first type can be transformed into Equation 22 (`Blanckaert and De Vriend [2004]`).

$$\begin{aligned}\frac{\partial \omega_{s,PRANDTL1}}{\partial t} &= -\frac{1}{1+n/R}\frac{\partial}{\partial z}\left(\frac{v_s^2}{R}\right) + \frac{1}{1+n/R}\frac{v_n\omega_s}{R} \\ &\quad + \frac{1}{1+n/R}\frac{\partial v_n}{\partial s}\frac{\partial v_s}{\partial z} - \frac{\partial v_z}{\partial s}\frac{\partial}{\partial n}\left(\frac{1}{1+n/R}v_s\right) \\ &\approx -\frac{1}{1+n/R}\frac{\partial}{\partial z}\left(\frac{v_s^2}{R}\right)\end{aligned} \tag{22}$$

where the first term in the equation represents the vorticity coinciding with the centrifugal force (`Duarte [2008]`). Neglecting all the terms with transverse and vertical velocity components (since $v_n, v_z << v_s$), leaves us with the first term. The part that represents the circulation of Prandtl's second type can be split in a part due to inhomogeneity of the turbulent shear stresses, $\overline{v_n' v_z'}$, and due to turbulence anisotropy, $\overline{v_n'^2} - \overline{v_z'^2}$ (Equation 23).

$$\begin{aligned}\frac{\partial \omega_{s,PRANDTL2}}{\partial t} &= \underbrace{\frac{\partial^2}{\partial z \partial n}\left(\overline{v_n'^2} - \overline{v_z'^2}\right) + \frac{1}{1+n/R}\frac{1}{R}\frac{\partial \overline{v_n'^2}}{\partial z}}_{Due\ to\ Anisotropy} \\ &\quad + \underbrace{\left(\frac{1}{1+n/R}\frac{\partial^2}{\partial z^2} - \frac{\partial}{\partial n}\left(\frac{1}{1+n/R}\frac{\partial}{\partial n}\right)\right)\left((1+n/R)\,\overline{v_n' v_z'}\right)}_{Due\ to\ Inhomogeneity}\end{aligned} \tag{23}$$

The mainly negative values of the vorticity in Figures 15 and 16 show the dominance of the, with the center region cell corresponding, clockwise rotation. Though, different locations with positive vorticity can be distinguished at the transverse coordinates 0.15, 0.45, 1.00 and 1.20 (Figure 17). The positive locations at transverse locations 1.00 and 1.20, are mainly enhanced by the voritcity source of Prandtl's second type and can be tied to the outer-bank cell (Chapter 3). The cell at transverse location 1.00 is detached from the outer-bank by a clockwise rotation cell.

	V_s [m/s]	u_* [m/s]	C_f [-]
N16_30_00	0.3939	0.0266 (0.0240)	0.0046 (0.0037)
N16_30_02	0.3756	0.0282 (0.0240)	0.0056 (0.0041)
N16_30_30	0.3413	0.0302 (0.0240)	0.0078 (0.0050)
N16_45_00	0.3587	0.0240 (0.0237)	0.0045 (0.0044)
N16_45_02	0.3456	0.0242 (0.0237)	0.0049 (0.0047)
N16_45_30	0.3189	0.0255 (0.0237)	0.0064 (0.0055)
N16_30_02TBS	0.4386	0.0332 (0.0247)	0.0057 (0.0032)

Table 6: The streamwise bulk velocity, V_s, the root mean square of the friction velocity, u_*, and the friction coefficient, C_f. For the friction velocity and friction coefficient, two values are given. This because of two different ways to calculate the friction velocity. For the first value, the friction velocity is based on the mean of the boundary shear stresses, while for the second value (the value between brackets) the friction velocity is based on the term forcing the flow. Both values should, however, be identical.

	ϕ [-]	$s(\phi_{max})$ [m]	$z(\phi_{max})$ [-]
N16_30_00	1548	0.5009	0.0378
N16_30_02	1713	0.5231	0.0378
N16_30_30	2372	0.6745	0.0422
N16_45_00	1921	0.5721	0.0422
N16_45_02	2154	0.6478	0.0422
N16_45_30	3005	0.7858	0.0511
N16_30_02TBS	1606	0.7769	0.0464

Table 7: The magnitude- and location of the maximum Stream Function.

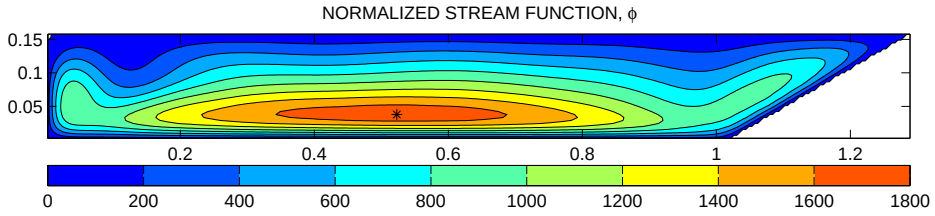

Figure 13: Cross section, showing the isolines of the normalized stream function for Calculation N16_30_02. A positive circulation cell can be noticed with the maximum value of the stream function (*) indicating the axis of rotation of the circulation cell. The two depressions in the upper part of the water column at lateral coordinates 0.15 and 1 suggesting opposing mechanisms enhancing a negative circulation.

5.2 Boundary Shear Stress

Table 8 shows the total boundary shear force in the system. In the first column the total boundary shear force is calculated by integrating the driving force (or momentum source), which given that the flow is in equilibrium coincides with the actual momentum 'loss'. In the second column the total boundary shear force is calculated by integrating the boundary shear stress. For the boundary shear force calculated via integration of the boundary shear stress, two values are given. The value between brackets is obtained by integrating the boundary shear stress over the width and length of the grid cells. The first value, without brackets, is obtained by integrating the boundary shear stress over the real surface of the boundary.

Table 9 shows the results of the convergence analysis. For a coarser grid, the from the velocity field obtained boundary shear force is closer to the from the momentum source obtained 'actual' boundary shear force.

Figures 19 and 20 show the boundary shear stress profile along the perimeter. The boundary shear stress is relatively small at the smooth inner bank and relative large at/near the outer-bank where flow velocities large. The differences between the different calculations is quantified in Table 10 and discussed in Chapter 6. Regarding the distribution of the bank shear stress `Ottevanger [2013]` found for a large width to radius of curvature ratio (b/R) the magnitude of the bank shear stress at the upper and lower bend are similar (Figure 18). Knowing that the b/R is 1.3/1.7=0.76, Figure 19 and 20 reinforce the latter.

The hand calculation provides information about the behavior of the boundary method. This hypothetical calculation considers a boundary where, for equilibrium conditions, the u_* should be 0.02 m/s. In this numerical algorithm the first grid point is located at 0.002 m and the second at 0.006 m from the boundary. For the considered boundary, the rough wall function is applicable, while z_0 is 0.0005. Hence, the velocities in the first and second grid point can be calculated. The associated viscosity (turbulent plus molecular) can also be calculated according to Equation 24. In this case using the Normal Wall Function Approach or the Immersed Boundary Method will lead to an identical result.

$$\nu = u_*^2 / \left(\frac{u_2 - u_1}{\Delta z} \right) \tag{24}$$

However, assuming that the model underestimates the near wall viscosity with 10%. Hence, to ensure sufficient momentum transfer towards the boundary, in case of the Normal Wall Function Approach, the velocity in grid point 2 increases according to Equation 25 while the velocity in grid point 1 remains unchanged (third column in Table 11).

$$u_2 = \frac{u_*^2}{(\nu - \Delta\nu)} \Delta z + u_1 \tag{25}$$

To ensure sufficient momentum transfer towards the boundary, in case of the Immersed Boundary Method, both the velocity in grid points 1 and 2 increase according to equation 26. This requires a larger velocity increase compared to the Normal Wall Function Approach (Figure 21 and the fourth column in Table 11).

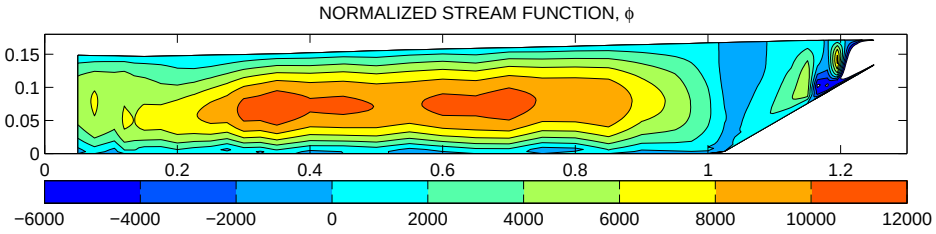

Figure 14: Cross section, showing the isolines of the normalized stream function for Physical Experiment F16_30_02. This data is still unpublished. Therefore, **before publishing one should consult K. Blanckaert**. Note that, in comparison with Figure 13, (1) also a positive circulation is present in the core of the flow, (2) the magnitude of the stream function is significantly larger, (3) the maximum value of the stream function is located further from the bed and (4) the two depressions at lateral coordinates 0.15 and 1 suggesting opposing mechanisms enhancing a negative circulation are, though different in magnitude, also present (Section 6.1.2). Since the secondary velocities in this cross-section are not divergence free, the depth-averaged net water transport had to be subtracted before calculating the stream function.

F =	$\int$ Momentum Source [N];	$\int$ Boundary Shear Stress [N]
N16_30_00	1.0466	1.3450 (1.2921)
N16_30_02	1.0466	1.5096 (1.4282)
N16_30_30	1.0466	1.7348 (1.6050)
N16_45_00	1.0982	1.1296 (1.0794)
N16_45_02	1.0982	1.1458 (1.0726)
N16_45_30	1.0982	1.2784 (1.1265)
N16_30_02TBS	1.0983	1.9872 (1.8731)

Table 8: The total boundary shear force in the system, calculated by integration of the driving force (momentum source) and by integration of the boundary shear stress. The boundary shear stress can be integrated by multiplying the boundary shear stress by the width and length of the grid cells (value between brackets) and by the real surface of the implemented immersed boundary.

F =	$\int$ Momentum Source [N];	$\int$ Boundary Shear Stress [N]	Δn
	1.0466	1.5096 (1.4282)	0.0045
	1.0970	1.2665 (1.2134)	0.0098
	1.0869	1.2102 (1.1634)	0.0135

Table 9: Table similar to Table 8 but showing the results of the convergence analysis. Calculation N16_30_02 is carried out with three different grid sizes. The total boundary shear force in the system, calculated by integration of the driving force (momentum source) and by integration of the boundary shear stress. The boundary shear stress can be integrated by multiplying the boundary shear stress by the width and length of the grid cells (value between brackets) and by the real surface of the implemented immersed boundary. In the last column the grid spacing is given.

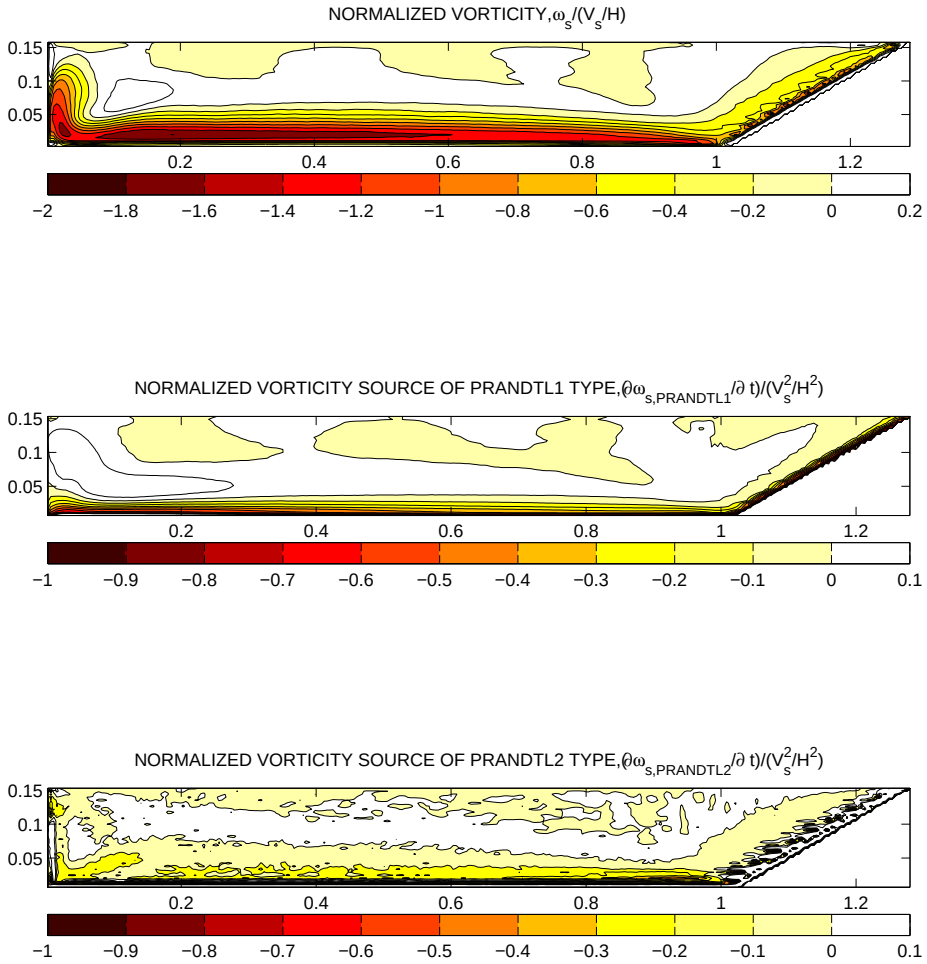

Figure 15: Cross section, showing the normalized vorticity as well as the normalized vorticity source of Prandtl's first and second type for Calculation N16_30_02. The graphs only show the negative values, all positive values are assigned white, which according to the author leaded to the most clear visualization of the vorticity field.

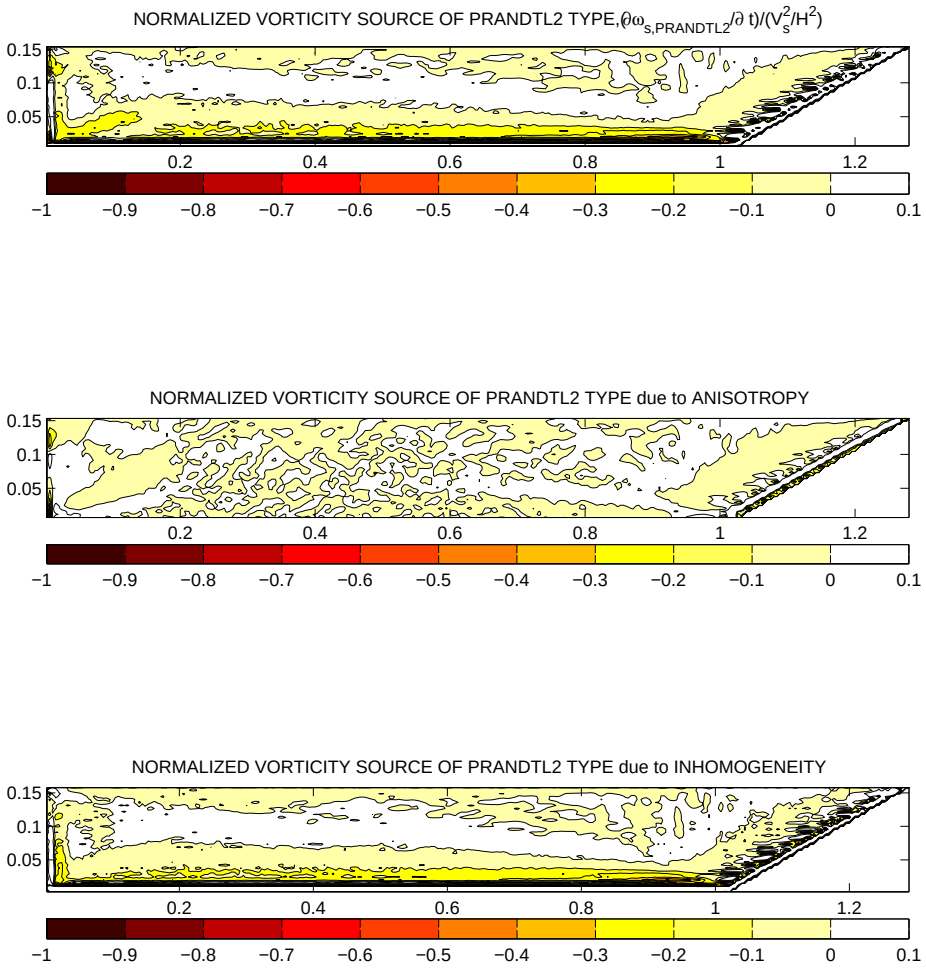

Figure 16: Cross section, showing the normalized vorticity source of Prandtl's second type as well as the part due to anisotropy and inhomogeneity for Calculation N16_30_02. The graphs only show the negative values, all positive values are assigned white, which according to the author leaded to the most clear visualization of the vorticity field.

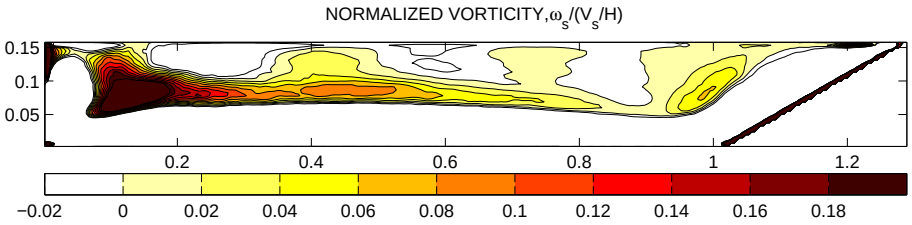

Figure 17: Cross section, showing the normalized vorticity for Calculation N16_30_02. The graphs is identical to Figure 15a, but in contrary only shows the positive values, all negative values are assigned white. Note the order of magnitude of the scale is one order smaller than in Figure 15.

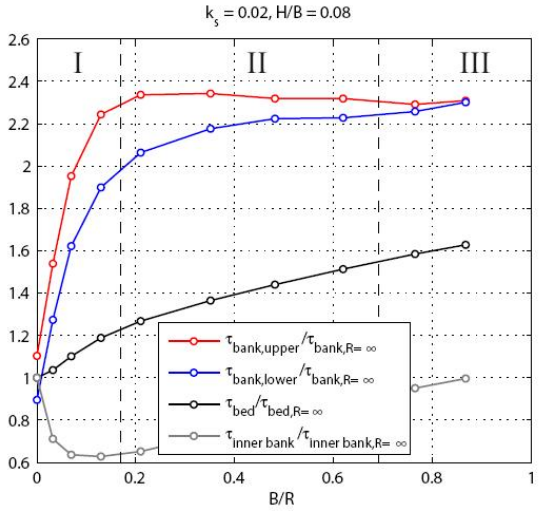

Figure 18: Results of `Ottevanger [2013]` show that for a large b/R there is hardly any difference between the upper and lower bank shear stress.

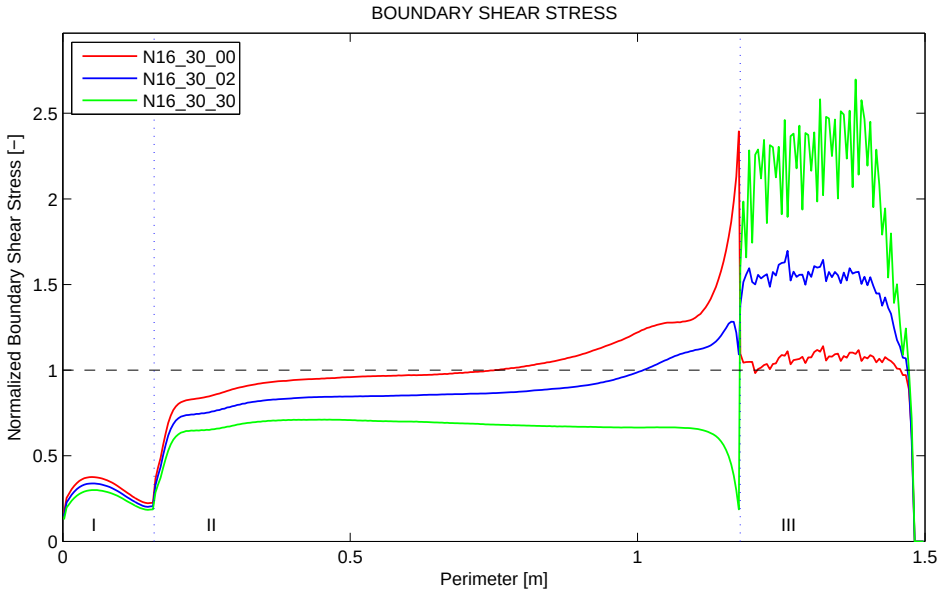

Figure 19: The boundary shear stress along the perimeter, normalized by the average boundary shear stress, for the calculations with a 30° outer-bank angle. (I) denotes the smooth inner bank; (II) the bed and; (III) the inclined outer-bank. The variations in the outer-bank shear stress are due to the Immersed Boundary Method and are explained in Section 6.4

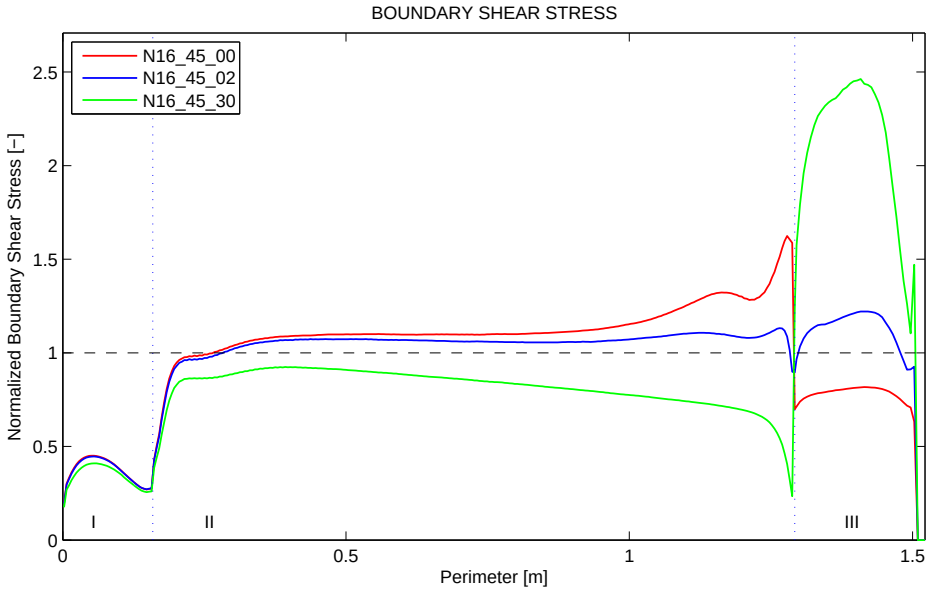

Figure 20: The boundary shear stress along the perimeter, normalized by the average boundary shear stress, for the calculations with a 45° outer-bank angle. (I) denotes the smooth inner bank; (II) the bed and; (III) the inclined outer-bank.

$$
\begin{aligned}
u_2 &= \frac{u_*^2}{(\nu - \Delta\nu)} \Delta z / \left(1 - \frac{log(z_1/z_0)}{log(z_2/z_0)}\right) \\
u_1 &= u_2 \left(\frac{log(z_1/z_0)}{log(z_2/z_0)}\right)
\end{aligned}
\tag{26}
$$

For the Immersed Boundary Method, the with the velocity profile coinciding shear velocity, $u_{*,output}$, is now larger than the with the momentum flux, thus also with the actual shear stress, coinciding shear velocity, $u_{*,actual}$. Since the boundary shear stress is proportional to the square of the friction velocity, a 10% underestimation of the near wall viscosity will lead to about 25% overestimation of the boundary shear stress whereas a 30% underestimation of the near wall viscosity will lead to 100% overestimation.

5.3 Turbulence

Figure 16 showed already the effect of the inhomogeneity of the turbulent shear stresses and the turbulence anisotropy on the secondary circulations. Figure 22 shows the inhomogeneity and anisotropy as well as the turbulent kinetic energy. The anisotropy is as expected positive at the horizontal bed and 30° outer-bank and negative at the vertical inner bank. The turbulent kinetic energy is a measure for the turbulent activity. The graph shows a lot of activity near the boundary and in the 90° angle between the bed and the inner bank.

5.3.1 Turbulent Viscosity

The contribution of the turbulence consists of a resolved part and a sub-grid part. Figure 23 shows the resolved and sub-grid turbulent viscosity profile in the central part of the straight channel, where effects of the side wall are assumed to be negligible (Calculation N16_90_02). The results show that in the ghost cell the part of the turbulence that is resolved is negligible and that the turbulent viscosity in the second grid point is slightly smaller than the value expected from boundary layer theory, κy^+ (Appendix B). The viscosity profile resembles a profile as expected according to mixing length theory.

Remark The critical reader might have noticed that the maximum z^+ is only 1300 (whereas it is almost 3000 for the in Chapter 4 described calculations) and that using also periodic boundary conditions in lateral direction would make more sense. The latter implies an infinitely wide channel, where absolutely no wall effect are present. The author recognizes this problems and for this calculation more care should have been taken choosing the input parameters, but because of time considerations there is satisfied with the current check.

	P_{OB}/P	$\overline{\tau}_{OB}/\tau_0$	$\tau_{OB,max}/\tau_0$
N16_30_00	0.2118	1.0062	1.1399
N16_30_02	0.2118	1.3788	1.6970
N16_30_30	0.2118	1.9135	2.6976
N16_45_00	0.1475	0.7161	0.8169
N16_45_02	0.1475	1.0300	1.2211
N16_45_30	0.1475	1.9161	2.4626
N16_30_02TBS	0.2118	1.3957	1.7144

Table 10: The relative length of the outer-bank and normalized mean and maximum outer-bank shear stress. Where $\tau_{OB,max}$ is defined as the average in time maximum in space value and τ_{OB} as the average in time and space.

		Normal method	IBM
	No error in ν_t	Small error in ν_t	Small error in ν_t
ν [m^2/s]	$2.913{\cdot}10^{-}5$	$2.622{\cdot}10^{-}5$	$2.622{\cdot}10^{-}5$
u_1 [m/s]	$0.693{\cdot}10^{-}1$	$0.693{\cdot}10^{-}1$	$0.770{\cdot}10^{-}1$
u_2 [m/s]	$1.242{\cdot}10^{-}1$	$1.303{\cdot}10^{-}1$	$1.381{\cdot}10^{-}1$
$u_{*,actual}$	$2.000{\cdot}10^{-}2$	$2.000{\cdot}10^{-}2$	$2.000{\cdot}10^{-}2$
$u_{*,output}$	$2.000{\cdot}10^{-}2$	$2.000{\cdot}10^{-}2$	$2.220{\cdot}10^{-}2$

Table 11: Results from hand calculation, showing the obtained velocities using the Normal Wall Function Approach and the Immersed Boundary Method for a correct and an underestimated turbulent viscosity.

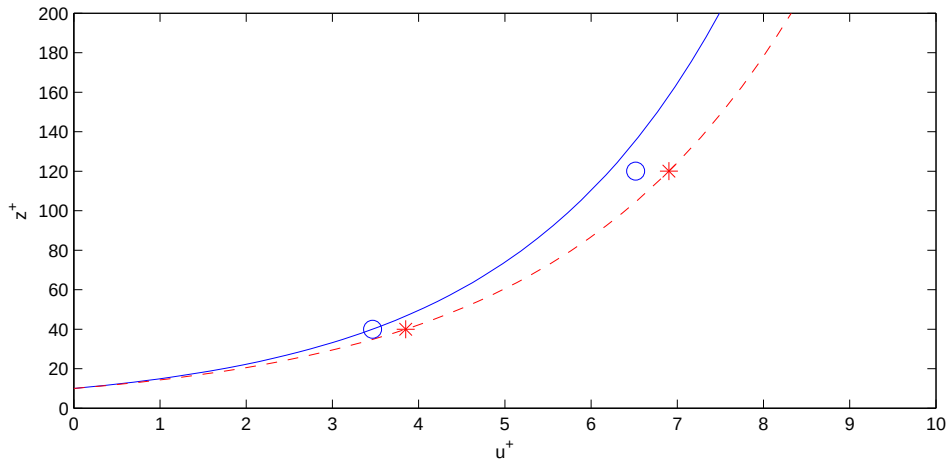

Figure 21: Results from the hand calculation, where the blue continuous line shows the correct logarithmic wall function; the blue rounds the obtained velocity in the first and second velocity grid point, using the Normal Wall Function Approach and given a 10% underestimation of the turbulent viscosity; and the red stars the obtained velocity in the first and second velocity grid point, using the Immersed Boundary Method and given a 10% underestimation of the turbulent viscosity. The red stars appear to lie neatly on a logarithmic curve (red striped line), which is unfortunately not the logarithmic curve coinciding with the actual boundary shear stress (blue continuous line)

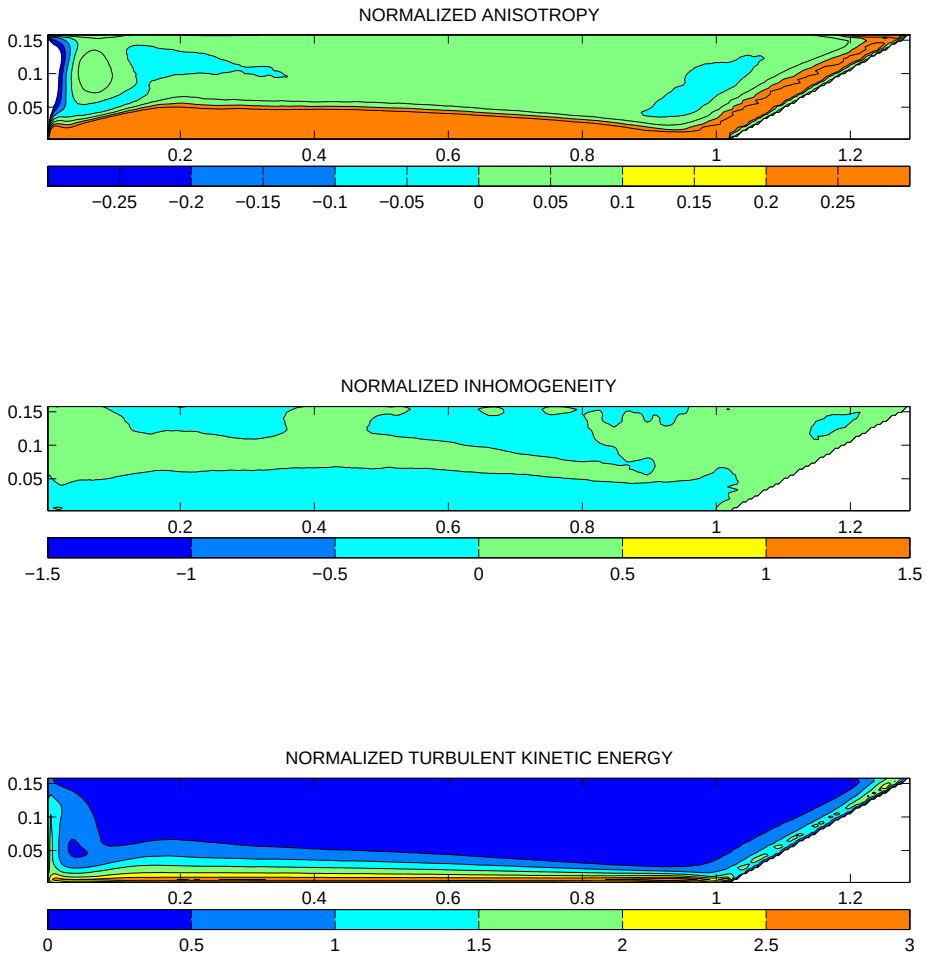

Figure 22: Turbulent properties normalized by the squared friction velocity for Calculation N16_30_02.

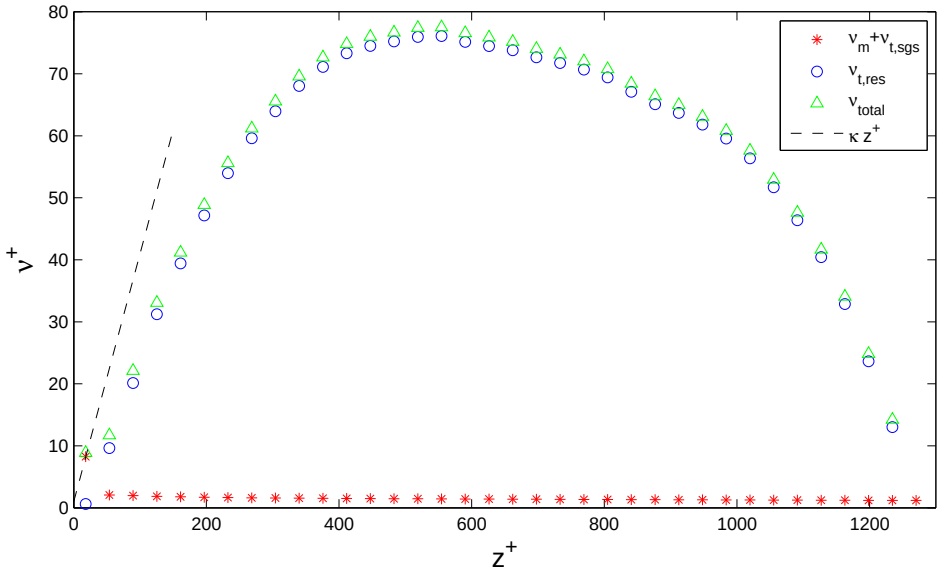

Figure 23: The viscosity profile in the central part (around the channel axis) of Calculation N16_90_02STR (a straight reach). The red stars represent the sub-grid viscosity, molecular plus turbulent; the blue circles, the resolved turbulence written in units of 'viscosity'; the blue triangles, the total viscosity, which is the sum of the latter; and the striped black line the function κz^+, which is the viscosity profile close to the wall that is expected according to boundary layer theory.

6 Discussion

This chapter discusses the research questions.

6.1 Outer-Bank Roughness

How are the magnitude and distribution of the outer-bank shear stress affected by the roughness of the outer-bank?

6.1.1 Comparing Calculations N16_30_00, N16_30_02 and N16_30_30.

Comparing the calculations: (1) Table 6 shows that for a rougher outer-bank a lower average streamwise velocity is obtained. Given an equal forcing term, this implies a larger friction coefficient. (2) The streamwise velocity distributions show a similar pattern (Figure 24). High velocities are located near the outer-bank, while near the inner-bank the highest velocities are located near the bed. Difference between the calculations is though that for a rough outer-bank the flow is less concentrated near the outer-bank. (3) Figure 25 shows that the secondary circulation pattern is similar. Though, for a rough outer-bank the (central region) secondary circulation is stronger, while the axis of rotation of the main circulation cell shifts upwards and towards the outer-bank. (4) Figure 26 shows that the outer-bank cell at transverse coordinate 1.20 strengthens for a rougher outer-bank, while the cell at transverse coordinate 1.00 weakens significantly. The latter might correspond with the outward shift of the central region cell. (5) Table 10 and Figure 19, show a larger normalized bank shear stress for a rough outer-bank. (6) Regarding the distribution of the outer-bank shear stress, Figure 19 shows that for a rougher outer-bank the distribution is less uniform. The bank shear stress increases slowly from the bank toe towards a certain point before decreasing rapidly towards zero at the water surface. This corresponds with the increased strength of the outer-bank cell at transverse loacation 1.20.

6.1.2 Comparison with Duarte [2008]

Main deviation with the flume experiments of `Duarte [2008]` (where this numerical calculations are based on) is the location of the maximum flow velocities. In the flume experiments the maximum flow was located near the inner bend, as a result of potential vortex distribution (Figure 12). The results are based on the cross section at 90° from the bend entrance in a developing flow case. The numerical calculations in the present paper are based on an axisymmetric flow case, in other words developed flow. Figure 27 shows indeed that the maximum flow at 90° from the bend entrance is concentrated near the inner bend, but also that at 180° from the bend entrance the flow is more concentrated near the outer bend. Secondly, the secondary velocities in the flume experiments are much larger. The latter can be subscribed to the occurrence of net transport of water towards the outer-bank (known as meander currents). The non-uniformity of these meander currents result in a stronger secondary circulation (Figure 14). The flume experiments show that for an increasing outer-bank roughness the bank shear stress shear stress get less uniform, which suggest an increased effect of the secondary circulations. The mean and maximum outer-bank shear stress increase also with increasing outer-bank roughness. In contrary to the numerical results, the maximum of the outer-bank shear stress is located near the bank toe. The fact that the outer-bank cell in the flume experiments is much more present and larger in extend, means that the highest secondary velocities towards the outer-bank are located near the bank toe, which seems to explain the deviation in the outer-bank shear stress distribution.

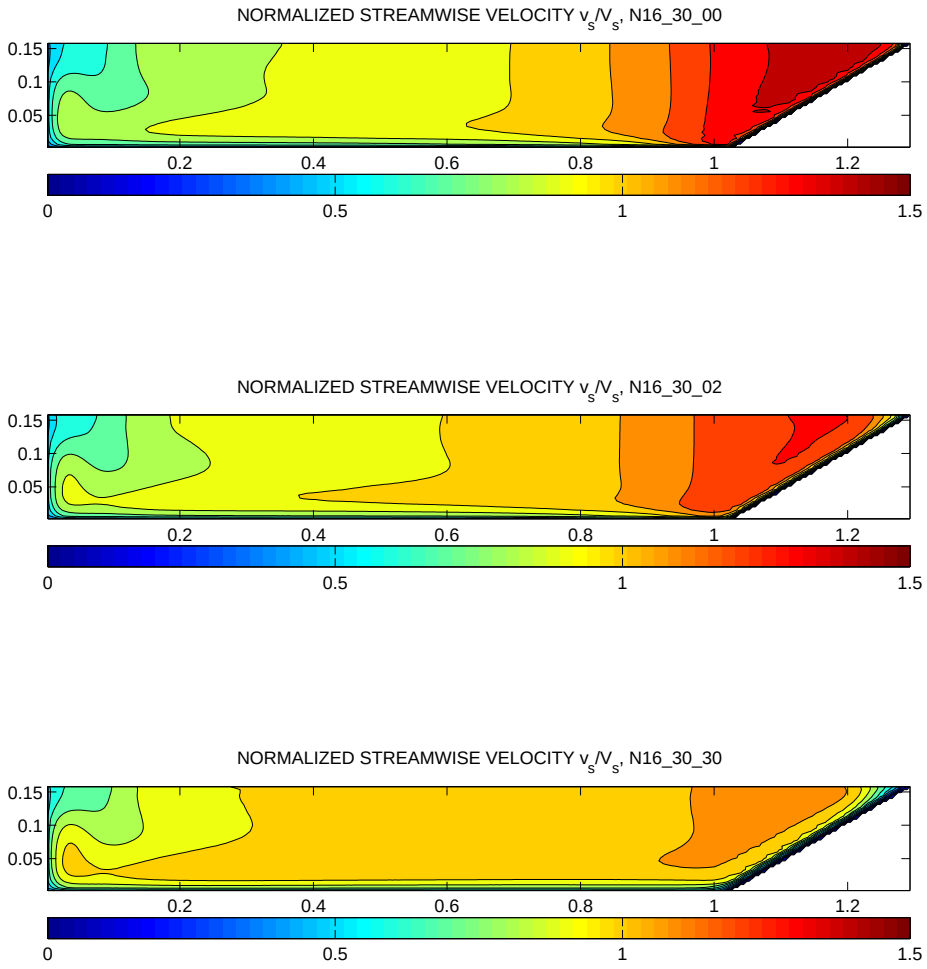

Figure 24: Cross section, showing the Normalized Streamwise Flow Velocity for Calculations N16_30_00, N16_30_02 and N16_30_30.

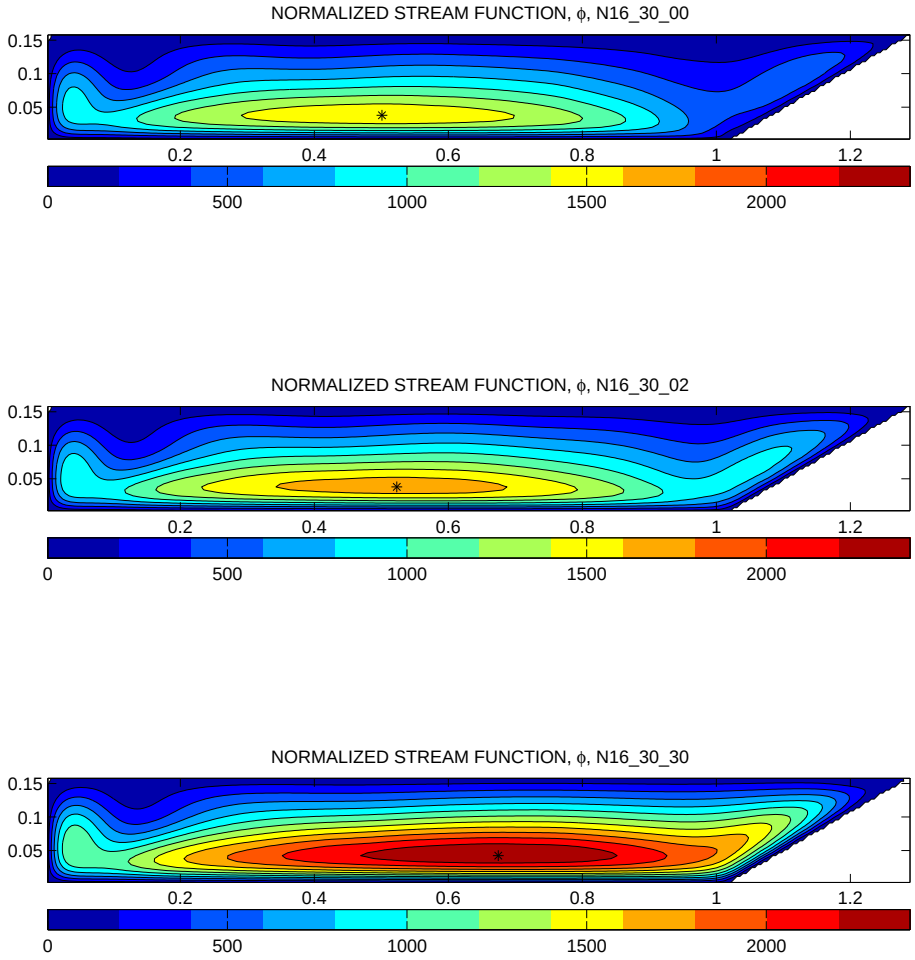

Figure 25: Cross section, showing the Normalized Stream Function for Calculations N16_30_00, N16_30_02 and N16_30_30.

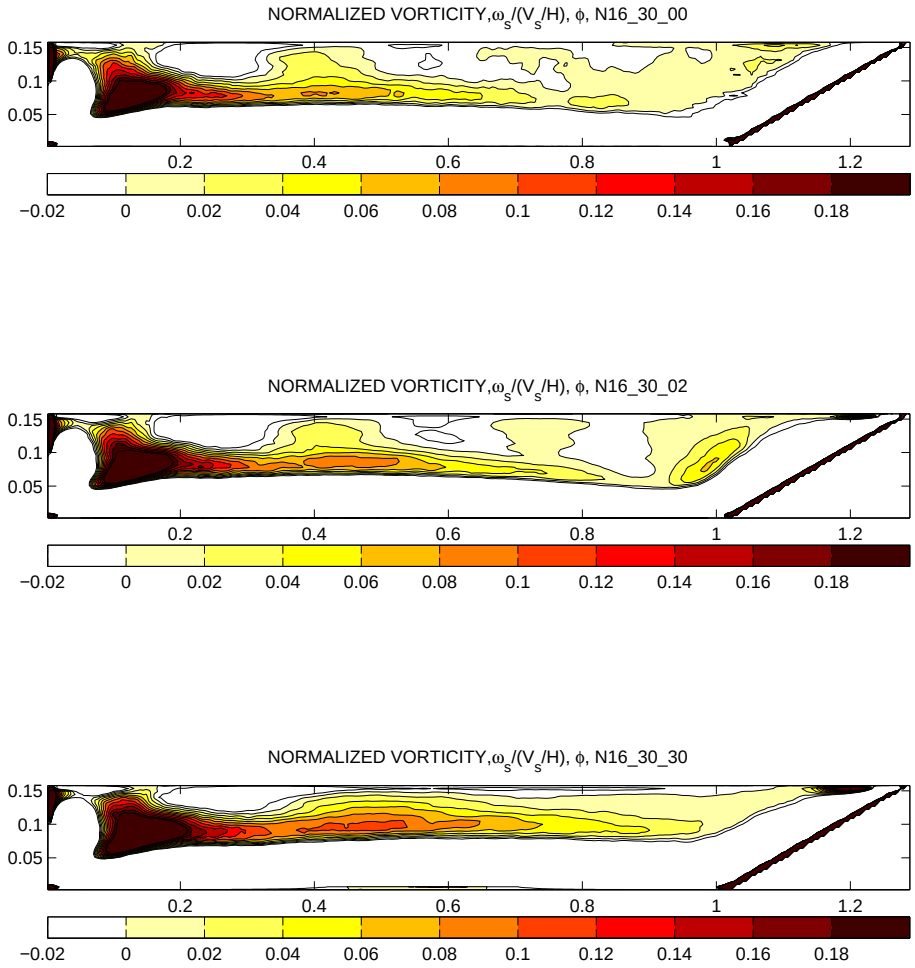

Figure 26: Cross section, showing the Normalized Vorticity for Calculations N16_30_00, N16_30_02 and N16_30_30. The graphs only shows the positive values, all negative values are assigned white.

6.2 Outer-Bank Inclination

How are the magnitude and distribution of the outer-bank shear stress affected by the inclination of the outer-bank?

6.2.1 Comparing Calculations N16_45_02 and N16_30_02.

Comparing the calculations: (1) The streamwise velocity distribution shows for the calculations a similar pattern (Figure 28) Though for a steeper outer-bank the flow is less concentrated near the outer-bank. (2) The vertical velocities at the outer-bank are larger for a steeper bank (Figure 29). (3) Figure 30 shows that the secondary circulation pattern is similar. Though, for a steeper outer-bank the (central region) secondary circulation is stronger, while the axis of rotation of the main circulation cell shifts upwards and towards the outer bend. (4) Figure 31 shows that the outer-bank cell at transverse coordinate 1.20 strengthens for a steeper outer-bank, while the cell at transverse coordinate 1.00 weakens significantly. The latter might correspond with the outward shift of the center region cell. (5) Figure 19 and 20 show a smaller normalized bank shear stress for a steeper outer-bank. (6) They also show that for a steeper bank angle the magnitude of the boundary shear stress is more sensitive to the outer-bank roughness, which can be argued intuitively. (7) Regarding the distribution of the outer-bank shear stress, Figure 19 and 20 show that for a steeper outer-bank the maximum outer-bank shear stress is located higher in the water column. This might correspond with the increased strength of the outer-bank cell.

6.2.2 Comparison with Duarte [2008]

In subsection 6.1.2 is discusssed why there is a difference between the numerical axisymmetric flow calculations and the physical developing flow measurements. Regarding the (distribution) of the outer-bank shear stress, the physical experiments did not show a big difference between different inclinations of the outer-bank. For both inclinations the distribution of the normalized outer-bank shear stress is more or less uniform with a magnitude of 0.5. In agreement, the numerical calculations give a more or less uniform distribution, but in contrary with a magnitude of 1. The difference can be subscribed to the location of the maximum flow velocities. The flow velocities are located near the inner bend in the developing flow measurements and near the outer bend for the axisymmetric calculations.

6.3 Transverse Bed Slope

How are the magnitude and distribution of the outer-bank shear stress affected by the, with the point bar related, transverse bed slope?

6.3.1 Comparing Calculations N16_30_02 and N16_30_02TBS.

Comparing the calculations: For the inner bend there is no doubt that the situation is completely different; For the outer bend Figures 28, 29, 30 and 31 show only minor differences between the flat and sloping bed. Although the calculation with the flat bed misses the effect of topographic steering. For the investigated width to curvature ratio, this suggests that the effect of the secondary circulations outscores the effect of topographic steering. Comparing Figures 19 and 32 shows that the bank shear stress is almost identical. In contrary the bed shear stress distribution is significantly different. Note that the stream function and vorticity are normalized by the mean water depth, which is smaller for the calculation with transverse bed slope.

With this research question, it is intended to further decrease the gap between the available bank shear stress data and bank shear stress in natural river bends. Therefore, it is yet impossible to compare the numerical outcomes with physical experiments or field data. Collecting information about the bank shear stress in flumes or rivers with a developed bathymetry might be subject to further research.

6.4 Performance of the Algorithm

How accurate is the algorithm in describing the boundary shear stress, what is the reason for the inaccuracy and how can the accuracy be improved?

In preliminary tests imperfections in the description of the velocity and viscosity in the ghost cell (grid cell neighboring the boundary) are recognized and solved by the author (Section 4.2). This considerably improved the performance of the model. Main problem was that the turbulent viscosity in the ghost cell was extremely underestimated. Results from the hand calculation, presented in Section 5.2, show that an underestimated turbulent viscosity leads to overestimated flow velocities. The with this flow velocity coinciding boundary shear stress is thus also an overestimation.

Table 8 shows the performance of the boundary method after these corrections. Based on integration of the momentum source, the first column shows the value that the boundary shear force should equal. The latter is possible since the flow is in equilibrium. For calculations N16_45_00 and N16_45_02 the values of the boundary shear force integrated from the boundary shear stress are quite accurate. Note that the boundary shear stress is obtained from the velocity gradients at the boundary. This good accuracy suggests that after the corrections the boundary method is quite good for the calculation of this two considered cases.

For the other calculations the accuracy is, however, less accurate (Table 8). Firstly, for rough boundaries the boundary method seems less accurate. For rough boundaries the local boundary shear stress and thus the local friction velocity is larger. This means that the distance from the boundary coinciding with $z^+ = 1$ is smaller (Equation 27). This means that the distance of the ghost cell to the boundary is larger in wall coordinates when the boundary is rough. Arguing that the boundary method is less accurate for higher z^+-values, might explain the decrease in accuracy.

$$z = \frac{z^+ \nu}{u_*} \tag{27}$$

Secondly, for the calculations with a 30° outer-bank angle the boundary method seems less accurate than for the calculations with a 45° outer-bank angle. Moreover, comparing Figures 19 and 20 it can be seen that in contrast to the 45° calculations for the 30° calculations the bank shear stress profile is not smooth. This observation can be explained. Known is that the aspect ratio between the vertical and lateral grid spacing is about unity. This means that when applying a 45° outer-bank angle, all the ghost cells have an equal distance to the boundary (Figure 33a). In contrary, when applying a 30° outer-bank angle, the ghost cells have different distances to the boundary (Figure 33b). The in space fluctuating bank shear stress in Figure 19 suggests that the performance of the boundary method depends on the grid spacing.

The hand calculation showed that the accuracy of the Immersed Boundary Method depends on the description of the turbulent viscosity. After the corrections the turbulent viscosity in the

ghost cell is properly described. However, besides the turbulent viscosity in the ghost cell, also the turbulent viscosity in the second velocity grid cell (or interpolated point I) should not be underestimated. The results from Table 8 suggest the latter. Since this second velocity grid point from the boundary is also close to the boundary, the assumption of homogeneity and isotropy is not valid. Therefore strictly the Smagorinsky Model is not valid and might underestimate the turbulent viscosity perpendicular to the boundary. Since the Smagorinsky Model is used to obtain the turbulent sub-grid viscosity in these grid cells, the inaccuracy of the boundary method can be assigned to the underestimation of the turbulent viscosity in the second velocity grid cell from the boundary. Results from calculation N16_90_02STR (Figure 23) show indeed that the turbulent viscosity in the second grid cell from the boundary is smaller than κz^+.

Above is suggested that the performance of the boundary method can be subscribed to the description of the turbulent viscosity and that the performance depends on the grid spacing. It is, however, not evident that a grid refinement would be an improvement. Because, it that case the second velocity grid point from the wall is located closer to the boundary, while closer to the boundary the assumption of homogeneity and isotropy are more violated. The latter leads to a further underestimation of the turbulent viscosity. The convergence analysis (Section 5.2) reinforces this theory.

Hence answering the research question. Concluded can be that the boundary method is in some cases quite accurate and quantified in Table 8. The present inaccuracy can be subscribed to the underestimation of the turbulent viscosity in the second grid cell from the boundary. The distance from the grid cells to the boundary influences the inaccuracy. The accuracy can be further improved by reconsidering the implemented Smagorinsky Model. Different improved Smagorinsky Models are developed. `Lévêque et. al. [2006]` developed an improved Smagorinsky Model, which is presumed performing good in complex non-homogeneous turbulent flows.

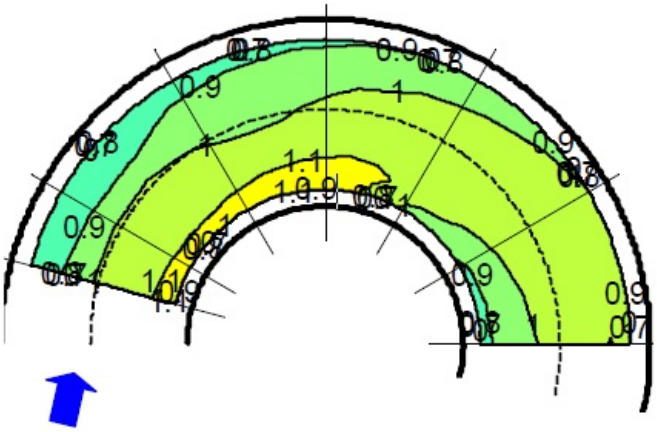

Figure 27: Depth Averaged Streamwise Velocity divided by the Cross Sectional Averaged Velocity for Measurement F16_90_02 (`Duarte [2008]`).

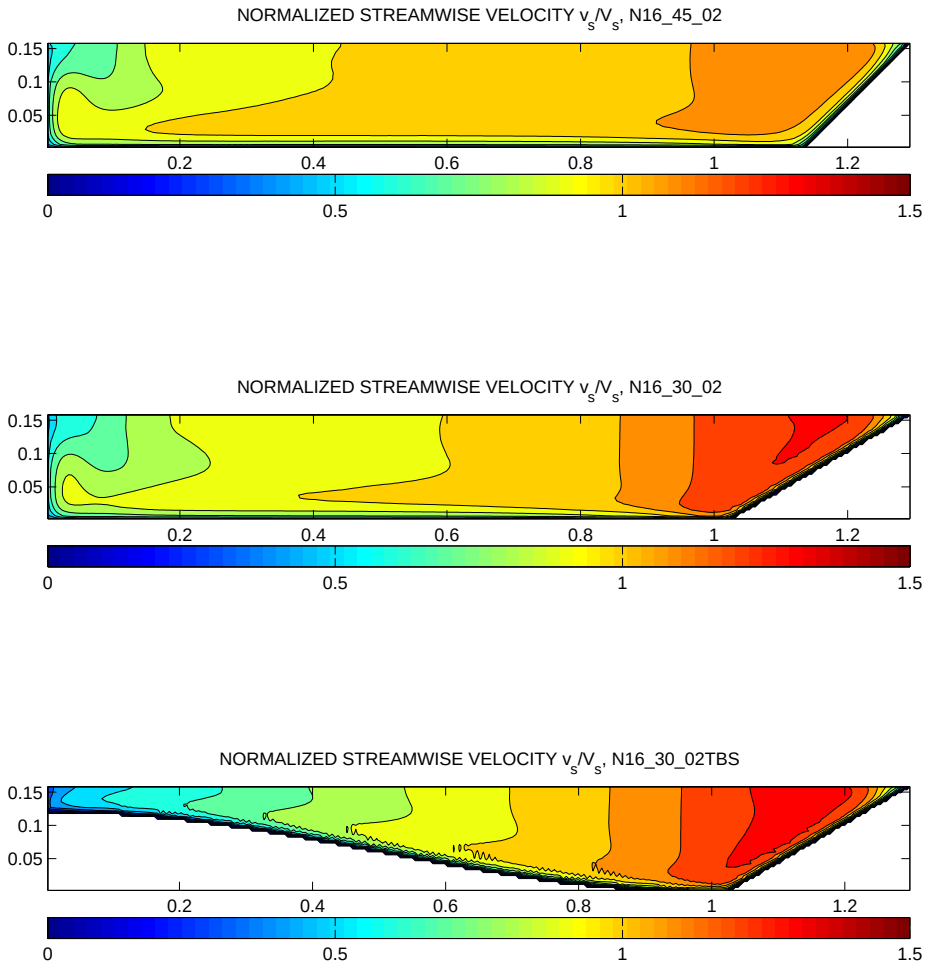

Figure 28: Cross section, showing the Normalized Streamwise Flow Velocity for Calculations N16_45_02, N16_30_02 and N16_30_02TBS.

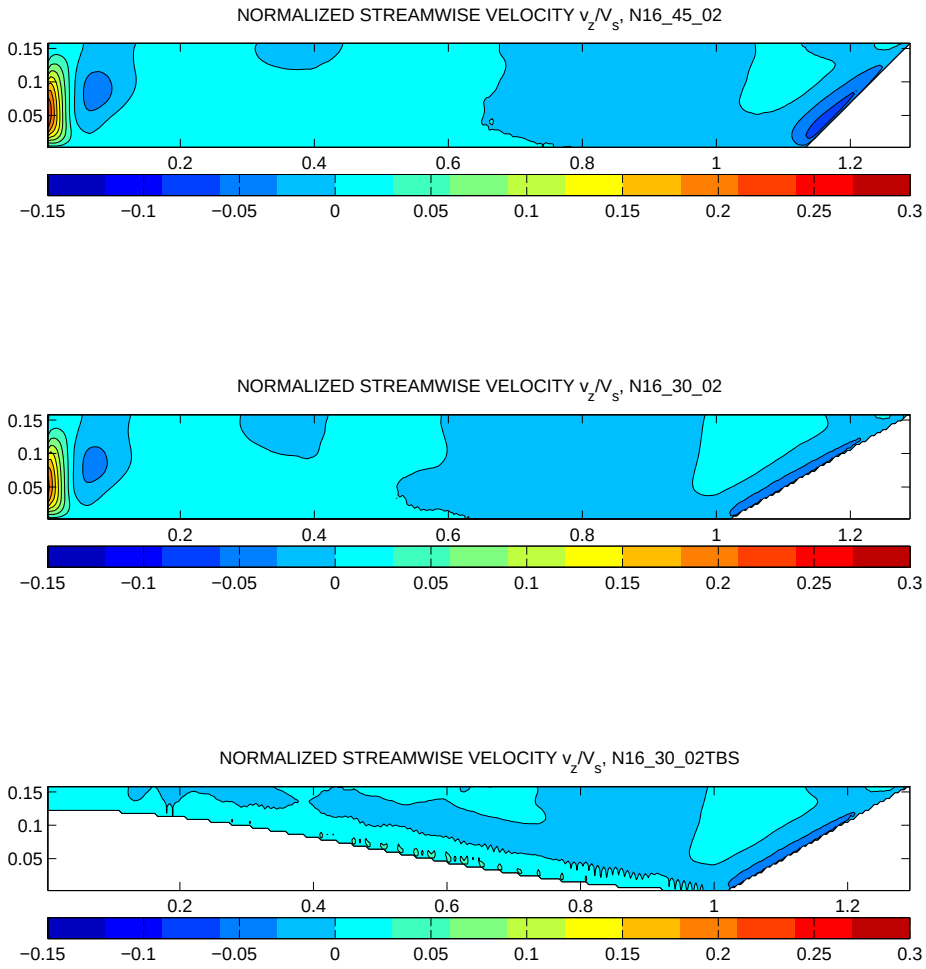

Figure 29: Cross section, showing the Normalized Vertical Flow Velocity for Calculations N16_45_02, N16_30_02 and N16_30_02TBS.

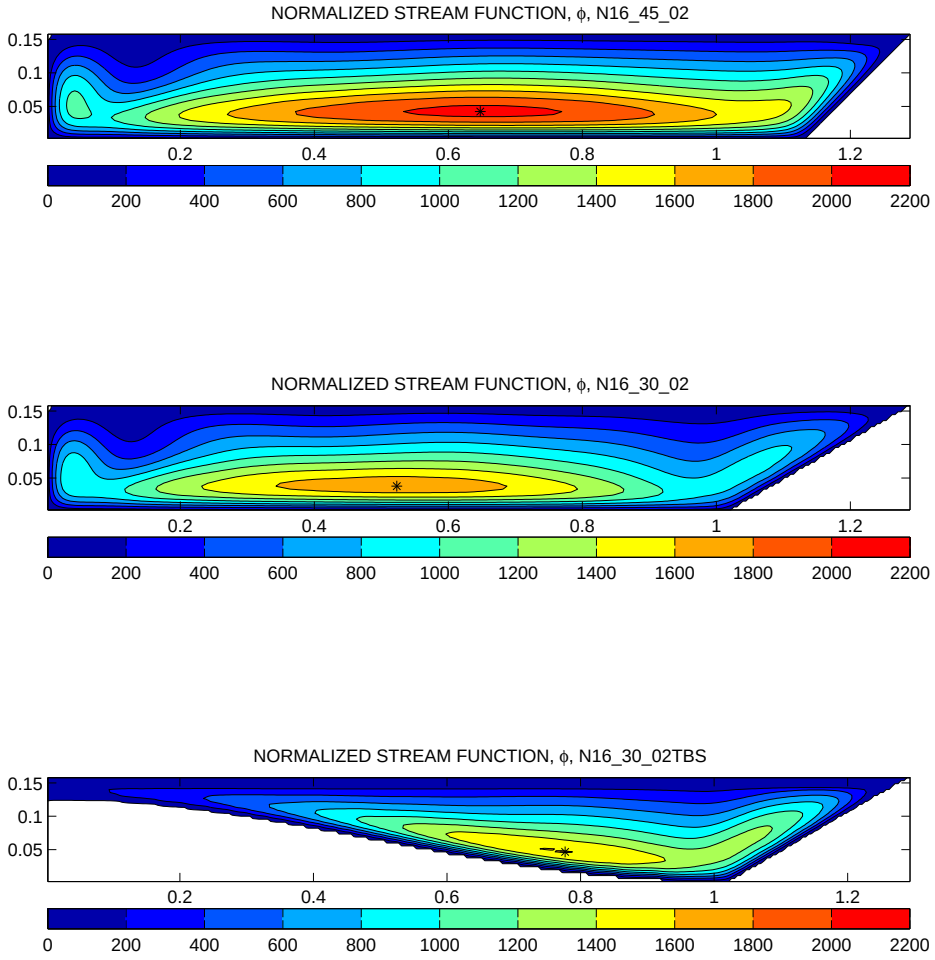

Figure 30: Cross section, showing the isolines of the Normalized Stream Function for Calculation N16_45_02, N16_30_02 and N16_30_02TBS.

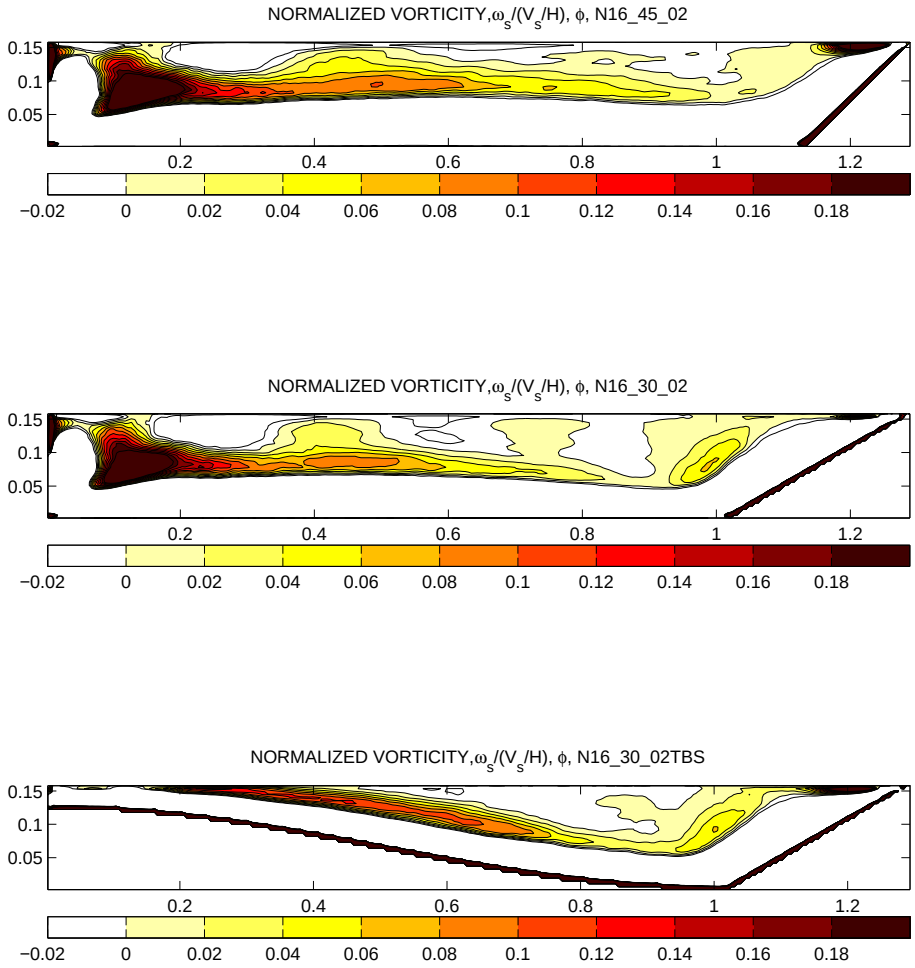

Figure 31: Cross section, showing the normalized vorticity for Calculation N16_45_02, N16_30_02 and N16_30_02TBS. The graphs only shows the positive values, all negative values are assigned white.

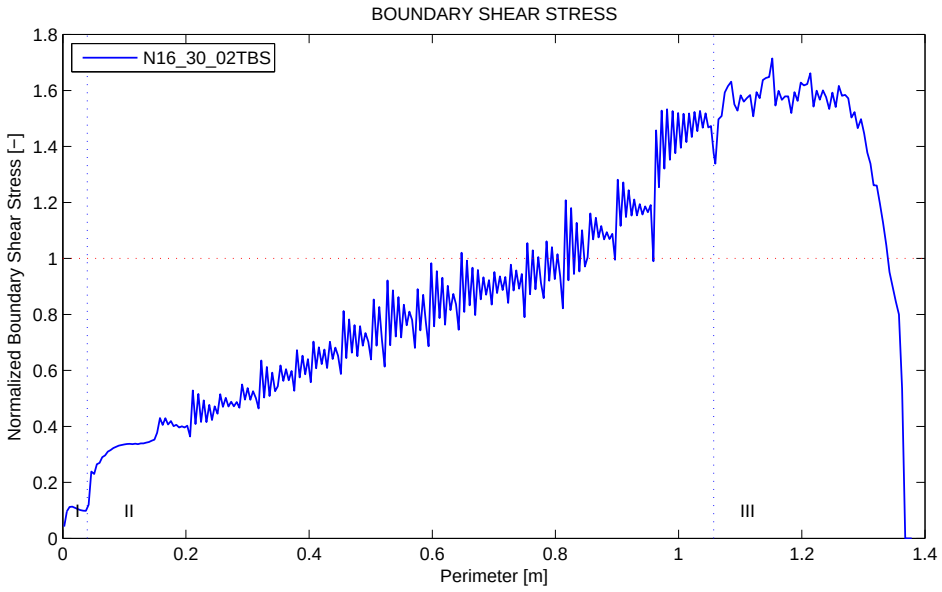

Figure 32: The boundary shear stress along the perimeter, normalized by the average boundary shear stress, for the calculation N16_30_02TBS. (I) denotes the smooth inner bank; (II) the bed and; (III) the inclined outer-bank. The variations in the boundary shear stress are due to the Immersed Boundary Method and are explained in Section 6.4

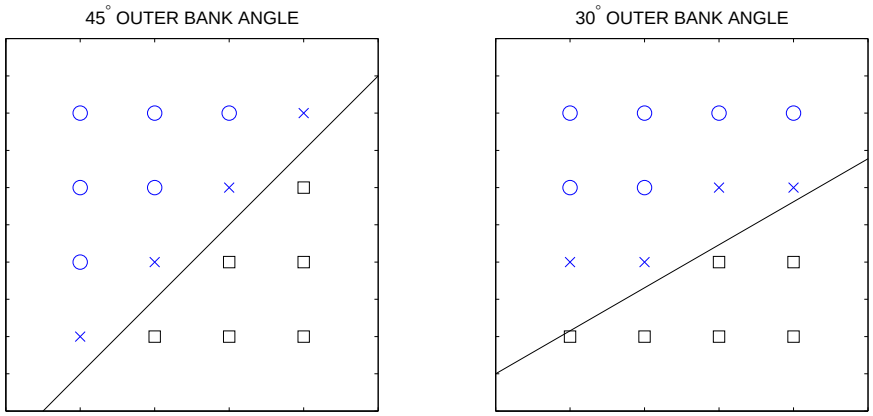

Figure 33: Example, showing the grid points and the embedded boundary. The black squares are solid point and the blue points are fluid points of which the rounds normal fluid points and the crosses ghost points.

7 Conclusions and Recommendations

7.1 Conclusions

The magnitude of the outer-bank shear stress and the outer-bank cell increase for increasing roughness of the outer-bank, leading to a less uniform distribution of the outer-bank shear stress. The magnitude of the outer-bank shear stress decreases for increasing inclination of the outer-bank. For a more inclined outer-bank, the magnitude of the outer-bank shear stress is more dependent on the outer-bank roughness. No significant dependency of the distribution of the outer-bank shear stress on the outer-bank inclination can be found from the results. Inclusion of the point bar related transverse bed slope does not lead to a significant change of the magnitude and distribution of the outer-bank shear stress. Clearly, the helical motion outscores the effect of topographic steering.

Regarding the performance of the algorithm in describing the boundary shear stress it is shown that the Immersed Boundary Method is prone to errors and is less robust than the Normal Wall Function Approach. The near wall velocity profile obtained using the Immersed Boundary Method does not often coincide with the actual momentum 'loss' at the wall. This problem, not recognized in earlier studies, is understood and partly solved. Hence, for some calculations the accuracy of the algorithm in describing the boundary shear stress is quite good, while it is not for others. The inaccuracy can be attributed to the description of the turbulent viscosity in the fluid cells bordering the ghost cell. This turbulent viscosity is computed by the Smagorinsky Model, although the assumptions of anisotropy and inhomogeneity are not valid. It is suggested that coarsening the grid improves the accuracy of the boundary method. Coarsening the grid, however, leads to other negative effects. Among others, it diminishes the turbulence that is captured by the grid. The accuracy of the boundary method can also be improved by reconsidering the implemented Smagorinsky Model. The turbulence closure model can be made direction dependent or a different Smagorinsky Model can be used. `Lévêque et. al. [2006]` proposes an improved Smagorinsky Model which is presumed to be performing well in complex non-homogeneous turbulent flows.

7.2 Recommendations

As stated in the introduction, the current parameterizations of the bank shear stress are not optimal applying to naturally curved flows. This thesis does not provide a new parameterization that is applicable to these flows. However, this thesis provides a good starting point for future research: an improved numerical approach. The results are compared with experimental data for validation. Continuing with this approach in order to find the desired parameterizations requires: (1) Further improvement and validation of the numerical algorithm. An elaborated convergence analysis might reveal the ideal grid size. Reassessing the implemented Smagorinsky Model might assure a good performance of the boundary method; (2) A broad variety of calculated cases. Curve-fitting parameterizations requires more extensive research than what was performed here (two different bank inclinations, three different bank roughnesses and one transverse bed slope); (3) Experimental or field data to compare with the numerical results. At the moment, no data of bank shear stress in curved flow with a transverse bed slope is available. Collecting this data would be a good subject of further study. Appendix G contains subject for further research.

Dankwoord

Het bestaan van de modelleur is eenzaam. Niemand kent het model zo goed als jij en bij problemen en foutmeldingen ben je voornamelijk op jezelf aangewezen. Dit neemt niet weg dat ik bij dit onderzoek veel hulp heb gekregen en hiervoor ben ik verschillende mensen mijn dank verschuldigd.

Maar allereerst wil ik de lezer bedanken dat hij/zij de moeite heeft genomen dit rapport door te lezen. In de hoop de uw interesse en nieuwsgierigheid gewekt te hebben wil ik er meteen aan toevoegen dat u bij vragen of opmerkingen over het rapport of het model niet hoeft te twijfelen met mij contact op te nemen.

Mijn begeleiders, Wim Uijttewaal, Alessandra Corsato en Erik Mosselman wil ik graag bedanken voor hun hulp, advies en opbouwende kritiek. Verder wil ik bedanken: Wim van Balen en Willem Ottevanger, mijn voorgangers die aan de LES-code gewerkt hebben, voor de lunchpauzes die ze hebben besteed om mij de structuur van het model uit te leggen; Koen Blanckaert voor het gebruik van zijn laboratorium data; Marcel Zijlema voor zijn voor zijn advies aangaande numeriek berekeningen; Frank Everdij, die me geholpen heeft het model draaiende te krijgen op het rekencluster; Mijn vriendin Anaïs voor het nakijken van het rapport op taalfouten en onduidelijkheden.

Voor hun ondersteuning tijdens mijn studie wil ik graag mijn familie bedanken en voor de mooie tijd in Delft mijn vrienden, huis- en studiegenoten.

References

[1] A.A.I. Alhamid (1991) "Boundary shear stress and velocity distributions in differentially roughened trapezoidal open channels" *University of Birmingham*

[2] E. Balaras (2004) "Modeling complex boundaries using an external force field on fixed cartesian grids in large-eddy simulations." *Computers and Fluids*, **33**, pp. 375–404

[3] W. van Balen (2010) "Curved open-channel flows, A numerical study" *TU DELFT*, **ISBN:** 978-90-6562-236-5

[4] K. Blanckaert and H.J. De Vriend (2003) "Nonlinear modeling of mean flow redistribution in curved open channels" *Water Resources Research*, **39**, No.12

[5] K. Blanckaert and H.J. De Vriend (2004) "Secondary flow in sharp open channel bends" *Journal of Fluid Mechanics*, **498** pp. 353-380

[6] K. Blanckaert and H.J. De Vriend (2005) "Turbulence structure in sharp open channel bends" *Journal of Fluid Mechanics*, **536**, pp. 27-48

[7] K. Blanckaert, A.J. Duarte and A.J. Schleiss (2010) "Influence of shallowness, bank inclination and bank roughness on the variability of flow patterns and boundary shear stress due to secondary currents in straight open-channels" *Advances in Water Resources*, **33**, pp. 1062-1074

[8] K. Blanckaert (2011) "Hydrodynamic processes in sharp meander bends and their morphological implications" *Journal of Geophysical Research*, **116**

[9] J.V. Boussinesq (1877) "Essai sur la théorie des eaux courantes" *Mémoires présentés par divers savants à l'Académie des Sciences*, **23(1)**, pp. 1-680

[10] V.T. Chow (1959) "Open-channel hydraulics" *McGraw-Hill Book Company*, **ISBN:** 07-010776-9

[11] R.W. Cruff (1965) "Cross-Channel Transfer of Linear Momentum in Smooth Rectangular Channels. Laboratory studies of open-channel flow." *GEOLOGICAL SURVEY WATER-SUPPLY PAPER*

[12] A. O. Demuren W. Rodi (1986) "Calculation of flow and pollutant dispersion in meandering channels" *Journal of Fluid Mechanics*, **172**, pp. 63–92

[13] J.F. Douglas, J.M. Gasiorek, J.A. Swaffield and L.B. Jack (2011) "Fluid Mechanics Sixth Edition" *PEARSON*, **ISBN:** 978-0-273-71772-0

[14] A.J. Pesanha de Oliveira Caimoto Duarte (2008) "An Experimental Study on Main Flow, Secondary Flow and Turbulence in Open-Channel Bends with Emphasis on their Interaction with the Outer-Bank Geometry" *EPFL*, **THÈSE NO:** 4227

[15] J.G.M. Eggels (1994) "Direct and Large Eddy Simulation of Turbulent Flow in a Cylindrical Pipe Geometry" *TU DELFT*, **ISBN:** 90-6275-940-8

[16] K. Houjou, Y Shimizu and C. Ishii (1990) "Calculation of boundary shear stress in opebn channel flow" *Journal of Hydroscience and Hydraulic Engineering*, **8**, No.2 pp. 21-37

[17] G.H. Keulegan (1938) "Laws of turbulent flow in open channels" *Natl. Bur. Standards Jour. Research*, **21**, pp. 707-741

[18] D.W. Knight, A.A.I. Alhamid and K.W.H. Yuen (1994) "Boundary shear stress distributins in open-channel flow" in Physical Mechanisms of mixing and transport in the environment, Ch.4, (ed. K. Beven, P. Chatwin and J. Millbank) *J. Wiley*, pp. 51-87

[19] E.W. Lane (1955) "Design of stable channels" *Transactions, Am. Soc. Civil Eng.*, **120**, pp. 1234-1279

[20] H.J. Leutheusser (1963) "Turbulent flow in rectangular ducts" *Journal of the hydraulic division Proceedings of the A.S.C.E.*, **89**, pp. 1-19

[21] E. Lévêque, F. Toschi, L. Shao and J-P. Bertoglio (2006) "Shear-Improved Smagorinsky Model for Large-Eddy Simulation of Wall-Bounded Turbulent Flows" *Journal of Fluid Mechanics*

[22] R. Mittal and G. Iaccarino (2005) "IMMERSED BOUNDARY METHODS" *Annual Review of Fluid Mechanics*, **37**, pp. 239-261

[23] I. Nezu and H. Nakagawa (1993) "Turbulence in open-channel flows" *Balkema Rotterdam*, **ISBN:** 90-5410-118-0

[24] K.W. Olesen (1987) "Bed topography in shallow river bends" *TU DELFT*

[25] W. Ottevanger (2013) "Modelling and parameterizing the hydro- and morphodynamics of curved open channels" *TU DELFT*, **ISBN:** 978-94-6191-925-0

[26] M.J.B.M. Pourquié (1994) "Large-eddy Simulationof a Turbulent Jet" *TU DELFT*, **ISBN:** 90-407-1061-9

[27] L. Prandtl (1952) "Führer durch die Strömungslehre"

[28] A. Tominaga, I. Nezu, K. Ezaki and H. Nakagawa (1989) "Three-dimensional turbulent structure in straight open channel flows" *Journal of Hydraulic Research*, **27**, No.1 pp. 149-173

[29] H.J. Tracy and C.M. Lester (1961) "Resistance coefficients and velocity distribution, smooth rectangular channel" *GEOLOGICAL SURVEY WATER-SUPPLY PAPER*

[30] W.J.S. Uijttewaal "Lecture Notes CIE5312: Turbulence in Hydraulics"

Hydraulic Engineering, TU Delft

Appendix

to the Master Thesis of A.W. van der Meer

Delft University of Technology
Faculty of Civil Engineering and Geosciences
Department of Fluid Mechanics

October 28, 2015

A Stream Function

The Lagrange stream function is: 'A scalar function of position used to describe steady incompressible 2D flow.' Constant values of the stream function give the streamlines. The rate of flow between the streamlines (per unit width) is equal to the difference between the value of the stream function on the streamlines. Since the stream function is the rate of flow per unit depth (`Douglas et al. [2011]`):

$$\begin{aligned} d\phi &= v_x dy - v_y dx \\ \phi &= \int v_x dy - \int v_y dx \end{aligned} \tag{28}$$

where ϕ is in [m^2/s]. For small spatial steps the following equation is valid:

$$d\phi = \frac{\partial \phi}{\partial x} dx + \frac{\partial \phi}{\partial y} dy \tag{29}$$

From Equations 28 and 29, the relationship between the velocity and the stream function can be obtained:

$$\begin{aligned} v_x &= \frac{\partial \phi}{\partial y} \\ v_y &= -\frac{\partial \phi}{\partial x} \end{aligned} \tag{30}$$

Cylindrical Coordinate System

Mass conservation equation cross sectional plane:

$$\frac{1}{r} \frac{\partial r v_n}{\partial n} + \frac{\partial v_z}{\partial z} = 0 \tag{31}$$

Including the expression for the stream function leads to:

$$\begin{aligned} \frac{1}{(R+n)} \frac{\partial (R+n) \left(-\frac{\partial \phi}{\partial z} \right)}{\partial n} + \frac{\partial v_z}{\partial z} &= 0 \\ \frac{R}{(R+n)} \frac{\partial \phi}{\partial n} &= v_z \end{aligned} \tag{32}$$

And for the other:

$$\begin{aligned} \frac{1}{(R+n)} \frac{\partial (R+n) v_n}{\partial n} + \frac{\partial \frac{\partial \phi}{\partial n}}{\partial z} &= 0 \\ \frac{R}{(R+n)} \frac{\partial \phi}{\partial z} &= -v_n \end{aligned} \tag{33}$$

Normalized Stream Function

The stream function can be normalized by dividing by the water depth and bulk velocity (Equation 34). This makes sense, since the stream function is obtained by integrating over the water

depth and since the importance of the circulation depends on its strength relative to the stream-wise velocities.

$$\begin{aligned} \frac{hR}{(R+n)}\frac{\partial\phi}{\partial n} &= \frac{v_z}{V_s} \\ \frac{hR}{(R+n)}\frac{\partial\phi}{\partial z} &= -\frac{v_n}{V_s} \end{aligned} \tag{34}$$

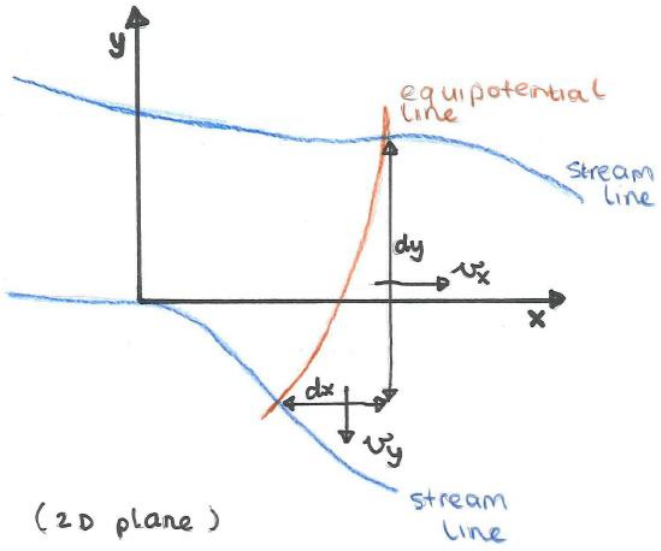

Figure 34: Stream function

B Wall Functions

Describing the boundary layer a distinction has to be made between a rough boundary and a smooth boundary (Figure 35, Table 12 and Equation 35) because the different layers as described for smooth boundaries can practically not be distinguished for rough boundaries. The boundary layer theory is valid for shear flows, flows where the mean motion varies only little in streamwise direction and varies much in the perpendicular direction. The velocity distribution for the region outside the wall region (the outer layer) is, however, not part of the wall functions. In the outer layer secondary circulations can play an important role. For completeness the equation for the outer layer is included anyway. Also the description of the turbulent viscosity near the wall, following from the velocity profiles and constant shear stress approximation is included.

$$k_s^+ = k_s \frac{u_*}{\nu} \tag{35}$$

Smooth	Rough
$k_s^+ < 5$	$k_s^+ > 70$

Table 12: Application smooth and rough wall functions.

Smooth Wall

For a smooth wall, the wall region can be further divided into three layers (Figure 37). Shear stress contains of viscous and turbulent part (Equation 36) and goes from zero at the core of the flow (or water level) linearly to maximum at the flow boundary. For each layer different assumptions are made. The position of the layers can be generalized using wall coordinates (Equation 37 and Table 13).

$$\tau = q_{xy} - \rho\nu \frac{\partial \bar{v_s}}{\partial z} \tag{36}$$

$$\begin{aligned} z^+ &= \frac{u_* z}{\nu} \\ \bar{v_s}^+(z) &= \frac{\bar{v_s}(z)}{u_*} \end{aligned} \tag{37}$$

Viscous Sublayer	Buffer Layer	Inner Layer	(Outer Layer)
$z^+ < 5$	$5 < z^+ < 30$	$30 < z^+ < 100$	$z^+ > 100$
Const. Shear Stress	Const. Shear Stress	Const. Shear Stress	Law of the Wake
q_{sz} Neglected	$\tau = q_{sz} - \rho\nu \frac{\partial \bar{v_s}}{\partial z}$	$\rho\nu \frac{\partial \bar{v_s}}{\partial z}$ Neglected	$\tau = -\rho \lvert u_* \rvert u_* (z/h - 1)$
$\tau = -\rho\nu \frac{\partial \bar{v_s}}{\partial z}$		$\tau = -\rho \lvert u_* \rvert u_*$	
$\bar{v_s}(0) \equiv 0$		$v_{s,il}(z_0) \equiv 0$	

Table 13: Assumptions smooth 'Law of the Wall'.

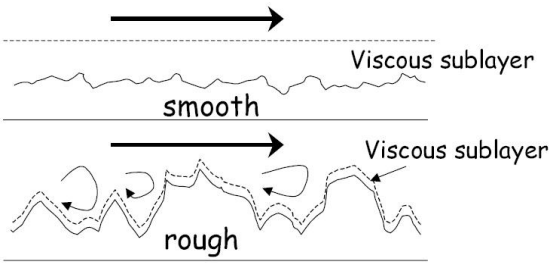

Figure 35: Definition smooth and rough boundary. Adjusted from `lecture notes CIE5312`.

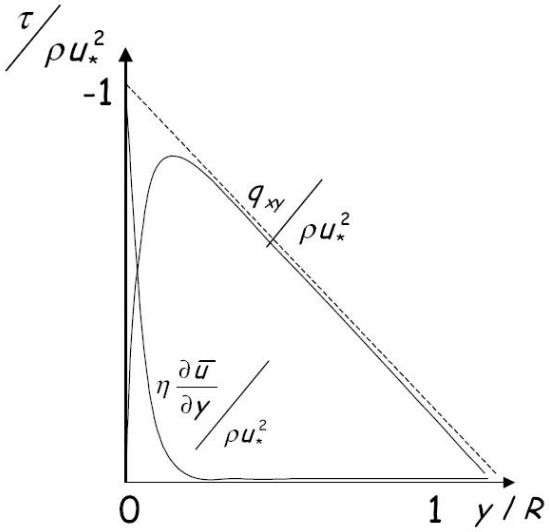

Figure 36: Internal shear stress distribution including the contribution of turbulent and viscous shear (`lecture notes CIE5312`).

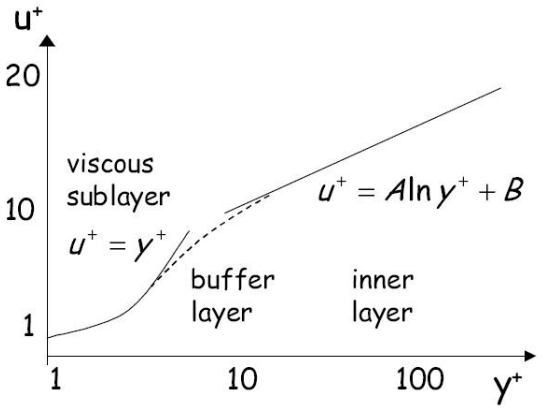

Figure 37: Different layers used in the smooth wall functions (`lecture notes CIE5312`).

Viscous Sublayer Closest to the wall the viscous shear stresses dominate. The turbulent shear stresses are neglected ($q_{sz} = -\rho\overline{v_s' v_w'} = 0$) and the shear stress is assumed to be constant and equal to the boundary shear stress. Integrating the shear stress equation ($\tau = \tau_0 = -\rho\nu\frac{\partial \bar{v_s}}{\partial z}$) and defining $\bar{v_s}(0) \equiv 0$ the velocity distribution for the viscous sublayer (Equation 38) is obtained.

$$\begin{aligned} \frac{\bar{v_s}(z)}{u_*} &= \frac{u_* z}{\nu} \\ \bar{v_s}^+(z) &= z^+ \end{aligned} \tag{38}$$

Turbulent Inner Layer This layer, also known as the 'Prandtl-Von Karman Universal-Velocity-Distribution Law', 'Law of the Wall' or 'Inner Law of Velocity Distribution', is dominated by turbulent shear stresses. The viscous shear stresses are neglected ($-\rho\nu\frac{\partial \bar{v_s}}{\partial z} = 0$) and the shear stress is assumed to be constant and equal to the boundary shear stress. Integrating the shear stress equation ($\tau = \tau_0 = q_{sz} = -\rho\,|u_*|\,u_*$) and defining a reference level (z_0, where $v_{s,il}(z_0) \equiv 0$) the velocity distribution for the Inner Layer (Equation 39) is obtained.

$$\begin{aligned} \bar{v_s}^+(z) &= \frac{1}{\kappa}\log_e(\frac{z}{z_0}) \\ &= 2.5\log_e(z^+) + 5.5 \end{aligned} \tag{39}$$

Buffer Layer In this layer both viscous and turbulent shear stresses are important ($\tau = q_{sz} - \rho\nu\frac{\partial \bar{v_s}}{\partial z}$). This equation can't be solved analytically. Equation 40 is adopted for the Buffer Layer. The equation matches the Viscous Sub- (at $z^+ = 5$) and Turbulent Inner Layer (at $z^+ = 30$).

$$\bar{v_s}^+(z) = 5.0\log_e(z^+) - 3.5 \tag{40}$$

Rough Wall

For the rough boundary the regions can not be distinguished easily (Figure 12). Here the following relation replaces the relation for the Viscous Sub-, Buffer and Inner Layer. Where k_s is the Nikuradse roughness height. The equation is valid for $z > \frac{k_s}{30}$.

Rough Wall Layer	(Outer Layer)
Constant Shear Stress	Law of the Wake
$\rho\nu\frac{\partial \bar{v_s}}{\partial z}$ Neglected	$\tau = -\rho\,\lvert u_*\rvert\,u_*(1 - z/h)$
$\tau = -\rho\,\lvert u_*\rvert\,u_*$	
$v_s(z_0) = v_s(\frac{k_s}{30}) \equiv 0$	

Table 14: Assumptions rough 'Law of the Wall'.

$$\begin{aligned} \bar{v_s}(z) &= \frac{u_*}{\kappa}\log_e(\frac{z}{z_0}) \\ &= \frac{u_*}{\kappa}\log_e(z\frac{30}{k_s}) \end{aligned} \tag{41}$$

Outer Layer

This layer, also known as the 'Velocity Defect Law' or 'Outer Law of Velocity Distribution', is dominated by turbulent shear stress. The shear stress can, however, not be assumed to be constant (Figure 36) and is decreases linearly towards zero at the free surface/core of the flow ($\tau = \rho |u_*| u_*(z/h - 1)$, where h is the water depth). The macroscopic dimensions of the flow geometry are important (which explains the use of h in the equation). Proximity of the wall and molecular viscosity plays no role thus the flow will be independent of the Reynolds number. Based on empirical approximations Equation 42 is obtained. Where $V_{s,0}$ is a reference velocity (or the velocity at the free surface), with constant B the equation can be matched to the wall functions and $h(z/h)$ represents the 'Law of the Wake'.

$$\frac{V_{s,0} - \bar{v_s}}{u_*} = -\frac{1}{\kappa} \log_e (z/h) + B + h(z/h) \tag{42}$$

Turbulent Viscosity

In the Viscous Sublayer the molecular viscosity is assumed to much more important than the turbulent effects. Hence the turbulence is neglected and no expression for the turbulent viscosity can be derived. In the Turbulent Inner Layer an expression for the turbulent viscosity can be derived. The turbulent viscosity is defined according to Equation 43.

$$\begin{aligned} \tau &= \rho \nu_t \frac{\partial v_s}{\partial z} \\ &= -\rho |u_*| u_* \end{aligned} \tag{43}$$

Knowing $u_* = \kappa z \frac{\partial v_s}{\partial z}$ and introducing $\nu_t^+ = \frac{\nu_t}{\nu}$ leads to Equation 44.

$$\nu_t^+ = \kappa z^+ \tag{44}$$

Combining Equations 39 and 44 indeed meets the assumption of constant shear stress.

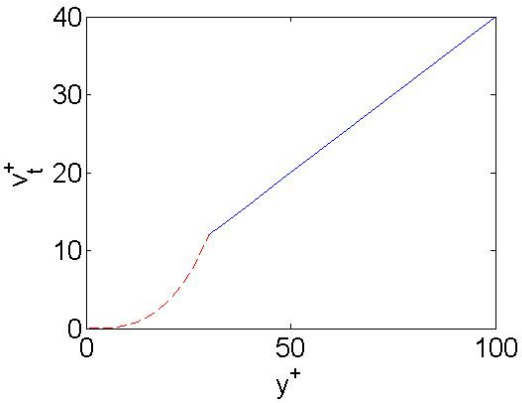

Figure 38: Turbulent viscosity profile.

C Transverse Bed Slope

To derive a relation for the transverse bed slope a cross section within a river bend is considered. Determining the bed shear stress direction and the sediment transport direction will lead to the desired transverse bed slope relation.

Bed Shear Stress Direction

The bed shear stress, τ_b, can be split into a transverse, τ_{bn}, and a streamwise, τ_{bs}, component. The transverse bed shear stress can on its turn be split into a part related to the cross current, τ_{bn}^{γ}, and a part related to the secondary circulations, τ_{bn}^{*}. According to `Olesen [1987]`:

$$\tau_{bs}(n) = \rho C_f V_s^2(n) \tag{45}$$

$$\tau_{bn}^{\gamma}(n) = \rho C_f V_s(n) V_n(n) \tag{46}$$

where ρ is the density of water, C_f is the dimensionless friction coefficient, $V_s(n)$ the depth averaged streamwise velocity and $V_n(n)$ the depth averaged transverse velocity. Since a cross section is considered it should be mentioned that the transverse and streamwise velocities vary in transverse direction.

The transverse bed shear stress related to the secondary flow can be approximated as follows (`Ottevanger [2013]`):

$$\frac{\tau_{bn}^{*}}{\tau_{bs}}(n) = g_{\tau}(n) \left(\frac{\tau_{bn}^{*}}{\tau_{bs}} \right)_{n=0} \tag{47}$$

where $g_{\tau}(n)$ is a dimensionless distribution function of the bed shear stress direction over the channel width.

$$\left(\frac{\tau_{bn}^{*}}{\tau_{bs}} \right)_{n=0} = H \left(\frac{\alpha_{\tau\infty}}{\alpha_{\tau 0}} \right) \left(\frac{\alpha_{\tau 0}}{R} \right) \tag{48}$$

where H is the water depth in $n = 0$, $\alpha_{\tau 0}/R$ represents the solution of the bed shear stress direction by a linear model and $\alpha_{\tau\infty}/\alpha_{\tau 0}$ is the reduction factor for nonlinear effects posed by `Blanckaert and de Vriend [2003]`. The reduction factor depends on the Bend Parameter (Figure 39). The Bend Parameter is posed by `Blanckaert and de Vriend [2003]` and is a collection of the variables that determine the transverse velocity distributions:

$$\beta = (C_f)^{-0.275} (H/R)^{0.5} (\alpha_s + 1)^{0.25} \tag{49}$$

where α_s is the normalized transverse velocity gradient:

$$\alpha_s = \left(\frac{\partial V_s}{\partial n} / \frac{V_s}{R} \right)_{n=0} \tag{50}$$

Bed Load Transport Direction

However, without wandering away from the subject, the direction of the bed load transport is given (`Ottevanger [2013]`):

$$\frac{s_{bn}}{s_{bs}}(n) = \frac{\frac{\tau_{bn}}{\|\vec{\tau_b}\|}(n) - G\frac{\partial z_b}{\partial n}(n)}{\frac{\tau_{bs}}{\|\vec{\tau_b}\|}(n) - G\frac{1}{1+n/R}\frac{\partial z_b}{\partial s}(n)} \tag{51}$$

where $\frac{\tau_{bn}}{\|\vec{\tau_b}\|}(n)$ is the ratio between the transverse and the total bed shear stress, $\frac{\tau_{bs}}{\|\vec{\tau_b}\|}(n)$ the ratio between the streamwise and the total bed shear stress, G the chosen gravitational pull model (which can be related to the dimensionless shear stress), z_b the bed elevation and $\frac{1}{1+n/R}$ corrects for an non-orthogonal grid. Assuming very small streamwise slopes and assuming $\frac{\tau_{bs}}{\|\vec{\tau_b}\|} \approx 1$ the equation can be simplified to:

$$\frac{s_{bn}}{s_{bs}}(n) = \frac{\tau_{bn}}{\tau_{bs}}(n) - G\frac{\partial z_b}{\partial n}(n) \tag{52}$$

Following from the knowledge about the bed shear stress (Equations 45 to 47), it follows that:

$$\frac{s_{bn}}{s_{bs}}(n) = \frac{V_n}{V_s}(n) - H\frac{\alpha_{\tau\infty}}{R}g_\tau(n) - G\frac{\partial z_b}{\partial n}(n) \tag{53}$$

"This expression shows that the direction of the bed load transport vector deviates from the direction of the depth averaged velocity due to two effects" (`Ottevanger [2013]`). This is caused by secondary flow effects and by gravity.

Transverse Bed Slope

Rearranging Equation 53 gives an expression for the transverse bed slope:

$$\frac{\partial z_b}{\partial n}(n) = \frac{\frac{V_n}{V_s}(n) - H\frac{\alpha_{\tau\infty}}{R}g_\tau(n) - \frac{s_{bn}}{s_{bs}}(n)}{G} \tag{54}$$

Now assuming fully developed conditions, thus no gradients in sediment transport and no meander currents the equation can be simplified to (`Ottevanger [2013]`):

$$\frac{\partial z_{be}}{\partial n}(n) = -\frac{H}{G}\frac{\alpha_{\tau\infty}}{R}g_\tau(n) = -A_e\frac{H}{R}g_\tau(n) \tag{55}$$

The dimensionless numbers G and $\alpha_{\tau\infty}$ can be combined in a dimensionless scour factor, A_e. Depending on the choice of g_τ, by integration, an expression for the transverse bed slope will arise.

Hence, assuming a sinusoidal profile for g_τ, defining h_m to be the mean water depth, relating the water depth to the bed elevation according to $h = z_w - z_b$ and assuming zw constant, the water depth as a function of the transverse location can be expressed by Equation 56.

$$h = h_m\left(1 + \frac{b}{\pi}\frac{A}{R}\sin\left(\frac{\pi}{b}n\right)\right) \tag{56}$$

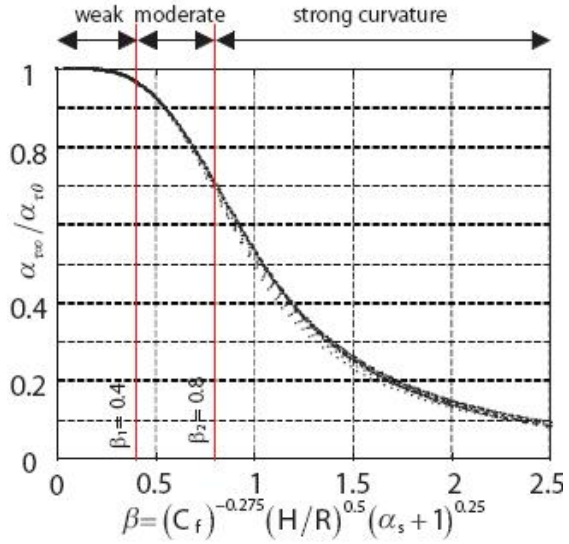

Figure 39: Reduction factor for nonlinear effects as a function of the Bend Parameter (`Ottevanger [2013]`).

D Manual of the Large Eddy Simulator

by A.W. van der Meer

Introduction

Modeling is really fun and the rapid increase in computer power provides us more and more opportunities. Which is really convenient but also is a big challenge. Usually the modeler continues on a model made by others, changing or implementing new algorithms increasing the performance of the model but also making it more and more complex. Always mistakes are made. Unfortunately, lacking proper documentation and time, these errors are often not recognized by reviewers and researchers building on the model. As result these errors will stay in the model and as the model grows they become more and more difficult to find. In the worst case this might make the model useless. Offering researchers using the described model this extensive manual, I attempted to provide them with sufficient information to build on the model as I left it and to uncover my mistakes (which are hopefully not a lot).

The model builds on the work of `Ottevanger [2013]`, `Van Balen [2010]`, `Eggels [1994]` and `Pourquié [1994]`. The contribution of the author to the algorithm is mainly characterized by adjustments. The core of the algorithm and the Immersed Boundary Method were already available. The only new feature in the algorithm is a shear stress output for the Immersed Boundary Method, including a new subroutine (`shearstressupdate`) which allows for the simultaneous use of the IBM and the 'Normal Wall Function Approach'. Adjustments regard: (1) For the IBM, the velocity description in the ghost cell. According to Equation 17, a body force is implemented on the basis of a 'hypothesized' velocity. Subroutine `fluidcell` calculates this velocity. Combining Equation 17 and 18 shows that the body force can easily be included according to Equation 19.

$$\begin{aligned} RHS_i + f_i &= \frac{v_i^{n+1} - v_i^n + \Delta t \left(RHS_i - \frac{\hat{v}_i^{n+1} - v_i^n}{\Delta t} \right)}{\Delta t} \\ &= \frac{v_i^{n+1} - \hat{v}_i^{n+1} + \overbrace{\Delta t \left(RHS_i \right)}^{\text{Missing}}}{\Delta t} \end{aligned} \tag{57}$$

The denoted part was missing, which is corrected by the author. The adjustment also required some adjustments in other subroutines (Appendix D). Note that by including the 'incorrect' subroutine `fluidcell` twice in the algorithm, for equilibrium flow, this mistake does not lead to a deviation in the flow field. However, since it was not properly documented, the concerned subroutine was not always included twice.

(2) For the IBM, the description of the turbulent viscosity in the ghost cell (described in subroutine `fluidvisc`). Close to the wall, the turbulent viscosity in the ghost cell was defined to depend on the the distance from the wall cubed. The viscosity profile was calibrated with the turbulent viscosity in the interpolated point (Figure 41) This might only lead to an accurate result having both the first two grid cells in the viscous sub- or buffer layer (Appendix B). However, this is often not the case. The author defined the turbulent viscosity to be described according to $\nu_t^+ = \kappa z^+$ (Appendix B).

(3) Implementation of the potential vortex distribution in a dimensional correct way (described in subroutine `momsource`).

(4) Removing unnecessary/unused variables and subroutines, making the algorithm computational less expensive and easier to understand and adapt. The removed subroutines are the subroutines related to the RANS part of the model and all different subroutines that were made with the intention to model a specific case. Most of these subroutines were started but not finished.

Outline

In this manual first background information is provided. Secondly, the main file and different versions are treated. Thirdly, the subroutines, parameter and technical files are explained. Where after all the variables in the model are listed and elaborated on. The manual ends with useful literature, some remarks and suggestions for further improvements. The major part of the manual is written by the author, but some parts are literary copied from `Van Balen [2008]`.

Background

The algorithm solves the Navier-Stokes Equations numerically. The algorithm is a Finite Volume Model with pressure-correction algorithm on a staggered mesh (Figure 40).

Governing Equations

$$\begin{aligned} \frac{1}{r}\frac{\partial ru}{\partial r} &+\frac{1}{r}\frac{\partial v}{\partial \theta} &+\frac{\partial w}{\partial z} &= 0 \\ \frac{\partial u}{\partial y} &+\frac{\partial v}{\partial x} &+\frac{\partial w}{\partial z} &= 0 \end{aligned} \tag{58}$$

$$\begin{aligned} \overbrace{\frac{\partial u}{\partial t}}^{I} &+\overbrace{\frac{1}{r}\frac{\partial ruu}{\partial r}}^{II} &+\overbrace{\frac{1}{r}\frac{\partial uv}{\partial \theta}}^{III} &+\overbrace{\frac{\partial uw}{\partial z}}^{IV} &-\overbrace{\frac{v^2}{r}}^{V} &=\overbrace{-\frac{\partial p}{\partial r}}^{VI} &+\overbrace{\nu\left(\nabla^2 u-\frac{u}{r^2}-\frac{2}{r^2}\frac{\partial v}{\partial \theta}\right)}^{VII}; \\ \frac{\partial v}{\partial t} &+\frac{1}{r}\frac{\partial rvu}{\partial r} &+\frac{1}{r}\frac{\partial vv}{\partial \theta} &+\frac{\partial vw}{\partial z} &+\frac{uv}{r} &=-\frac{1}{r}\frac{\partial p}{\partial r} &+\nu\left(\nabla^2 v-\frac{v}{r^2}+\frac{2}{r^2}\frac{\partial u}{\partial \theta}\right); \\ \frac{\partial w}{\partial t} &+\frac{1}{r}\frac{\partial rwu}{\partial r} &+\frac{1}{r}\frac{\partial wv}{\partial \theta} &+\frac{\partial ww}{\partial z} & &=-\frac{\partial p}{\partial z} &+\nu\left(\nabla^2 w\right) \end{aligned} \tag{59}$$

$$\begin{aligned} \frac{\partial u}{\partial t} &+\frac{\partial uu}{\partial x} &+\frac{\partial uv}{\partial y} &+\frac{\partial uw}{\partial z} & &=-\frac{\partial p}{\partial x} &+\nu\left(\nabla^2 u\right); \\ \frac{\partial v}{\partial t} &+\frac{\partial vu}{\partial x} &+\frac{\partial vv}{\partial y} &+\frac{\partial vw}{\partial z} & &=-\frac{\partial p}{\partial y} &+\nu\left(\nabla^2 v\right); \\ \frac{\partial w}{\partial t} &+\frac{\partial wu}{\partial x} &+\frac{\partial wv}{\partial y} &+\frac{\partial ww}{\partial z} & &=-\frac{\partial p}{\partial z} &+\nu\left(\nabla^2 w\right) \end{aligned}$$

where the Laplace tensor is defined by equation 60. Further, note that the velocities in the equations represent the real velocities and not the Reynolds averaged velocities.

$$\begin{aligned}\nabla^2 \equiv \frac{1}{r}\frac{\partial}{\partial r}\left(r\frac{\partial}{\partial r}\right) &+\frac{1}{r^2}\frac{\partial^2}{\partial \theta^2} &+\frac{\partial^2}{\partial z^2}\\ \nabla^2 \equiv \frac{\partial^2}{\partial x^2} &+\frac{\partial^2}{\partial y^2} &+\frac{\partial^2}{\partial z^2}\end{aligned} \tag{60}$$

Time Integration

Numerical Scheme Regarding the numerical scheme the second order explicit Adams-Bashfort, Equation 61, is used. Semi-implicit schemes did not result in a significant gain in time step and fully explicit methods, as Adams-Bashfort, greatly simplify the imposition of the boundary and the parallelization of the model (`Balaras [2004]`).

$$\begin{aligned}y^{n+1} &= y^n + \Delta t\left(1.5f^n - 0.5f^{n-1}\right)\\ y' &= f\end{aligned} \tag{61}$$

Pressure-Correction Algorithm Since the water level is imposed as a rigid-lid and the flow is not assumed hydrostatic, the pressure-correction method is used. This is a two steps method where first the flow field is solved using the momentum equations but violating the non-divergence criterion (predictor step). Secondly, in the corrector step the correction of the velocity field is computed through the pressure field. Solving the pressure equation is thus required here. The associated pressure equation and pressure Poisson solver will not be discussed here.

$$\begin{aligned}u^{n+1} &= u^n + \Delta t\left(1.5(-ADV + DIFF)^n - 0.5(-ADV + DIFF)^{n-1} - \nabla P^{n+1}\right)\\ u^* &= u^{n+1} + \Delta t \nabla P^{n+1}\\ &= u^n + \Delta t\left(1.5(-ADV + DIFF)^n - 0.5(-ADV + DIFF)^{n-1}\right)\\ \Delta t \nabla^2 P^{n+1} &= div(u^*)\end{aligned} \tag{62}$$

Boundary Conditions

Free Surface For the free surface, the free-slip condition and rigid lid approximation are applied. The latter means that at the free surface (rigid lid) instead of $w \neq 0$ and $p = 0$, $w = 0$ and $p \neq 0$ are applied. The approximation leads to a continuity error, which is however small when the super elevation of the free surface is small with respect to the channel depth (`Demuren and Rodi [1986]`).

In- and Outflow Conditions The fact that only axi-symmetric cases are modeled allows the use of periodic boundary conditions. This means that the velocity, viscosity and pressure in the most upstream grid points are equal to them in the most downstream grid points. Note that this requires a sufficiently long longitudinal length of the domain. Based on the results of `Van Balen [2010]` and `Ottevanger [2013]` the longitudinal length is chosen to be more or less equal to the width of the bend.

Main File and Versions

The main file calls all subroutines. Before starting the numerical calculation: (1) The input file is read; (2) The computation grid is determined; (3) The geometry of the fluid domain is determined; (4) The initial conditions are posed. Different options:

- The grid consists of a series of straight and curved parts. This can be defined by the parameters: NN1, NN2 etc (Subroutine makegrid).
- The initial conditions are read from a file or posed by a function (Subroutines init and startveld).

The computation loop consist of a predictor and corrector step. In the predictor step: (1) The sub-grid viscosity is computed by the Smagorinsky Model; (2) The advection-diffusion is solved assuming free slip conditions; (3) Momentum is added to the flow in order to account for the forcing term; (4) Momentum is subtracted from the flow, in order to account for the friction at the solid boundaries. Different options:

- For the Smagorinsky Model, there can be chose between the basic and the dynamic Smagorinsky Model.
- To account for the friction at the solid boundaries there can be chose between a simple implementation of the wall function, the two layer wall model or the Immersed Boundary Method.

In the corrector step there is accounted for non-divergence criterion. The different options are listed in Table 15.

Axisymmetric	Smagorinsky	Normal Wall Function Approach	Different
Developing	Dynamic Smagorinsky	Immersed Boundary Method	Pressure Solvers
		Two Layer Wall Model	

Table 15: Different options

Subroutines

Below all the subroutines present in the model are explained and discussed. The subroutines are divided over several files.

BOUNDAR.F

File containing all the subroutines that deal with the grid and initial and boundary conditions (except the IBM).

Mkgrid In this subroutine, the grid is defined. The only important parameter for the user of the model is the variable krom for the cases CaseRA and CaseRS, and the variables N1, N2 and N3 for the cases CaseTA and CaseTS. The variable krom is a two-dimensional array (basically the top-view on the geometry) that contains information on the curvature of the geometry: 0 denotes straight, 1 denotes left-turning curved and -1 denotes right-turning curved. The user can prescribe himself where in the array a curvature applies. The variables N1, N2 and N3 is a more general way to prescribe these locations. The use of the variables krom and N1, N2 and N3 will be made clear with an example later on. Makes `domain`, `grid` and `geometry` files in folder `data`?

Standard This subroutine deals with some initial stuff. Relevant is, however, the declaration of the directory-path that is specified here, by means of the variable `pad`. Important remark: throughout the model, the number of characters of the variable `pad` is fixed. Of course, the user can change this himself. Calls subroutines `MPI BCAST`, `PARSTRT` (for parallelization issues) and `PARINIT` (for parallelization issues).

Init In this subroutine the initial velocity field is prescribed. Two options are present: a 1/7 power law in only the vertical direction (optie = 1) and a 1/7 power law in both vertical and transverse direction (optie = 2). Random noise is add to the velocity distribution to 'trigger' the occurrence of turbulence. Without the noise turbulence would also occur (cause of round off errors), but in that case it would take more (spin up) time. When using multiple processors, the noise should not be the same for all the different parallized parts. Alternative is a hot start with: `startveld(0)` or read a file with `init` (optie = 3). Calls `random number`.

Zijwanden In this subroutine the law of the wall is applied to the sidewalls. This law of the wall is applied to the total wall-parallel velocity vector. One can choose whether the wall function for smooth or rough walls is applied.

$$\begin{aligned} \text{tauls} &= U_*^2 \frac{V}{\vec{U}} \\ \vec{U} &= \sqrt{V^2 + W^2} \end{aligned} \tag{63}$$

where `tauls` is the streamwise wall shear stress on the left sidewall [$\mathrm{m}^2/\mathrm{s}^2$], W is the interpolated vertical velocity in the V velocity node. U_* is the shear velocity calculated from the velocity vector, $\vec{U}$, using the rough or smooth wall functions.

Zijwandenupdate Updates the velocity in the boundary point using the in subroutine `zijwanden` obtained wall shear stress. For the streamwise velocity on the left side wall this looks like:

$$\mathrm{Vbound}(1,j,k) = \mathrm{Vbound}(1,j,k) - \frac{\mathrm{tauls}(j,k)\cdot \mathrm{dt}}{\mathrm{dr}} \tag{64}$$

$$\begin{aligned} m\Delta u &= F\mathrm{dt} \\ \rho \mathrm{dxdydz}\Delta u &= \tau \mathrm{dydzdt} \\ \rho \mathrm{dx}\Delta u &= \tau \mathrm{dt} \end{aligned} \tag{65}$$

where `Vbound` is the streamwise velocity in the boundary point, `tauls` the streamwise wall shear stress, `dt` the time step and `dr` the spatial step in wall normal/lateral direction.

Zijwandenalternatief Implementation of the two-layer wall model of Balaras, Benocci and Piomelli. This wall model solves a seperate equation on an embedded grid. This method is described in chapter 2 of the PhD thesis of Wim van Balen and not further discussed here. Calls subroutine `tridag`.

Bodem Basically the same as for zijwanden, but applied to the bottom. The choice for the type of bottom (smooth or rough) can be arranged by the variable optie. Smooth is denoted by optie = 1 and rough by optie = 2. The roughness height ks is represented by the variable ruwh and is given in meters.

Bodemupdate Same as `zijwandenupdate`, but applied to the bottom.

Bodemalternatief Same as zijwandenalternatief, but applied to the bottom. Not discussed here. Calls subroutine `tridag`.

Tridag Thomas algorithm, needed to solve the linear system of equations arising from the two-layer wall model. Not discussed here.

Boumpj Prescribes no-stress and no-penetration conditions at the walls. Remark, that if a wall function is applied, the solid wall has to be prescribed as a free-slip boundary. The wall function itself (subroutine `zijwanden`, `bodem` or the IBM) provides friction. Calls subroutines `excju`, `excjv` and `excjw` to add noise in the model?

Bouprj Analogue of boumpj, but applied to the pressure and other scalar quantities, e.g. the sub-grid viscosity. Calls subroutine `excjp` to add noise in the model?

Momsource In case periodic boundary conditions are applied, this subroutine provides the driving force of the flow. This subroutine basically adds the contribution `vmomsource` to the predicted velocity field, which is denoted as `dVdt`. A certain amount of momentum is added in order to obtain a prescribed mean streamwise velocity, `snelheid`. In the algorithm this looks like:

$$\begin{aligned} \mathrm{dVdt}(i,j,k) &= \mathrm{dVdt}(i,j,k) + \mathrm{vmomsource} \\ \mathrm{vmomsource} &= \frac{\mathrm{dt}\cdot \mathrm{cf}\cdot \mathrm{snelheid}^2}{\mathrm{height}} \cdot \mathrm{hcv}(i,j,k) \end{aligned} \tag{66}$$

The equation for `vmomsource` can be easily derived from Newton's law. The below factor can be added to the equation to account for the potential vortex distribution.

$$\mathrm{abs}(\mathrm{krp}(i,j)) \cdot (\mathrm{Rin} + 0.5\mathrm{width}) \tag{67}$$

Excju Subroutine to add noise to the boundary conditions? Subroutine that prescribes the inflow conditions and outflow conditions for the transverse velocity component u. Two options can be chosen: just random noise (optie = 1) and a profile read from a certain file (optie = 2). In case of optie = 2, the directory-path has to be specified properly by means of the variable filenameinputu (check the number of characters of this file name). This subroutine has a freaky character because of parallelization affairs. Called by subroutine `boumpj`.

Excjv Analogue of excju, but applied to the streamwise velocity v. In this case, optie = 1 prescribes a 1/7 power law in both the vertical and transverse direction. At the end of the subroutine, outflow conditions are applied. Called by subroutine `boumpj`.

Excjw The same as excju, but applied to the vertical velocity w. Called by subroutine `boumpj`.

Excjp The same as excju, but applied to the pressure Called by subroutine `bouprj`.

STDROUT.F

File containing all the subroutines that deal with the discritizations and time integration.

Adamsb Time integration predictor step of u, v, w. There can be chosen between the use of explicit euler (optie = 1) and Adams-Bashfort (optie = 2). Calls subroutines `diffu`, `advecu`, `presu`, `diffv`, `advecv`, `presv`, `diffw`, `advecw`, `presw`.

$$\begin{aligned} y_*^{n+1} &= y^n + \Delta t \left(\text{cof1} \cdot f^n + \text{cof2} \cdot f^{n-1}\right) \\ y' = f &= -\text{ADV} + \text{DIFF} - \text{PRES} \end{aligned} \tag{68}$$

where `cof1`=1 and `cof2`=0 for explicit euler and `cof1`=1.5 and `cof2`=-0.5 for Adams-Bashfort.

Adamsb2 When the IBM is used, the predictor step is carried out twice. However, f^n shouldn't be calculated again (because this would lead to an incorrect f^n). Thus for the second predictor step `adamsb2` should be used instead of `adamsb`.

Fillps Fills the right hand side of the pressure Poison solver, which is the divergence of the predicted velocity field.

$$\begin{aligned} \text{pdak}(i,j,k) =& \frac{\text{dUdt}(i,j,k) - \text{dUdt}(i-1,j,k)}{\text{dr}(i)\text{dt}} + \text{krp}(i,jv)\frac{\text{dUdt}(i,j,k) + \text{dUdt}(i-1,j,k)}{2\text{dt}} \\ &+ \frac{\text{dVdt}(i,j,k) - \text{dVdt}(i,j-1,k)}{\text{dyp}(i,jv)\text{dt}} + \frac{\text{dWdt}(i,j,k) - \text{dWdt}(i,j,k-1)}{\text{dz}(k)\text{dt}} \end{aligned} \tag{69}$$

Correc Correction step. Adjusts the velocities according to the pressure field `pdak(i,j,k)` as obtained by the pressure solver. For the streamwise direction this is:

$$\text{dVdt}(i,j,k) = \text{dVdt}(i,j,k) - \frac{\text{pdak}(i,j+1,k) - \text{pdak}(i,j,k)}{\text{dyp}(i,jv)}\text{dt} \tag{70}$$

Update Update the velocities (`dVdt`→`V`), pressure (`p+pdak`→`p`) and advection, diffusion and pressure terms of the momentum equation (`RVold`→`RVnew`) for the next time step.

Diffu Calculates the diffusion part of the lateral momentum equation.

Diffv The same as `diffu`, but applied to the streamwise velocity.

Diffw The same as `diffu`, but applied to the vertical velocity.

Advecu Calculates the advection part of the lateral momentum equation. In `advecu` the '`putout`' is first reset to zero. When calling subsequently `advecu`, `diffu` and `presu`, `advecu` should be called first.

Advecv The same as `advecu`, but applied to the streamwise velocity.

Advecw The same as `advecu`, but applied to the vertical velocity.

Presu Calculates the pressure part (except the additional pressure as calculated by the corrector step) of the lateral momentum equation.

Presv The same as `presu`, but applied to the streamwise velocity.

Presw The same as `presu`, but applied to the vertical velocity.

Smagor This subroutine assesses the static Smagorinsky model. Calls subroutine `fluidvisc` to include the IBM-method for the boundaries. The sub-grid scale viscosity ν_{sgs}, needed for the modeling of the sub-grid scale stress tensor, is modeled using Smagorinsky's Model following:

$$\nu_{sgs} = \underbrace{C_s^2 \Delta^2}_{\text{Lmix}^2} \underbrace{\sqrt{2 S_{ij} S_{ij}}}_{\sqrt{\text{shear}}} \tag{71}$$

where C_s is Smagorinsky's Constant and Δ the turbulence resolution length-scale (in the subtle nomenclature of Pope [2004]), defined as $\Delta = (r\Delta\Theta\Delta r\Delta z)^{1/3}$, and $\left|\tilde{S}_{ij}\right|$ the rate of strain tensor based on the resolved velocities. Several values for Smagorinsky's Constant could be used. The value $C_s = 0.1$ though is a fairly standard value. A standard Van Driest damping function is used in order to let $\nu_{sgs} \to 0$ at solid walls. In the subroutine viscosity is defined as:

$$\nu = \nu_{molecular}(i,j) + \nu_{sgs}(i,j,k) * (\text{damping}) \tag{72}$$

where: $\nu_{molecular}$ is the molecular viscosity ($\propto 1/\text{Re}$), damping(i,k) the Van Driest damping (which basically takes care that C_s goes to zero at the flow boundary) and $\nu_{sgs}(i,j,k)$ the (turbulent) sub-grid viscosity ($= \text{Lmix}^2\sqrt{\text{shear}}$). Since the turbulence in LES is isotropic on subgrid scale, the variable `shear` is obtained using all normal and shear stresses. Note further that to prevent a negative viscosity: $\nu_{sgs} \geq -Rei$.

Dynsubmod The dynamic Smagorinsky Model. Can be used instead of subroutine `smagor`. Calls subroutine `bouprj`. Not discussed here. Improvement compared to the use of the static Smagorinsky Model small. See chapter 4 of the PhD thesis of Wim van Balen.

IBM.F

File containing all the subroutines that deal with the Immersed Boundary Method.

Ghostcells Defines which velocity nodes are in the fluid domain (hcu = 1) and which are in the solid domain (hcu = 0) and defines the ghostcells (hhcu = 1), which are the velocity nodes in the fluid domain that have at least one neighbor in the solid area. Calls subroutines `bouprj`, `bottomU`, `bottomV`, `bottomW` and `bottomC`. Important output out from this subroutine for U-velocity points are the matrices `hcu`, `hhcu` and `acu`. Idem for v, w and c points. In matrix `acu` all the u-ghostpoints are listed with in the first three columns the i, j and k location of the point and in the fourth column a number which indicates the possition of the ghostpoint relative to the boundary (in subroutine `fluidcell` this boundary position will be used in combination with vector `gc`).

BottomU This subroutine determines for each u velocity node the local spatial partial derivatives of the bottom geometry. This is needed later on in subroutines `ghostcells`, `fluidcell` and `fluidvisc`. The output of this subroutine is `fff` in [m] (the bottom elevation in the fluidpoint U), non-dimensional `fax` (the bottom gradient in the fluidpoint U in x direction) and

non-dimensional `fay` (the bottom gradient in the fluidpoint U in y direction).

$$\begin{aligned} \text{fff} &= \frac{\text{bottom}(i+1,jv) + \text{bottom}(i+1,jv)}{2} \\ \text{fax} &= \frac{\text{bottom}(i+1,jv) - \text{bottom}(i+1,jv)}{dr(i)} \\ \text{fay} &= \frac{\frac{\text{bottom}(i+1,jv+1)+\text{bottom}(i,jv+1)}{2} - \frac{\text{bottom}(i+1,jv-1)+\text{bottom}(i,jv-1)}{2}}{2\text{dyp}(i,jv)} \end{aligned} \tag{73}$$

BottomV The same as subroutine `bottumU`, but for each v velocity node.

BottomW The same as subroutine `bottumU`, but for each w velocity node.

BottomC The same as subroutine `bottumU`, but for each concentration node.

Wallpredictor This subroutine is part of the Balaras algorithm on which the Immersed Boundary Method is based: you do the predictor step twice, after the first predictor step, you compute the predicted velocities in the boundary points specially by means of the Immersed Boundary Method. This subroutine updates the computed velocities in the velocity ghost points (`dUdt`(i,j,k) → `U`(i,j,k)).

Fluidcell (Major part of this description is copied from Van Balen [2008].) This subroutine is the core of the Immersed Boundary Method: it computes the velocities in the boundary points. With the variable optie, one can choose the wall function for smooth walls (optie = 1) or for rough walls (optie = 2). Once again, the roughness height ks is represented by the variable ruwh. This subroutine makes use of several rotation subroutines listed at the bottom of the ibm.f file. Calls subroutine `bottomU`, `matinvb33`, `roteerZ`, `roteer3dheen`, `matinv44`, `roteer3dterug`.

1. Locate all the fluid points that have at least one direct neighbor in the solid. An example is point G in figure 41. These points, denoted as `G` in the subroutine, will henceforth be referred to as boundary points and are defined by subroutine `ghostcells` in the matrix `acu` for the u velocity points.

2. Find point `A`, which is defined as the point on the embedded boundary, such that the distance AG is minimal, i.e. the line AG is perpendicular to the wall. The location of point `G` relative to the boundary is defined in `acu(n,4)`. With the help of dummy boundary point `J` and subroutine `matinvb33`, point `A` is found.

3. Find appropriate surrounding fluid points, that are not boundary points at the same time. These points are denoted `B`, `C` and `D` and `E`. Also determine the total velocity vector at these points, which is necessary due to the staggered character of the grid.

4. Rotate the reference system locally, such that the tangent line at the embedded boundary and the line AG become the new principal axes of the local reference system. The new axes are now denoted as xt, the tangent direction, and xn, the normal direction.

5. Define an image point I, with coordinates xIt and xI n defined as

6. Find the velocity components in tangent and normal direction at point I by means of linear interpolation, based on the polynomial u = a1 + a2x + a3y. At this point, linear interpolation is not inadequate since all the points I, B, C and D are located relatively far from the wall and relatively close to each other.

7. Use the interpolated tangent velocity at point I and the zero-velocity at point A as boundary conditions for the determination of uô from equation 2.10. Use a linear velocity profile for the normal velocity, from zero at point A to the interpolated velocity at point I.

8. Determine, from the solution from the previous step, the velocity components at point G.

9. Translate the calculated velocity vector backwards to the original reference system and use the velocity at point G for the calculation of the body force fi in equation 3.2. Notice here, that, due to the staggered character of the grid, only the horizontal component of the velocity at point G is needed for the calculation of the body force fi.

Boundaryshearstressupdate Subroutine that needs to be used when the IBM and subroutine `bodem` are used simultaneously.

Fluidvisc Analogue of subroutine `fluicell`, but applied to the sub-grid viscosity. Calls subroutine `bottomC`, `roteerZ`, `roteer3dheen`, `matinv44`, `roteer3dterug`. Called by `smagor`.

Matinvb33 Matrix opperations contribution in obtaining the closest point on the boundary (`A`) from ghostcell `G`. This subroutine uses the distance of ghostcell `G` to the dummy boundary point `J` and the bottom slope and direction of the bottom slope in point `J`. Used by subroutine `fluidcell`.

Matinv44 Used to find velocity components in image point I in step 6 of subroutine `fluidcell`.

Roteer3dheen, Roteer3dterug, RoteerX, RoteerY and RoteerZ Subroutines to rotate the grid. Used in step 4 and 9 in subroutine `fluidcell` and in subroutine `fluidvisc`.

SOLVER.F

Pressure Poisson solvers, part of the corrector step. Solves the 'additional pressure', `pdak`. The input `pdak` is the right hand side of the pressure equation, whereas the output `pdak` is the additional pressure?

Solmpj This subroutine executes an FFT in two horizontal direction and applies the Thomas algorithm in the vertical direction. This subroutine can only be used for straight flows on regular grids. With this routine, also straight channel flow with periodic boundaries applied in the two bottom-parallel directions can be simulated. Calls several subroutines from `FFTpack.f`, `subr.f` and `parsub.f`.

Cycredjk This subroutine executes an FFT in the lateral direction and applies a so-called generalized cyclic reduction method in the streamwise-vertical plane? This method can be applied to straight flows and curved axisymmetric flow on regular grids? Calls several subroutines from `FFTpack.f`, `subr.f` and `parsub.f`.

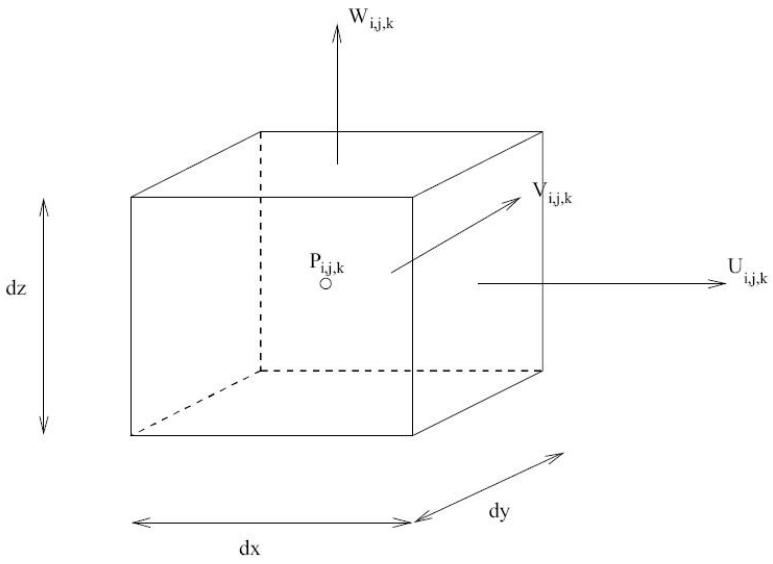

Figure 40: Relevant staggered grid (`Boersma`).

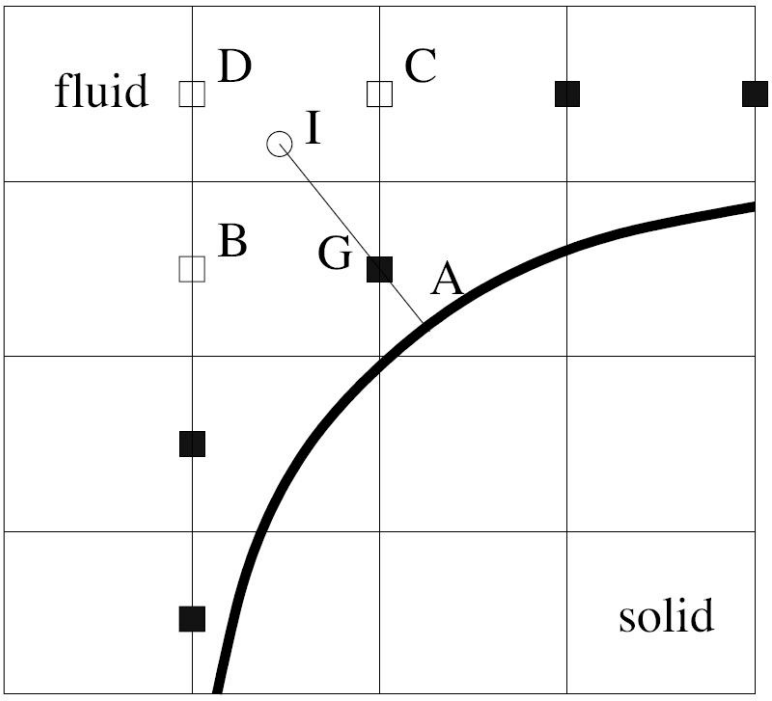

Figure 41: (`Van Balen [2008]`).

Solmpjalt This method applies the FFT in the two directions of the cross section plane and uses the Thomas algorithm for the third, streamwise direction. This method is applicable to flows that have both curved and straight parts, as long as the curvature of the curved part is relatively mild. In Chapter 2 of the PhD thesis of Wim van Balen, it is explained that for such a case, the second radial terms can be kept out of consideration at the cost of losing some mass. The big advantage of this method is, however, that it is way faster compared to the bicgstab routine. Calls several subroutines from `FFTpack.f`, `subr.f` and `parsub.f`.

Bigcstab This subroutine executes an FFT in the vertical direction and applies the BiCGSTAB method (with ILU preconditioning) to the directions in the horizontal plane. This method is applicable to all kinds of flows: meandering, hybrid curved-straight, etc. as long as the grid in vertical direction is regular. Calls several subroutines from `FFTpack.f`, `subr.f` and `parsub.f`.

Cycredik This subroutine executes an FFT in the streamwise direction and applies a so-called generalized cyclic reduction method in the cross sectional plane. This method can be applied to straight flows and curved axisymmetric flow on regular grids. Calls several subroutines from `FFTpack.f`, `subr.f` and `parsub.f`.

INOUT.F

Includes subroutines that write data for further analysis. Different other output subroutines exist.

Datdumgeometry Writes 'geometry' data files in directory `data`. Data consist of `hcu`, `hcv` and `hcw`. Only used in case of complex boundary (thus use of IBM method). Needs to be called after subroutine `ghostcells` is called.

Datdum Writes data files in directory `data`. Data consists at the moment of `u`, `v`, `w`, `pdak`, `ekm` and `divergentie` but this can be changed or extended easely.

Startveld() Writes (`startveld(1)`) or reads (`startveld(0)`) flow data files (`u`, `v` and `w`) in/from directory `init`. Used for 'hot-start'.

Statistiek Writes data files in directory `uitvoer`. Data consst of velocities (`u`, `v` and `w`), Reynold stresses (`uu`, `uv`, `uw`, `vv`, `vw`, `ww`), turbulent viscosity (`ekm`) and boundary shear stresses (`taubs`, `taubn`, `tauls`, `taulz`, `taurs` and `taurz`). Velocities are interpolated in the pressure points.

CHECKS.F

Includes the control subroutines that asses the stability (time step, `chkdt`) and mass conservation (divergence of the flow field, `chkdiv`). Calls subroutines `bouprj` and `MPI ALLREDUCE`. Output in file 'output'.

FFTPACK.F

Includes standard routines for pressure Poisson solver. Taken from the website `www.netlib.org`. Used by the pressure Poisson solvers from `solver.f`.

SUBR.F

Includes standard routines for pressure Poisson solver. Alternative for fftpack.f. Used by the pressure Poisson solvers from `solver.f`.

PARSUB.F

Technical fortran file on parallelization issues. Contains subroutines `barrou`, `PARINIT`, `PARSTRT`, `PAREND`, `ALL ALL j` and `ALL ALL j var`.

Technical files

MAKEFILE

Contains name of specific simulation. Needs to be changed? `EXE`=*'name'* at line 5.

Parameter files

COMMON.TXT

This file contains the global declaration of variables.

INPUT

This files contains the input parameters, which are listed below.

Tijdstappen The desired number of time steps.

Tstatbegin Indicates the time step from which statistical averaging takes place.

Tussenstap Time-interval of taking samples for the statical averaging.

Turbulencemodel Indicates whether LES is used (0) or RANS (1).

Concentration Indicates whether a scalar tracer is present (0 = off, 1 = on). Define a source yourself. Recall that the treatment of concentration is not well established for the cases `CaseTA` and `CaseTS`.

Smagorinsky The values of the Smagorinsky Constant, Cs. Standardly taken as 0.1. Notice that also the dynamic Smagorinsky Model is incorporated in the model: see subroutine `dynsubmodel` at the bottom of `stdrout.f`. In that case, also the prescription of the sub-grid viscosity `ekm` at rule 759 (in case of `CaseRA`) should be uncommented.

Insleng The total length of the straight parts of the flow together (in [m]). Redefined in subroutine `standard`?

Rin The curvature radius at the convex sidewall (in [m]).

Width The width of the flume (in [m]).

Height The water depth (in [m]).

Fleng The total angular length of the curved parts of the flow together, in degrees. Redefined in subroutine `standard`?

snelheid Some prescribed velocity. Relevant for the initial conditions and inflow conditions (in [m/s]). Used in the subroutine `momsource`.

cf The friction factor, used in the subroutine `momsource`. (= ccff).

iper Periodicity in transverse direction (0 = non-periodic, 1 = periodic).

jper Periodicity in streamwise direction (0 = non-periodic, 1 = periodic).

ruwl Boundary roughness of the left bank (= -1 if smooth).

ruwb Boundary roughness of the bed (= -1 if smooth).

ruwr Boundary roughness of the right bank (= -1 if smooth).

PARAM.TXT

In this file the grid parameters are defined. The file contains the number of processors `numpes` and the number of grid cells in each direction: `imax` in transverse direction, `jtot` in streamwise direction and `ktot` in vertical direction. If, for instance, 4 processors are used (i.e. `numpes` = 4) and 200 grid cells in streamwise direction are used (i.e. `jtot` = 200), then the numbering of the cells goes from 1 to `jmax` at each processor (note: `jmax` = `jsen` = `jtot`/`numpes` should be a natural number). To enable the prescription of boundary conditions, the entire array ranges from 0 to `j1`, with `j1` = `jmax` + 1 (see figure 42). The same holds for the two other directions `i` and `k`.

MPI_CONS.TXT

Contains the parameters for parallelization.

BOTTOM.TXT

Contains the bottom elevation for every pressure grid point.

Additional Directories

The model is designed to make use of four additional directories. `Data` (to store instantaneous data), `init` (to store initial conditions), `invoer` (to store profiles of the streamwise, transverse and vertical velocities as inflow boundary conditions. Inflow data are taken from this folder), `uitvoer` (to store data after statistical treatment).

Variables

All variables in the algorithm are listed and discussed here.

ioutp Defined in subroutine `standard` as 6.

istep Indicator of the subsequent time steps (integer). Used for the loop in `main.f`. Reaches from 0 to `nstep`. Set to 0 in subroutine `standard`.

nstep The desired number of time steps. Defined in `input`.

istart Used in `parsub.f` (subroutine `ALL ALL j var`).

iper,jper Periodicity in transverse and streamwise direction (0 = non-periodic, 1 = periodic). Defined in `input`.

tstep Time-interval of taking samples for the statical averaging. Defined in `input`.

tstatb Indicates the time step from which statistical averaging takes place. Defined in `input`.

turb Indicates whether LES is used (0) or RANS (1). Defined in `input`.

conon Indicates whether a scalar tracer is present (0 = off, 1 = on). Defined in `input`.

NN1,NN2,NN3,NN4,NN5,NN6,NN7 Only in non-axisymmetric?

Re Reynolds number. Defined in subroutine `standard` as 10^6.

Rei Inverse of the Reynolds number ($\frac{1}{\mathrm{Re}} \propto \nu_{molecular}$). Defined in subroutine `standard`.

pi π, defined in subroutine `standard`.

Cs The values of the Smagorinsky Constant, Cs. Defined in `input`, standardly taken as 0.1.

Courant Courant number? Defined (as 0.30) and used in subroutine `chkdt`.

snelheid The cross sectional averaged streamwise velocity. Relevant for the initial conditions and inflow conditions. Defined in `input` and used in the subroutine `momsource`. In [m/s].

tijdu,tijdv,tijdw Defined in subroutine `standard` as 1.5.

Influ,Inflv,Inflw Used in subroutines `excju`, `excjv` and `excjw`.

ruwl,ruwb,ruwr Left boundary, bed and right boundary roughness (if rough it represents k_s in [m?], if smooth it is set to -1). Defined in `input`.

Ru,Rp Radius of curvature of the pressure points (`Rp`) and u-velocity points (`Ru`)? Note that the radius of curvature of the v- and w-velocity points are equal to the curvature of the pressure points.

dr,xRu,xRp Lateral position of the pressure (`xRp`) and u-velocity (`xRu`) grid points and the lateral mesh size (`dr`). Note that the lateral position of the v- and w-velocity points are equal to the lateral position of the pressure point.

Lmix Mixing length scale of the Smagorinsky Model ($= Cs \cdot \Delta$).

dyu,dyp Streamwise mesh size between the pressure points (`dyp`) and u-velocity points (`dyu`). Note that the mesh size between the subsequent v- and w-velocity points are equal to the mesh size between the pressure points.

kru,krp Curvature of the pressure points (`krp`=1/`Rp`) and u-velocity points (`kru`). Note that the curvature of the v- and w-velocity points are equal to the curvature of the pressure points.

zp,zw,dz Vertical position of the pressure (`zp`) and w-velocity (`zw`) grid points and the vertical mesh size (`dz`). Note that the vertical position of the u- and v-velocity points are equal to the lateral position of the pressure point.

dyin,dphi Scalars, `dyin` is streamwise grid size in the straight part of the domain (dyin = $Insleng/(jtot - ii)$) and `dphi` is the grid rotation between two grid points in the curved domain (dphi = $Fleng/ii$). Together with the radius of curvature, `dphi` is also a measure for the streamwise grid size.

yp,yu,yv,xp,xu,xv Matrix containing the x and y coordinates of the grid points. Used in case of IBM method. Defined in subroutine `mkgrid`.

phiu,phiv,phip 2d-Matrices containing the orientation of the grid points. Used in case of IBM method in subroutine `fluidcell` for rotational purposes. Defined in subroutine `mkgrid`.

dt Time step, in [s]. Defined in ...

time Time, in [s] (each time step `istep`: time = time + dt). Used in `main.f`. Set to 0 in subroutine `standard` and in `main.f`.

U,V,W Velocities after the corrector step. In [m/s].

kr Dummy variable? Sometimes `kr` = `krom`, sometimes `kr` = abs(`krom`).

krom Gives the direction of the bend. Right 'turn' = -1; left 'turn' = 1; straight = 0.

ccff/cf The (dimensionless) friction factor, used in the subroutine `momsource`. Defined in `input`.

gemsnelheid Dummy variable, calculated average velocity in [m/s]. Used in subroutine `momsource` and defined in subroutine `chkdiv`.

taubs,taubn,tauls,taulz,taurs,taurz Boundary shear stresses. Defined by subroutines `zijwanden`, `bodem` or `fluidcell`? In [m^2/s^2] ($= \tau/\rho$).

derive

dUdt,dVdt,dWdt Dummy velocities. After the predictor step, before the corrector step. In [m/s].

RUnew,RUold,RVnew,RVold,RWnew,RWold Terms in the momentum equation on time n (RUnew) and time $n-1$ (RUold). Defined in `diffu`, `advecu` and `presu`. In subroutine `update` `RVold` becomes `RVnew`. In [m/s^2].

divergentie Used in subroutine `chkdiv`.

tke 'Turbulent Kinetic Energy'. Only used for RANS.

tep 'Epsilon', dissipation. Only used for RANS.

sigmak,sigmae,c1e,c2e,copp,cyl,cyw,cmu Magnitude defined in subroutine `standard`. Only used for RANS.

Rkenew,Rkeold,Repnew,Repold Terms in the 'turbulent kinetic energy'/'epsilon' equation on time n (Rkenew) and time $n-1$ (Rkeold). Defined in `keps.f`. Only used for RANS.

ekm Eddy viscosity. Defined by subroutine `smagor`. In ..

concnew,concold Terms in the 'tracer' equation on time n (concnew) and time $n-1$ (concold). Defined in `keps.f`.

conc Concentration of tracer.

Cdyn Dynamic Smagorinsky Constant. Defined by `dynsubmod`.

numean In `satistiek`. Output values for turbulent viscosity (from `ekm`). In ..

work,save Reduce work space for non-used CFP solver? Defined in `param.txt`.

p Pressure. In [m^2/s^2] ($= p/\rho$)?

pdak 'Additional' pressure. Follows from corrector step. Defined by pressure Poisson solver. Added to the pressure in subroutine `update`. In [s^{-2}] (according to `fillps`) or [m^2/s^2] ($= p/\rho$, according to `correc`)? Is the variable `pdak` after the pressure Poisson solver not the same variable `pdak` before?

opl Dummy variable in `solver.f`. Only in non-axisymmetric/ old version.

Insleng The total length of the straight parts of the flow together (in [m]). Defined in `input` but redefined in subroutine `standard`.

Height The water depth (in [m]). Defined in `input`.

Width The width of the flume (in [m]). Defined in `input`.

Fleng The total angular length of the curved parts of the flow together, in degrees. Defined in `input` but redefined in subroutine `standard`.

Rin The curvature radius at the convex sidewall (in [m]). Defined in `input`.

ampl,pery Only used in `ibm22082011.f`!

pert,tb Used in case of IBM method in subroutines `bottomgeometry` and `movingwall`. `pert` is set to 4; `tb` is $\sin(\frac{2\pi \text{time}}{\text{pert}})$.

umean,vmean,wmean In `satistiek`. Output values for Reynolds averaged velocities. In [m/s].

uvmean,uwmean,vwmean,uumean,vvmean,wwmean In `satistiek`. Output values for Reynolds stresses. Uses interpolated values. In $[m^2/s^2]$?

emean,pmean In `satistiek`. `emean` are the output values for turbulent viscosity (from `ekm`), in newer versions called `numean`. `pmean` are the output values for `pdak`, in newer versions omitted.

taubsmean,taubnmean,taulsmean,taulzmean,taursmean,taurzmean In `satistiek`. Output values for boundary shear stresses. In $[m^2/s^2]$ $(= \tau/\rho)$.

pad Path. Defined in subroutine `standard`. Number of characters defined in `common.txt`.

hcu,hcv,hcw,hcc Matrix which denotes whether an u, v, w or c grid point is in the fluid (=1) or solid (=0) domain. Defined in subroutine `ghostcells`.

bottom Location of the channel bed. Defined in `bottom.txt` or by a function in subroutine `ghostcells`.

hhcu,hhcv,hhcw,hhcc Matrix which denotes whether an u, v, w or c grid point is a ghost point (=1). Defined in subroutine `ghostcells`.

acu,acv,acw,acc Matrix listing the ghost points by means of their grid position (`acu`(:,1:3)). Also provides information about the location of the boundary with respect to the ghost cell (`acu`(:,4)) and information about the location of the neighbouring grid points in the fluid domain (`acu`(:,5:16)). Defined in subroutines `ghostcells` and `findinterpolationpoints`.

abu,abv,abw,abc Used in the IBM method in subroutine `insideboundary`/`concentrationboundary`, should containt grid point locations of 'type of ghost cells' but matrix is not defined anywhere?

ni,nj,nk,nc Number of ghost cells (listed in `acu`, `acv`, `acw` and `acc`). Used in IBM method.

nib,njb,nkb,ncb Number of ghost cells (listed in `abu`, `abv`, `abw` and `abc`). Used in IBM method.

myid Refers to the parrallized part (is 0, 1, 2 or 3 if 4 numpes are used; see figure 42).

iv,jv,kv 'Reel coordinates, introduced because of parallelization issues (iv $= i + myid * jsen$; see figure 42).

Ubaverl,Vbaverl,Wbaverl,Ubaverh,Vbaverh,Wbaverh Often interpolated velocities in [m/s]. Used in subroutine `smagor`, `zijwanden` and `bodem`.

Vrell,Vrelh Velocity vector length (ex. $\sqrt{(}U^2 + V^2)$ in the cell clostest to the left (Vrell) and right (Vrelh) wall in [m/s]. Used in subroutine `smagor`, `zijwanden` and `bodem`.

ust u_* In the beginning of the iteration loops, where u_* is determined, $u_* = 0.1$. In [m/s]. Used in step 7 and 8 of subroutine `fluidcell`. Also defined in subroutines `fluidvisc`, `fluidmove`, `insideboundary` and `concentrationboundary` but not used.

Ustl,Usth u_* at the left wall (Ustl) and at the right wall (Usth) in [m/s]. In the beginning of the iteration loops, where u_* is determined, $u_* = 0.1$. Used in subroutines `zijwanden`, `bodem` and `smagor`.

Ustlog,Ustsafe Sort of dimensionless wall coordinate ($=u_* y \mathrm{Re} \cdot \mathrm{Cmaal} = 9 \cdot y^+$). Ustsafe is the minimum value of Ustlog (= 50). Used in subroutine `smagor` to define `Ustl` (u_*) and finally the Van Driest damping. Apparently $\bar{u}(y^+) = \frac{u_*}{\kappa} \log_e(9 \cdot y^+) = u_* \left(\frac{1}{\kappa} \log_e(y^+) + 5.5\right)$, which represents the velocity distribution of the turbulent inner layer.

kappa Von Karman constant (= 0.4). Used in subroutine `smagor`.

Cmaal (= 9) Helps to describe the turbulent inner layer in a strange way ($\frac{1}{\kappa} \log_e(\mathrm{Cmaal}) = 5.5$). Used in subroutine `smagor` for the Van Driest damping function.

Vbound,Ubound,Wbound Velocity in the boundary cell in [m/s]. Used in subroutine `boumpj`

ca1,ca2,cb1,cb2 Constants for the (smooth) wall functions. For the rough wall function it is implemented as numbers in the equation directly. Used in subroutines `zijwanden` and `bodem`.

dVtdrl,dVtdrh,dVdrl,dVdrh,dWdrl,dWdrh,dUdrl,dUdrh Boundary shear stress (divided by density in [m^2/s^2]) without sign. Used in subroutines `zijwanden` and `bodem`.

URe Dimensionless wall coordinate y^+ ($=u_* y / \nu_{molecular}$). Used for choosing in which layer of the smooth wall functions the velocity point is located. Used in subroutines `zijwanden` and `bodem`.

ruwh Boundary roughness, is defined or is equal to `ruwl`, `ruwb` or `ruwr`. Used in subroutines `zijwanden` and `bodem`.

nl Dummy variable, used for iteration loops.

optie (= 1 or 0) Used to define an option. For example between the two options of the initial velocity distribution.

ii Number of grid points in curved domain (= sum(abs(krom(1:imax,1:jtot)))/imax). Used in `boundar.f`. `jtot-ii` gives the number of grid points in the straight domain. In some of the technical files `ii` is also used as variable to denote something else.

cof1, cof2 Parameters defining time integration method (Adam-Bashfort or Euler forward).

im,ip,jm,jp,km,kp im = i - 1, kp = k + 1 etc.

eppo,epmo,epop,epom e.a. Interpolated turbulent viscosity, `ekm`, in subroutine `diffu`.

fff,fay,fax Output of subroutine `bottomU`: `fff` in [m] is the bottom elevation in the fluidpoint U, non-dimensional `fax` is the bottom gradient in the fluidpoint U in x direction and non-dimensional `fay` is the bottom gradient in the fluidpoint U in y direction.

-G,-A,-B,-C,-D,-E,-F,-I,-J Points defined in the IBM-method. Where (x-,y-,z-) denote the location; (u-,v-,w-) the velocities; (ph-) the orientation in the horizontal plane; and (i-,j-,k-) the position in the grid.

snelU,snelV,snelW 3d-Matrices containing the velocities in the fluid domain. Used in the IBM-method.

phx,phy Slope of the bottom in x- and y-direction in point `J` (in subroutine `fluidcell`), `G` (in subroutines `fluidvisc` and `fluidmove`) or `X` (in subroutines `insideboundary` and `concentrationboundary`). Needed in the subroutines which rotate the coordinate system.

putout Often used for subroutine.

fG,fyG,fxG,fJ,fyJ,fxJ `fff`, `fay` and `fax` applied to point `G` and `J`. Used in the IBM-method.

vecI,vecG Velocity vector in ghostcell (`vecG`) and image cell `vecI`($=\sqrt{uI^2 + vI^2}$). Used in subroutine `fluidcell`.

dzp,dzm,drp e.a. dzp=zp(kp)-zp(k); dzm=zp(k)-zp(km); drp=xRp(ip)-xRp(i). In [m]?

zplus Wall coordinate, y^+. Used in subroutine `fluidcell`.

kromming Mean `kru`. Used in the advection subroutines (`advecu`).

sx,sy,sz In ibm.f. And excju.

t In ibm.f.

A(),B(),rhs(),detB,pp,qq In ibm.f.

variables in excju, dynsubmod Not assessed yet.

bvxjp,bvxjm,bwxkp,bwxkm e.a. Factors to give a relative importance to the different contributions?? Hence (= 1). Used in subroutines `diffu` and `advecu`.

Remark

Note that this manual is meant to help the modeler understand the algorithm. The manual is however far from complete and should be extended in the future.

References and Other Useful Links

1. Brief description of the DNS/LES/RANS flow model. Written by Wim van Balen. Parts of this manual are copied from his description.
2. "Curved open-channel flows, A numerical study" `Van Balen [2010]`. Parts of this manual are copied from here.
3. "Modeling complex boundaries using an external force field on fixed cartesian grids in large-eddy simulations." `Balaras [2004]`. Proposes the in the model used IBM.
4. A document by Boersma. Here the discritization as they are used in the model are listed.
5. Master thesis of Anton van der Meer. As addition to this thesis, this manual is written.
6. "Modelling and parameterizing the hydro- and morphodynamics of curved open channels" `Ottevanger [2013]`. Used and adapted the model.

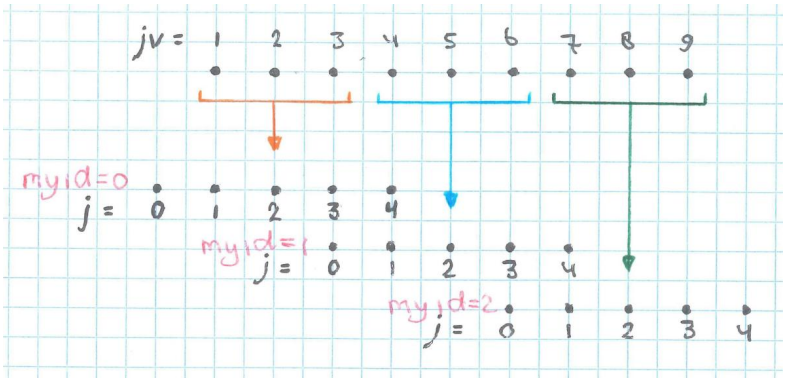

Figure 42: Example to clearify the used grid parameters. Consider that the fluiddomain in j-direction consists of nine grid cells (thus `jtot` = 9). Running the model on three numpes (`numpes` = 3), leads to `jmax` cq. `jsen` = 3 and `j1` = 4. The three parallized parts are denoted by `myid` = 0, 1 and 2. The original coordinates, `jv`, can be easely regained (`jv` = j + `myid` * `jsen`).

E Calculation Overview

LES Calculations with FORTRAN

A lot of calculations have been made in order to write this thesis. The majority of them are, however, not used in the report since they contained major errors. An overview of the, in the report referred to, calculations are listed below.

N16_30_00 Calculation based on flume experiment F16_30_00 of `Duarte [2008]`. In contrary the numerical calculation is axisymmetric. Grid size and input parameters can be found in Tables 1, 2 and 3.

N16_30_02 Calculation based on flume experiment F16_30_02 of `Duarte [2008]`. In contrary the numerical calculation is axisymmetric. Grid size and input parameters can be found in Tables 1, 2 and 3.

N16_30_30 Calculation based on flume experiment F16_30_30 of `Duarte [2008]`. In contrary the numerical calculation is axisymmetric. Grid size and input parameters can be found in Tables 1, 2 and 3.

N16_45_00 Calculation based on flume experiment F16_45_00 of `Duarte [2008]`. In contrary the numerical calculation is axisymmetric. Grid size and input parameters can be found in Tables 1, 2 and 3.

N16_45_02 Calculation based on flume experiment F16_45_02 of `Duarte [2008]`. In contrary the numerical calculation is axisymmetric. Grid size and input parameters can be found in Tables 1, 2 and 3.

N16_45_30 Calculation based on flume experiment F16_45_30 of `Duarte [2008]`. In contrary the numerical calculation is axisymmetric. Grid size and input parameters can be found in Tables 1, 2 and 3.

N16_30_02TBS Calculation based on flume experiment F16_30_02 of `Duarte [2008]`. In contrary the numerical calculation is axisymmetric and contains a transverse bed slope. Grid size and input parameters can be found in Tables 1, 2 and 3.

N16_90_02STR Calculation of a straight channel reach with vertical banks from which the turbulent viscosity profile is obtained. Grid sizes equal as in the above mentioned calculations. Referred to from Section 5.3.1. As insufficient care has been taken to the input parameters, the bulk velocity in this calculation is very small.

N16_30_02CRS96 Identical calculation as N16_30_02, but with a coarser grid size. Grid size can be found in Table 9, third row. Referred to from Section 5.2.

N16_30_02CRS135 Identical calculation as N16_30_02, but with a coarser grid size. Grid size can be found in Table 9, second row. Referred to from Section 5.2.

HoT1 and HxT1 Calculations with and without the additional itteration loop for the Normal Wall Function Approach. Referred to from and explained in Section 4.2.

MATLAB-Codes

makebottom.m Code that generates the bottom file that is read by subroutine ghostcells of the FORTRAN model. Different versions of the code exist, all making a specific bottom topography.

exWF.m Code generating the hand calculation from Section 5.2.

viscosityprofilegraph.m Code plotting the viscosity profile, as in figure 38 in appendix B.

uitlezendata.m Code that converts the binary output of the FORTRAN model in MATLAB structures and matrices. The code also averages the data along the longitudinal domain, which is useful for axisymmetric cases. Saves the data in [modelname,'.mat'].

BoundaryShearStress.m Plots the boundary shear stress over the length of the perimeter. Used for Figures 19, 20 and 32.

gridTestje.m Code used to generate Figure 33.

MomentumSourceIntegral.m Calculates the cross-sectionally averaged boundary shear stress based on the with the velocity field coinciding outputted boundary shear stresses and based on the momentum source. Saves the data in [modelname,'_TauOut.mat']. Used for Tables 6, 8 and 9.

NormStreamfunction.m Calculates the magnitude of the normalized stream function, as well as the location of the axis of rotation. Used for Table 7 and all figures showing the normalized stream function.

Prandtl1.m Calculates the vorticity source of Prandlt's first type.

Prandtl2.m Calculates the vorticity source of Prandlt's second type.

TurbulenceOutput.m Calculates the turbulent anisotropy and inhomogeneity.

TurbulentViscosities.m Calculates and plots the viscosity profile. The molecular, sub-grid and resolved turbulent viscosity. As in Figure 23.

Vorticity.m Calculates the vorticity.

Plot.... All scripts starting with 'Plot'. Different MATLAB scripts plotting figures based on the saved quantities from the scripts above.

For Mechanism Based Approaches

velocityFieldMBAroughness.m Plot on the basis of equation 88, the velocity field as in figure 44. Used for section F.2.

velocityProfileMBAroughness.m Plot on the basis of equation 88, the velocity profiles from the core of the tube to the boundary of the tube for different locations. Used for section F.2.

F Mechanism Based Approach

Preliminary versions of models made with the intention to get insight in the different mechanisms. In each model is attempted to isolate one mechanisms in order to assess the contribution of it with respect to the boundary shear stress.

F.1 Shear Forces (Channel Geometry)

Research Question

What is the effect of the channel geometry on the distribution of the boundary shear stress? A simplified mathematical model, where secondary currents are neglected, is used to asses this question.

Physical Background

When only taken shear forces, turbulent- and molecular interactions, into account than only the (uniform) forcing, the molecular viscosity (assumed to be an intrinsic property of the fluid), the turbulent properties and the distance from the boundaries determine the streamwise velocity at a certain location ($u = f\left(x, y, z, \nu, F\right)$). The forcing and molecular viscosity are uniform, the flow is considered to be uniform in streamwise direction and the turbulent properties are considered to be a function of the distance from the boundaries. Hence, the streamwise velocity at a certain location is solely a function of the distance from the boundaries ($u = f\left(y, z\right)$).

Mathematical Model: Green's Function

$$\begin{aligned} L\left[u\right] &= f(y,z) \\ u(y,z) &= \int_0^{L_z}\int_0^{L_y} f(y_0,z_0)G(y,y_0,z,z_0)\mathrm{d}y_0\mathrm{d}z_0 \\ L\left[G(y,y_0,z,z_0)\right] &= \delta\left(y-y_0,z-z_0\right) \end{aligned} \tag{74}$$

where: $L\left[u\right]$ is the differential operator, $f(y,z)$ a function, $G(y,y_0,z,z_0)$ the Green's function, (y_0,z_0) a point in the domain and $\delta\left(y-y_0,z-z_0\right)$ the Dirac Delta Function.

2D Laminar Closed Conduit Flow

$$
\begin{aligned}
L\left[u\right] = \frac{\mathrm{d}^2 u}{\mathrm{d}x^2} &= f(x) = a \\
u(0) &= 0 \\
u(L) &= 0 \\
u(x) &= \int_0^L f(x_0) G(x, x_0) \mathrm{d}x_0 \\
G(x, x_0) &= -\frac{x}{L}(L - x_0) \quad \text{for} \quad x < x_0 \\
&= -\frac{x_0}{L}(L - x) \quad \text{for} \quad x > x_0 \\
u(x) &= \int_0^x a\left(-\frac{x_0}{L}(L - x)\right) \mathrm{d}x_0 + \int_x^L a\left(-\frac{x}{L}(L - x_0)\right) \mathrm{d}x_0 \\
&= \left[-\frac{1}{2} a x_0^2 + \frac{1}{2}\frac{a}{L} x x_0^2\right]_0^x + \left[-a x x_0 + \frac{1}{2}\frac{a}{L} x x_0^2\right]_x^L \\
&= \frac{1}{2} a x^2 - \frac{1}{2} a L x
\end{aligned}
\tag{75}
$$

2D Laminar Open Channel Flow

$$
\begin{aligned}
L\left[u\right] = \frac{\mathrm{d}^2 u}{\mathrm{d}x^2} &= f(x) = a \\
u(0) &= 0 \\
u'(L) &= 0 \Rightarrow u(2L) = 0 \\
u(x) &= \int_0^{2L} f(x_0) G(x, x_0) \mathrm{d}x_0 \\
G(x, x_0) &= -\frac{x}{2L}(2L - x_0) \quad \text{for} \quad x < x_0 \\
&= -\frac{x_0}{2L}(2L - x) \quad \text{for} \quad x > x_0 \\
u(x) &= \int_0^x a\left(-\frac{x_0}{2L}(2L - x)\right) \mathrm{d}x_0 + \int_x^{2L} a\left(-\frac{x}{2L}(2L - x_0)\right) \mathrm{d}x_0 \\
&= \left[-\frac{1}{2} a x_0^2 + \frac{1}{2}\frac{a}{2L} x x_0^2\right]_0^x + \left[-a x x_0 + \frac{1}{2}\frac{a}{2L} x x_0^2\right]_x^{2L} \\
&= \frac{1}{2} a x^2 - \frac{1}{2} a (2L) x \\
&= \frac{1}{2} a x^2 - a L x
\end{aligned}
\tag{76}
$$

Rectangular 3D Laminar Open Channel Flow

$$
\begin{aligned}
L[u] = \frac{\mathrm{d}^2 u}{\mathrm{d}x^2} =& f(y,z) = a \\
u(y,0) =& 0 \\
u'(y,L_z) =& 0 \Rightarrow u(y,2L_z) = 0 \\
u(0,z) =& 0 \\
u(L_y,z) =& 0 \\
u(x) =& \int_0^{L_y}\int_0^{2L_z} f(y_0,z_0)G(y,y_0,z,z_0)\mathrm{d}y_0\mathrm{d}z_0 \\
G(y,y_0,z,z_0) =& \frac{y}{L_y}(L_y-y_0)\frac{z}{2L_z}(2L_z-z_0) \quad \text{for} \quad y<y_0;\ z<z_0 \\
=& \frac{y_0}{L_y}(L_y-y)\frac{z}{2L_z}(2L_z-z_0) \quad \text{for} \quad y>y_0;\ z<z_0 \\
=& \frac{y}{L_y}(L_y-y_0)\frac{z_0}{2L_z}(2L_z-z) \quad \text{for} \quad y<y_0;\ z>z_0 \\
=& \frac{y_0}{L_y}(L_y-y)\frac{z_0}{2L_z}(2L_z-z) \quad \text{for} \quad y>y_0;\ z>z_0 \\
u(y,z) =& \int_0^{y}\int_0^{z} a\left(\frac{y_0}{L_y}(L_y-y)\frac{z_0}{2L_z}(2L_z-z)\right)\mathrm{d}y_0\mathrm{d}z_0 \\
&+ \int_y^{L_y}\int_0^{z} a\left(\frac{y}{L_y}(L_y-y_0)\frac{z_0}{2L_z}(2L_z-z)\right)\mathrm{d}y_0\mathrm{d}z_0 \\
&+ \int_0^{y}\int_z^{2L_z} a\left(\frac{y_0}{L_y}(L_y-y)\frac{z}{2L_z}(2L_z-z_0)\right)\mathrm{d}y_0\mathrm{d}z_0 \\
&+ \int_y^{L_y}\int_z^{2L_z} a\left(\frac{y}{L_y}(L_y-y_0)\frac{z}{2L_z}(2L_z-z_0)\right)\mathrm{d}y_0\mathrm{d}z_0 \\
=& \frac{1}{4}ay^2z^2 - \frac{1}{4}ayz^2L_y - \frac{1}{2}ay^2zL_z + \frac{1}{2}ayzL_yL_z \\
\frac{\partial u(y,z)}{\partial z} =& \frac{1}{2}ay^2z - \frac{1}{2}ayzL_y - \frac{1}{2}ay^2L_z + \frac{1}{2}ayL_yL_z
\end{aligned}
\tag{77}
$$

Mapping Functions

Equation 77 calculates the velocity distribution for a rectangular cross section. Using Mapping Functions, the equation can be extended to random cross sections (Equation 78).

$$
u(y_*,z_*) = \frac{1}{4}ay_*^2z_*^2 - \frac{1}{4}ay_*z_*^2L_{y*} - \frac{1}{2}ay_*^2z_*L_{z*} + \frac{1}{2}ay_*z_*L_{y*}L_{z*} \tag{78}
$$

where: $y_* = f(y,z)$, $z_* = f(y,z)$, $L_{y*} = f(z)$ and $L_{z*} = f(y)$. The functions depend on the geometry of the channel. For a trapezoidal channel these functions are defined in Table 16.

	y_*	z_*	L_{y*}	L_{z*}
A	$\frac{y[L_y(z=0)]}{L_y(z)} = \frac{y[L_y(z=0)]}{2sz+[L_y(z=0)]}$	z	$L_y - 2sz$	$L_y + \frac{y_{c1}-y}{s}$; L_y; $L_y + \frac{y-y_{c2}}{s}$

Table 16: Mapping functions for a trapezoidal channel.

F.2 Shear Forces (Differential Roughness)

Research Question

What is the effect of a differential boundary roughness on the distribution of the boundary shear stress in a channel? A simplified hypothetical case is considered analytically to asses this question.

Model Set-Up

A circular tube is considered (Figure 43). The tube is uniform in streamwise direction. The driving force is obtained by placing the tube under a constant angle. Furthermore, no secondary flow is considered (`assumption 1`). The current set-up has a few advantages: (1) The boundary shear stress is uniformly distributed when a uniform boundary roughness is used. The variations in boundary shear stress are thus **only the result of the differential roughness**. No effects of edges or a free surface are present; (2) Since the driving force is known, the average boundary shear stress can be calculated *a priori* with Equation 79.

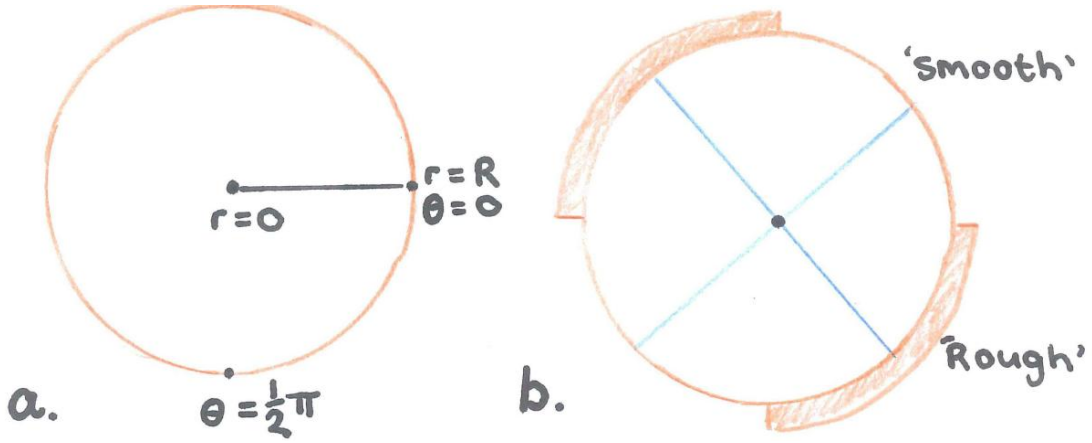

Figure 43: Cross section and used polar coordinate system of the (a) uniform and (b) differential roughened model scenario's.

$$\bar{\tau_b} = \rho g R_h I_e \tag{79}$$

A wall function is assumed to describe the velocity distribution in the tube (`assumption 2`; Equation 80). Therefore, for a given roughness the velocity field and discharge can be obtained (Equation 81 and Table 17). The two different roughnesses used (Table 17) are the same as used by `Blanckaert et al. [2010]`.

$$\begin{aligned} u(r) &= \frac{u_*}{\kappa} \log_e \left(\frac{R-r}{y_0} \right) \\ &= \frac{\sqrt{\tau_b/\rho}}{\kappa} \log_e \left(\frac{R-r}{y_0} \right) \end{aligned} \tag{80}$$

	R_h $[m]$	I_e $[-]$	$\bar{\tau}_b$ $[Pa]$	k_s $[m]$	$u(0)$ $[m/s]$	Q $[m^3/s]$	C_f $[-]$
Roughness 1	0.5	0.001	4.9050	0.002	1.6426	4.3554	0.0026
Roughness 2	0.5	0.001	4.9050	0.030	1.1800	2.9031	0.0057

Table 17: Flow properties for the two selected roughnesses.

$$\begin{aligned}
Q =& -\int_0^{R-y_0} \left(\frac{\sqrt{\tau_b/\rho}}{\kappa} \log_e \left(\frac{R-r}{y_0} \right) 2\pi r \right) dr \\
=& -\left[-\frac{1}{2}\pi \frac{\sqrt{\tau_b/\rho}}{\kappa} \left(-2R^2 \log_e (r-R) + 2r^2 \log_e \left(\frac{R-r}{y_0} \right) - 2Rr - r^2 \right) \right]_0^{R-y_0} \\
=& \frac{1}{2}\pi \frac{\sqrt{\tau_b/\rho}}{\kappa} \left(2R^2 \log_e (-R) - 2R^2 \log_e (-y_0) + 2(R-y_0)^2 \log_e \left(\frac{y_0}{y_0} \right) - 2R(R-y_0) - (R-y_0)^2 \right) \\
=& \frac{1}{2}\pi \frac{\sqrt{\tau_b/\rho}}{\kappa} \left(-2R^2 \log_e \left(\frac{y_0}{R} \right) - 2R(R-y_0) - (R-y_0)^2 \right)
\end{aligned} \tag{81}$$

Implementing on two quarters of the circle a roughness of $k_{s,1} = 0.002$ and the two other quarters $k_{s,2} = 0.03$ (Figure 43), the boundary shear stress is no longer uniform. Because of symmetry, only one quarter of the tube need to be considered. Using Equation 80 the velocity field could be calculated. However, this would lead to large discontinuities in the velocity field. In reality these discontinuities would be smoothened and lead to a different velocity field. The following two assumptions were made to obtain the velocity field in the tube. The total discharge in the tube is equal to the mean of the total discharges for roughness $k_{s,1}$ and roughness $k_{s,2}$ (`assumption 3`). The velocity distribution perpendicular to the border point between the two roughnesses can be described by a function, which is the average of the wall functions of the two roughnesses (`assumption 4`; Equation 83). Assumptions 3 and 4 lead to the following requirements for the velocity distribution equation (Equation 82).

$$\begin{aligned}
u(r,0) &= u_m(r) \\
\left| u\left(r, \pm\frac{1}{4}\pi\right) - u_m(r) \right| &\leq \frac{1}{2}\Delta u \\
\frac{\partial u}{\partial \theta}\left(r, \pm\frac{1}{4}\pi\right) &= 0
\end{aligned} \tag{82}$$

where $(r = R, \theta = 0)$ is the border point between the rough and the smooth boundary, $u_m(r)$ the average function of the wall functions of the two roughnesses (Equation 83) and Δu the difference between the velocity in the 'rough' and 'smooth' case (Equation 84).

$$\begin{aligned}
u_m(r) &= \left(u_1(r) + u_2(r)\right)/2 \\
&= \frac{1}{2}\frac{\sqrt{\tau_b/\rho}}{\kappa} \log_e \left(\frac{(R-r)^2}{y_{0,1} y_{0,2}} \right)
\end{aligned} \tag{83}$$

$$\begin{aligned}\Delta u &= \frac{u_*}{\kappa}\log_e\left(\frac{R-r}{y_{0,1}}\right) - \frac{u_*}{\kappa}\log_e\left(\frac{R-r}{y_{0,2}}\right)\\ &= \frac{u_*}{\kappa}\log_e\left(\frac{y_{0,2}}{y_{0,1}}\right)\\ &= \frac{\sqrt{\tau_b/\rho}}{\kappa}\log_e\left(\frac{y_{0,2}}{y_{0,1}}\right)\end{aligned} \tag{84}$$

For $r \leq R - y_{0,2}$. Given the above requirements an equation for the velocity field is derived (Equation 85).

$$\begin{aligned}u(r,\theta) &= u_m(r) + \frac{\theta\left(|\theta| - \frac{1}{2}\pi\right)}{-\frac{1}{16}\pi^2}\left(\frac{1}{2}\Delta u\right)r^a\\ &= \frac{1}{2}\frac{\sqrt{\tau_b/\rho}}{\kappa}\log_e\left(\frac{(R-r)^2}{y_{0,1}y_{0,2}}\right) + \frac{\theta\left(|\theta| - \frac{1}{2}\pi\right)}{-\frac{1}{16}\pi^2}\left(\frac{1}{2}\frac{\sqrt{\tau_b/\rho}}{\kappa}\log_e\left(\frac{y_{0,2}}{y_{0,1}}\right)\right)r^a\\ &= \frac{1}{2}\frac{\sqrt{\tau_b/\rho}}{\kappa}\left(\log_e\left(\frac{(R-r)^2}{y_{0,1}y_{0,2}}\right) + \frac{\theta\left(|\theta| - \frac{1}{2}\pi\right)}{-\frac{1}{16}\pi^2}\log_e\left(\frac{y_{0,2}}{y_{0,1}}\right)r^a\right)\end{aligned} \tag{85}$$

For $-\frac{1}{4}\pi \leq \theta \leq \frac{1}{4}\pi$ and $0 \leq r \leq (R - y_{0,2})$, in which $(r = R, \theta = 0)$ is the border point between the rough and the smooth boundary. Where a is a measure for the mixing. Knowing the velocity field with the Ray-Isovel Method (`Houjou et al. [1990]`) the boundary shear stress distribution can be obtained. The cross sectional area between two rays is a measure for the local boundary shear stress (Equation 86).

$$\tau_b = \rho g I_e \frac{\int_R^0 dA}{\delta p} \tag{86}$$

where δp is the length of the perimeter between two adjacent rays and $\int_R^0 dA$ the cross sectional area between the adjacent rays.

Intermezzo: Ray-Isovel Method To determine the local boundary shear stress, `Houjou et al. [1990]` presented the ray-isovel method. When the velocity field is known, the isovels can be obtained. Using the *steepest descent method* the rays can be obtained. The direction of a certain ray at a certain point depends on the derivatives to r and θ at that point (Equation 88) according to Equation 87.

$$\vec{d} = \left(\frac{\partial u(\vec{r},\theta)}{\partial r} + \frac{\partial u(\vec{r},\theta)}{\partial \theta}\right) \Big/ \left|\frac{\partial u(\vec{r},\theta)}{\partial r} + \frac{\partial u(\vec{r},\theta)}{\partial \theta}\right| \tag{87}$$

$$\begin{aligned}\frac{\partial u(r,\theta)}{\partial r} &= \frac{1}{2}\frac{\sqrt{\tau_b/\rho}}{\kappa}\left(\frac{-2}{R-r} + a\frac{(\theta)\left(|\theta| - \frac{1}{2}\pi\right)}{-\frac{1}{16}\pi^2}\log_e\left(\frac{y_{0,2}}{y_{0,1}}\right)r^{a-1}\right)\\ \frac{\partial u(r,\theta)}{\partial \theta} &= \frac{1}{2}\frac{\sqrt{\tau_b/\rho}}{\kappa}\left(\frac{1}{-\frac{1}{16}\pi^2}\log_e\left(\frac{y_{0,2}}{y_{0,1}}\right)r^a\left(2\left|\theta\right| - \frac{1}{2}\pi\right)\right)\end{aligned} \tag{88}$$

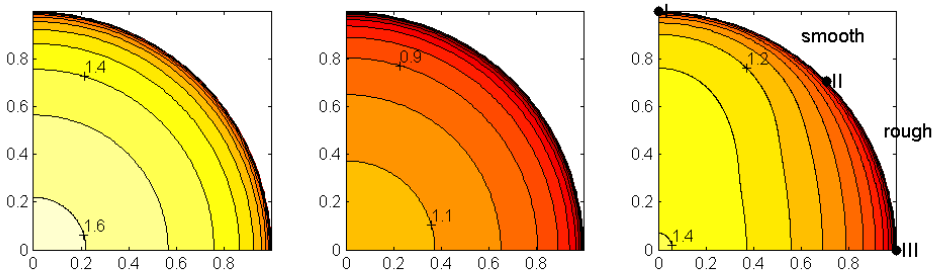

Figure 44: Isovels for a tube with: (a) A roughness $k_{s,1} = 0.002$; (b) A roughness $k_{s,2} = 0.03$; (c) A differential roughness, a combination of both previous roughnesses. Where $k_{s,1} = 0.002$ is called 'smooth', $k_{s,2} = 0.03$ is called 'rough' and the mixing parameter a is defined to be 2.

where the derivatives are derived from Equation 85 and thus $(r = R, \theta = 0)$ is the border point between the rough and the smooth boundary. The integrated area between two rays is a measure for the boundary shear stress at the by the rays confined perimeter according to Equation 86. **End Intermezzo**

Results

Figure 44 shows the isovels for two scenario's with a uniform boundary roughness $k_s = k_{s,1} = 0.002$ and $k_s = k_{s,2} = 0.03$ and a differential boundary roughness which is a combination of the two roughnesses. Point II in Figure 44C represents the border point between the two different boundary roughnesses. For the uniform roughnesses, the bank shear stress distribution is also uniform. Results for the differential boundary roughness the boundary shear stress distribution is given in Figure 45. On the 'rough side', a peak in the bank shear stress arises. This peak decreases and shifts towards the border point for (1) a decreasing difference between the boundary roughnesses and (2) an increasing mixing parameter a. It appears that better mixing leads to a more uniform boundary shear stress distribution.

Discussion

What can be concluded from the results? To what extend do the results represent reality and to what extend do they result from the assumptions made? The (possible) artifacts of the assumptions are treated in... In addition, the results can be compared with data. `Blanckaert et al. [2010]` carried out experiments in trapezoidal channels where the banks had a different roughness than the bed. They found a similar bank shear stress distribution, i.e. with a peak in the bank shear stress distribution close to the border point. The analytical model used in this article demonstrates thus that this configuration of the bank shear stress distribution can be obtained without the inclusion of secondary currents. Moreover, the present analytical model suggests that the peak decreases and shifts towards the border point for a decreasing difference in boundary roughness. However, the data of `Blanckaert et al. [2010]` shows that the peak shifts away from the border point for a decreasing difference in boundary roughness. How can this be explained? Might it be a result of the secondary currents? Assumption (or better simpli-

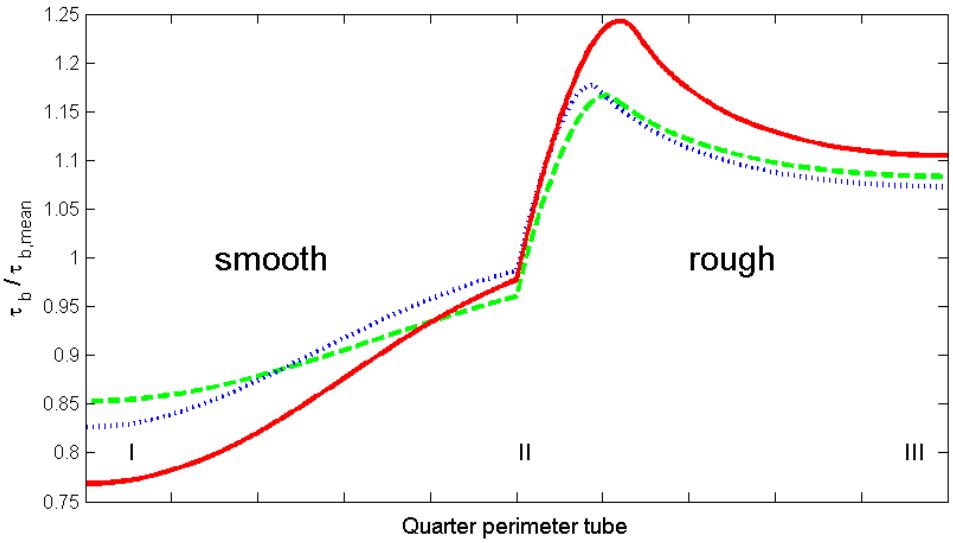

Figure 45: The bank shear stress distribution (BSSD) for a quarter of the tube. The red solid line represents the BSSD for the in Figure 44C presented scenario. The blue dotted line represents the same scenario where only the mixing parameter is increased to $a = 3$. The green striped line represents the same scenario where only the 'smooth' roughness is doubled, thus the roughness difference is decreased.

Boundary roughness distr.	⇒	(1) Secondary flow (2) Shear forces	⇒	Streamwise velocity field	⇒	Boundary shear stress distr.

Diagram 18: Two mechanisms in which the boundary roughness distribution can influence the boundary shear stress distribution.

fication) 1 holds that the secondary currents are neglected in the analytical model though they are present in reality. Whereas the boundary roughness distribution affects both the secondary flow and the molecular and turbulent shear forces (Diagram 18), the present analytical model only considers the latter.

Another interesting point of discussion is the physical meaning of the mixing parameter a. Currently the value is chosen quite arbitrarily. In reality the mixing parameter depends, besides on secondary flow (which is neglected), on the molecular and turbulent viscosities. Consequently, since the molecular viscosity is relatively small from a certain distance away from the boundary, the mixing parameter a depends mainly on turbulent properties. A larger turbulent kinetic energy is thus expected to lead to a higher mixing parameter a. But how does the turbulent kinetic energy depend on the boundary roughness distribution?

Conclusion

Although this simplistic model leaves a lot of questions unanswered, the following conclusions can be drawn:

1. The shape of bank shear stress found by `Blanckaert et al. [2010]`, i.e. with a peak close to the border point between the rough and the smooth boundary, can be obtained with a model only considering shear forces.

2. Shear forces alone cannot explain the shift of the peak in the bank shear stress away from the border point which according to the data of `Blanckaert et al. [2010]` happens when decreasing the difference in boundary roughness.

3. A smaller difference between the roughnesses leads to a lower peak in the bank shear stress and a to more uniform bank shear stress distribution.

4. More effective mixing leads to a lower peak in the bank shear stress and to a more uniform bank shear stress distribution.

F.3 Secondary flow

Research Question

What is the effect of secondary circulations on the distribution of the boundary shear stress? A simplified numerical model, where the secondary currents are imposed *a priori*, is used to asses this question.

Physical Background

Interaction between the (or exchange of) water particles transfers the effect of a solid boundary into the flow. A distinction can be made between interactions on molecular level (the molecular scale) and interactions on a larger level (the flow scale). The **interactions on the molecular scale** can be regarded to be an intrinsic property of the fluid and independent of the flow properties. These interactions are in fluid dynamics always parameterized by the molecular viscosity. The **interactions on the flow scale** can be divided into turbulence and currents perpendicular to the main flow (secondary currents). Averaged in time the turbulence is zero. Averaged in space the secondary currents are zero. The influence of the solid boundary on the flow field, implying a reactive force, depends on these interactions. Without any interaction the flow would accelerate infinitely. Only considering the interactions on the molecular scale will lead to an equilibrium flow field with unrealistically large flow velocities. Taking also the turbulence into account leads to flow velocities with a realistic order of magnitude. As well taking the secondary currents, also contributing to the interaction, into account will lead to even lower flow velocities.

Besides that the interactions determine the average flow velocity, the nature of the interactions also determine the **distribution of the flow velocities**. The molecular and turbulent interactions are symmetrical and can be treated as diffusion. The interaction by secondary currents is asymmetrical and can be treated as advection. For an infinitely small balance area Equation 89 can be applied.

$$\begin{aligned} \frac{\partial \text{Momentum}}{\partial t} &= \text{Forcing} + \sum(\text{Interactions})\frac{\partial^n \text{Momentum}}{\partial y^n} \\ \frac{\partial \text{Momentum}}{\partial t} &= \underbrace{F}_{I} + \underbrace{u_y \frac{\partial M}{\partial y}}_{II} - \underbrace{(K_t(y) + K_m)\frac{\partial^2 M}{\partial y^2}}_{III} \end{aligned} \tag{89}$$

where (I) is the forcing, (II) is the contribution of the secondary currents and (III) the contribution of the molecular and turbulent interactions.

Boundary Shear Stress The **average boundary shear stress** is, obeying Newton's third law, equal to the forcing. Considering a constant cross section, the average boundary shear stress is not dependent on the interactions (albeit given that there are interactions). The **local boundary shear stress** is, however, determined by the velocity and turbulence field and these depend on the amount and nature of the interactions.

Model

Solving Equation 89, the influence of secondary currents can be assessed. However, the advection-diffusion equation can't be solved analytically. A simplified model is adopted to solve the problem numerically. By defining the forcing, channel geometry, turbulence and secondary velocity field,

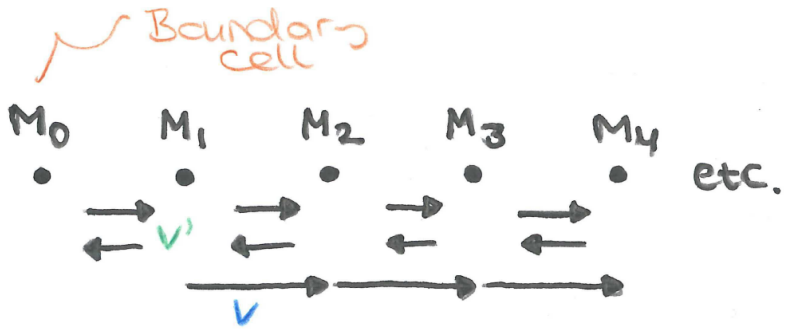

Figure 46: Interaction perpendicular to the streamwise direction.

the streamwise velocity field and thus also the discharge and the local boundary shear stresses are obtained.

Governing Equation The secondary current is implemented and the molecular and turbulent interactions are implemented as a 'Reynolds velocity' (Figure 46). The finite volume approach, which is momentum conservative, is used. For a two-dimensional space, a uniform streamwise direction and *one* perpendicular direction, the discrete Equation 90 is given.

$$\frac{\partial \mathrm{M}_n}{\partial t} = \underbrace{\frac{1}{4}\frac{(v_{n-1}+v_n)\mathrm{M}_{n-1} + (v_{n-1}-v_{n+1})\mathrm{M}_n - (v_n+v_{n+1})\mathrm{M}_{n+1}}{\Delta x}}_{\text{advection}} + \underbrace{\frac{1}{4}\frac{(v'_{n-1}+v'_n)\mathrm{M}_{n-1} - (v'_{n-1}+2v'_n+v'_{n+1})\mathrm{M}_n + (v'_n+v'_{n+1})\mathrm{M}_{n+1}}{\Delta x}}_{\text{diffusion}} + \mathrm{F}_n \tag{90}$$

where M is the momentum 'storage' (which is a measure for the streamwise velocity), v is the secondary velocity, v' is a 'Reynolds type' velocity, F the forcing and Δx the grid size.

Boundary Conditions Boundary points are defined to account for the boundary effects. A distinction is made between closed and open boundaries. Through both open and closed boundaries no flow occurs, thus the velocity v at each boundary point equals zero. At the open boundaries the free slip condition is applied, which implies no momentum loss. Thus at the open boundaries also v' is zero. At the closed boundaries the no slip condition applies which means that momentum is lost from the system. To establish this, the fluctuation 'Reynolds type' velocity at the boundary is larger than zero and the momentum 'storage' in the boundary point is zero. The non-zero 'Reynolds velocity' at the boundary accounts for the molecular interaction. The boundary properties are summarized in Table 19. Note that the momentum that is lost from the system depends on the momentum (streamwise velocity) and 'Reynolds velocity' in the cell next to the boundary cell.

Solving Procedure Since the steady solution is of interest, the equations simplify to a set of ordinary differential equations. Inclusion of the boundary conditions leads to the matrix below. From the summation of the columns it can be seen that the discretization is momentum conservative except at the boundaries where momentum is lost due to interaction with the wall.

	M_0	v_0'	v_0
Open boundary, x_0	0	0	0
Closed boundary, x_0	0	v_1'	0

Table 19: Boundary conditions

Three-Dimensional Extension When not taking one but two directions perpendicular to the streamwise direction into account the same procedure is carried out for two directions. Hence, a three dimensional matrix arises. Note that the three-dimensional matrix has to be converted into a two-dimensional matrix before being solved.

Model Matrix

For M_0 is a closed boundary:

$$\begin{bmatrix} -\frac{1}{2}v_1' - \frac{1}{4}(v_1' + v_2') - \frac{1}{4}(v_1 + v_2) & \frac{1}{4}(v_1' + v_2') - \frac{1}{4}(v_1 + v_2) & 0 & \dots \\ \frac{1}{4}(v_1' + v_2') + \frac{1}{4}(v_1 + v_2) & -\frac{1}{4}(v_1' + v_2') - \frac{1}{4}(v_2' + v_3') + \frac{1}{4}(v_1 + v_2) - \frac{1}{4}(v_2 + v_3) & \frac{1}{4}(v_2' + v_3') - \frac{1}{4}(v_2 + v_3) & \dots \\ 0 & \frac{1}{4}(v_2' + v_3') + \frac{1}{4}(v_2 + v_3) & -\frac{1}{4}(v_2' + v_3') - \frac{1}{4}(v_3' + v_4') + \frac{1}{4}(v_2 + v_3) - \frac{1}{4}(v_3 + v_4) & \dots \\ \dots & \dots & \dots & \dots \end{bmatrix}$$

$$\begin{bmatrix} M_1 \\ M_2 \\ M_3 \\ \dots \end{bmatrix} = \begin{bmatrix} F_1 \\ F_2 \\ F_3 \\ \dots \end{bmatrix}$$

And for M_0 is an open boundary:

$$\begin{bmatrix} \frac{1}{4}(v_1' + v_2') - \frac{1}{4}(v_1 + v_2) & \frac{1}{4}(v_1' + v_2') - \frac{1}{4}(v_1 + v_2) & 0 & \dots \\ \frac{1}{4}(v_1' + v_2') + \frac{1}{4}(v_1 + v_2) & -\frac{1}{4}(v_1' + v_2') - \frac{1}{4}(v_2' + v_3') + \frac{1}{4}(v_1 + v_2) - \frac{1}{4}(v_2 + v_3) & \frac{1}{4}(v_2' + v_3') - \frac{1}{4}(v_2 + v_3) & \dots \\ 0 & \frac{1}{4}(v_2' + v_3') + \frac{1}{4}(v_2 + v_3) & -\frac{1}{4}(v_2' + v_3') - \frac{1}{4}(v_3' + v_4') + \frac{1}{4}(v_2 + v_3) - \frac{1}{4}(v_3 + v_4) & \dots \\ \dots & \dots & \dots & \dots \end{bmatrix}$$

$$\begin{bmatrix} M_1 \\ M_2 \\ M_3 \\ \dots \end{bmatrix} = \begin{bmatrix} F_1 \\ F_2 \\ F_3 \\ \dots \end{bmatrix}$$

Results

To get better insight and to show the performance of the model first the results of the two-dimensional model are presented. However, to implement secondary currents in a two-dimensional domain the mass conservation law needs to be violated. Subsequently, the results of the three-dimensional model are addressed.

Two-Dimensional A scenario with a wall at both sides of the flow is considered. Implementing **no secondary current** and a **constant 'Reynolds velocity'**, corresponding with laminar flow, a parabolic velocity profile arises (Figure 47). This is in agreement with literature. Implementing a towards the core of the flow linear increasing 'Reynolds velocity', corresponding with the **mixing length model**, a logarithmic profile arises. This also agrees with literature.

Next we include a **secondary current** (violating the mass conservation law). As secondary currents have a direction this leads to asymmetry. For a constant 'Reynolds velocity' and different constant secondary currents (as in Table 20) the profiles as presented in Figure 48 arise. It appears that the secondary currents leads to a lower average velocity, or discharge (Table 20), and relatively higher flow velocities near the right boundary. Logic consequence is that the shear stress on the right boundary increases while the shear stress at the left boundary decreases (Figure 49). The average boundary shear stress remains equal, since the forcing doesn't change.

Three-Dimensional In the three-dimensional space violating the mass conservation law is no longer inevitable. Here a squared channel, width-to-depth ratio equal to unity, is considered. For the **secondary current structure** three different cases are considered: (1) a case without secondary currents, (2) a case with four rotating cells and (3) a case with one rotating cell mimicking the outer-bank cell. Calculations are made for a **closed conduit** and for an **open channel**. For the 'Reynolds velocity' the **mixing length model** is used. The results are presented in Figures 50 to 55.

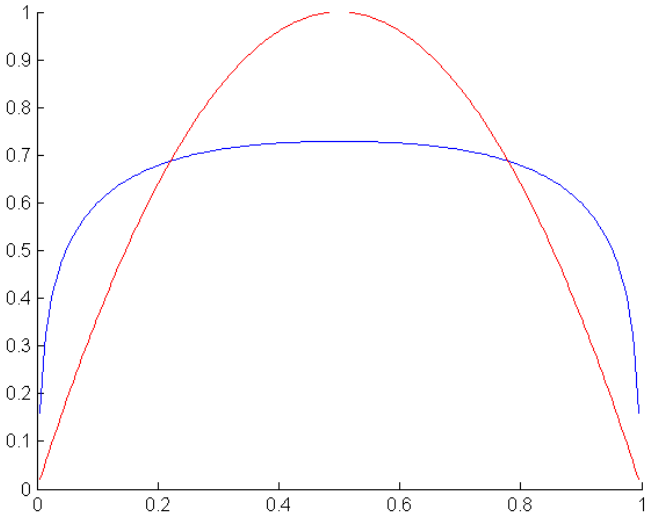

Figure 47: Velocity profile for 2D-flow between two walls using a constant 'Reynolds velocity' (red line) and a towards the core of the flow linear increasing 'Reynolds velocity' (blue line).

v/v'	Q/Q_0
0	1.00
0.001	1.00
0.01	0.80
0.1	0.14
1	0.01

Table 20: Discharge relative to the discharge of the case without secondary currents for different strengths of the secondary current relative to the 'Reynolds velocity'.

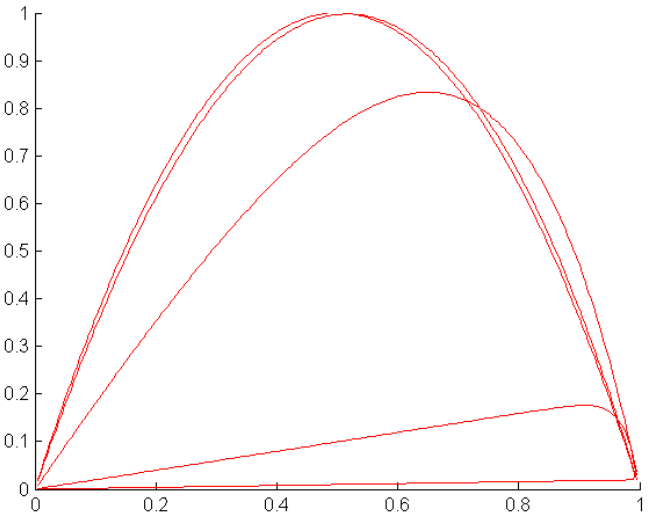

Figure 48: Five velocity profiles for 2D-flow between two walls using a constant 'Reynolds velocity' (red line) and different constant secondary currents as presented in Table 20.

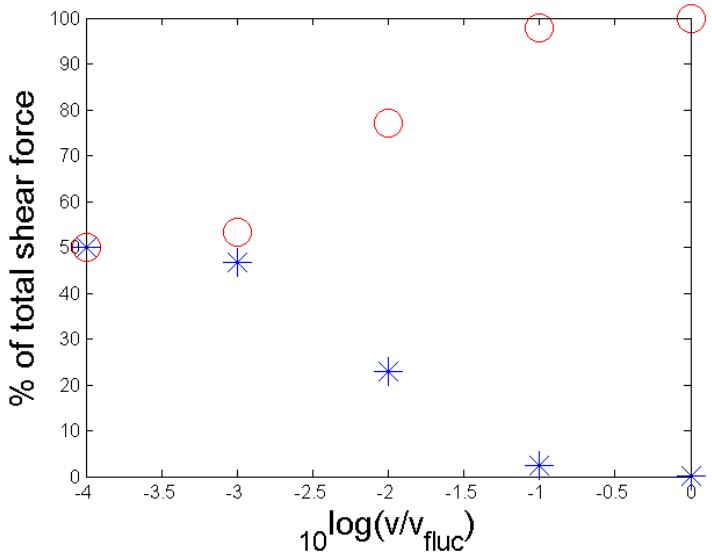

Figure 49: Percent of the total shear force that is exerted on the left (blue asterisks) and right (red circles) boundary of a two-dimensional flow subjected to a constant secondary current towards the right boundary. It is plotted against the strength of the secondary current relative to the 'Reynolds velocity' on a logarithmic scale.

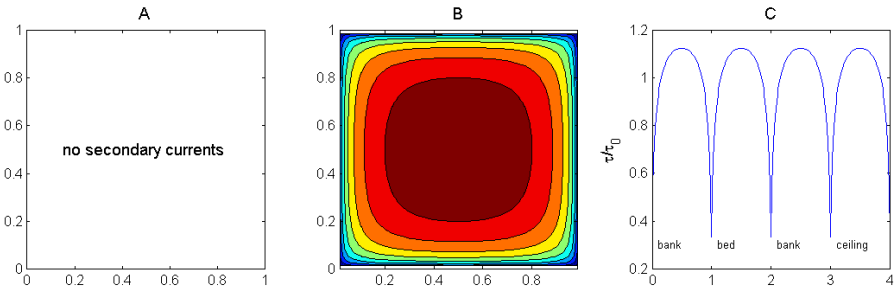

Figure 50: (A) Secondary current structure (by means of the stream function), (B) streamwise velocity field and (C) boundary shear stress distribution for a closed conduit.

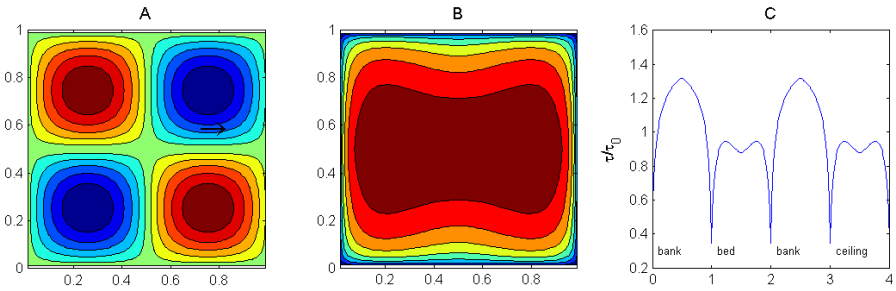

Figure 51: Idem

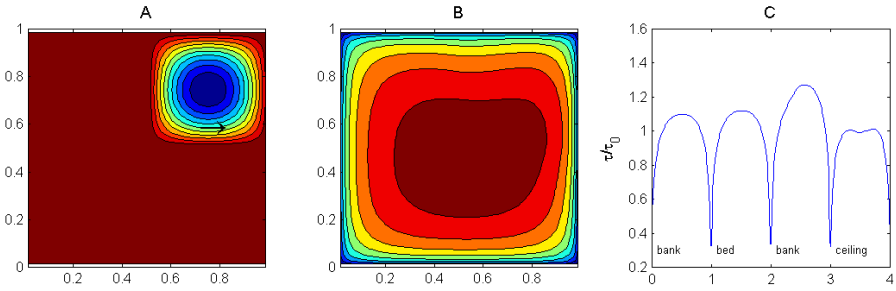

Figure 52: Idem

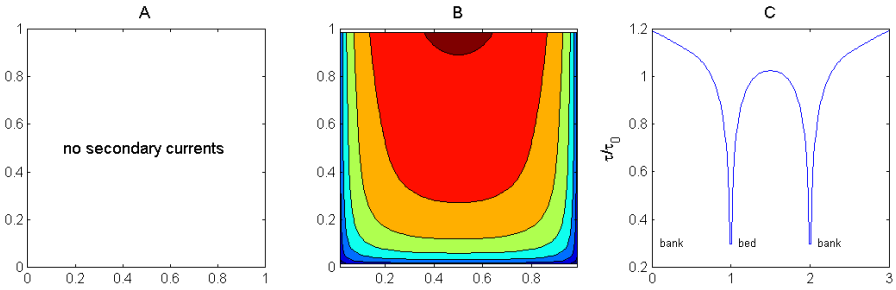

Figure 53: (A) Secondary current structure (by means of the stream function), (B) streamwise velocity field and (C) boundary shear stress distribution for an open channel.

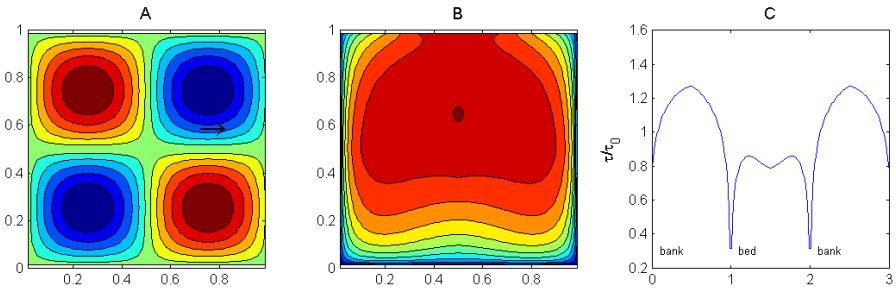

Figure 54: Idem

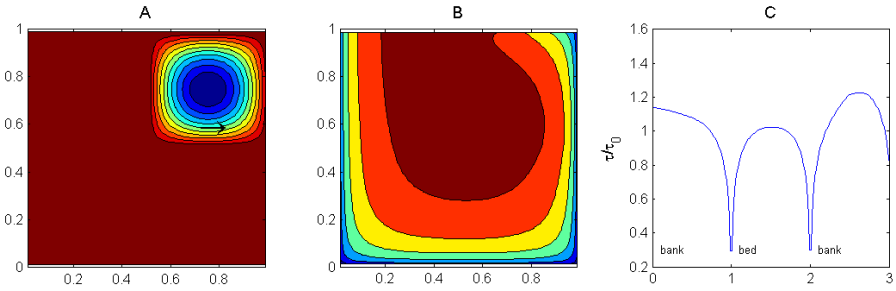

Figure 55: Idem

G Subjects for Further Study

Some subject for further research.

1. Assessing the turbulence closure model in order to improve its performance close to the wall. This is important for the implementation of the boundary, especially when using the Immersed Boundary Method. The current Smagorinsky Model can be made directional dependent close to the boundary or the Smagorinsky Model of `Lévêque [2006]` can be implemented.

2. Assessing the Immersed Boundary Method. Different approaches are available (`Mittal [2005]`). Assess the importance of the fluid grid points chosen to interpolate point I.

3. Including the Immersed Boundary Method for moving boundaries (`Mittal [2005]`). Assess the opportunities of this method.

4. Implementing the two-layer wall model (`Van Balen [2010]`) in combination with non-grid aligned boundaries.

5. Doing flume experiments with a with the point bar related transverse bed slope. This for validation of the numerical results.

6. Reassessing the adaptation length equation for developing curvature (Equation 2, `Ottevanger [2013]`).

7. Parameter study to the outer-bank shear stress in naturally curved flows.